Investigation of Nanoscale intercalation into graphite and carbon materials by *in situ* Scanning Probe Microscopy

Inauguraldissertation

der philosophisch-naturwissenschaftlichen Fakultät
der Universität Bern

vorgelegt von

Dario Alliata

von Italien

Leiter der Arbeit: Prof. Dr. H. Siegenthaler
Departement für Chemie und Biochemie der Universität Bern

und

Dr. R. Kötz
Paul Scherrer Institut, Allgemeine Energieforschung, Elektrochemie,
Villigen und Würenlingen

von der philosophisch-naturwissenschaftlichen Fakultät angenommen

Bern, den 28. Juni 2000 Der Dekan

Prof. A. Pfiffner

1. Abstract

Graphite and Metal Oxide were extensively studied as electrode materials in ion transfer batteries, and the macroscopic changes of their properties during insertion were investigated for many years. The knowledge of dimensional changes during electrochemical processes is fundamental for the understanding of the electrochemical ion exchange mechanism and for prospective practical applications. However, so far the analysis of ion intercalation processes gave rarely information on a local microscopic scale. For this purpose, Scanning Probe Microscopy (SPM) techniques can be used to probe thickness changes or local spectroscopic properties, even in nanometer scale.

Aim of the work was the local and time dependent investigation of dimensional changes of the host material during electrochemical intercalation processes on the nanometer scale. Scanning Probe Microscopy, combined with Cyclic Voltammetry, was used as in situ tool of analysis during intercalation and deintercalation of ions into the electrodes. Ex situ techniques, like X-ray Photoelectron and Raman Spectroscopies, were also used to obtain complementary information.

The activity of the thesis was initially focused onto the system of highly oriented pyrolytic graphite (HOPG) in aqueous and non-aqueous electrolyte, as a model to elucidate the mechanism of electrochemical intercalation in graphite. Then it was extended to a practical electrode, i.e. carbon electrodes suitable for developing of μ-batteries.

The first results were obtained on graphite intercalated compounds formed in HOPG in perchloric acid. The intercalation process was characterized quantitatively by in situ Atomic Force Microscopy. The HOPG interlayer spacing increases by 32% to 66% for the formation of stages IV-III-II of graphite intercalation compounds, when perchlorate ions intercalate. The dimensional changes were studied as a function of the step height in a range between 6.7 Å, corresponding to a bilayer of HOPG planes, and micrometers, corresponding to hundreds of HOPG planes. The main result is that the percentage change of the interlayer distance decreases with increasing number of graphene layers involved in the intercalation process. In addition, the local aspect of the process was demonstrated by revealing coexisting regions with different kinetics for intercalation and deintercalation processes. Intercalation in HOPG was investigated also in sulfuric acid. As a

consequence of the much lower charge efficiency only the stage IV formation could be evaluated in H_2SO_4. Compared to the results for the stage IV formation in perchloric acid, dramatic change of the surface morphology were observed already after 2-3 intercalation cycles in sulfuric acid.

The effect of the intercalation process on the friction at the surface of HOPG was studied in both acids. The friction coefficient was observed to change at step locations. Lateral Force Microscopy, Cyclic Voltammetry and XPS results indicated that the initial adsorption of ions is responsible for the variation of the friction in proximity of the steps on the HOPG surface.

The in situ SPM investigation was subsequently extended to the intercalation of Li ions in graphite. When a carbon electrode in non-aqueous electrolyte is charged for the first time from the open-circuit potential (3 V) to close 0 V (vs. Li/Li^+), Li^+ are inserted into the carbon structure. In addition to Li^+ insertion, the other major electrochemical/chemical reactions that occur during the first charge are the decomposition of the electrolyte on the carbon surface and the formation of a surface layer, often referred to as the solid electrolyte interface (SEI) layer. For this purpose, HOPG and carbon electrodes were studied in an organic electrolyte ($LiClO_4$ in EC:DMC). Scanning Tunneling Microscopy (STM) and Atomic force microscopy (AFM) combined with cyclic voltammetry were used as in situ tools of analysis during intercalation and deintercalation of Li ions. Both STM and AFM results showed the presence of hill-like structures on HOPG basal planes, as soon as the potential of ca. 1 V was reached. The hills are 1-2 nm in height and can be explained on the basis of the co-intercalation model [1]. Subsequently, a SEI film starts to form at ca. 0.7 V. The in situ AFM technique revealed that the SEI film is very rough at the beginning, and does not cover the whole surface of the HOPG electrode. After two complete cycle, the SEI film is about 20 nm thick and covers the entire surface. Later on the film was observed to grow until reaching the maximum thickness of ca. 40 nm. Combining the in situ AFM results with literature data, we believe now that at first the solvent intercalates within graphite and is reduced to form gas, organic radicals and polymers. Then a SEI film precipitates on the surface via a nucleation and growth mechanism.

Carbon electrodes obtained by pyrolysis of photoresist materials were also investigated by AFM, XPS and Raman techniques. Ex situ current sensitive AFM and four point probe method revealed a clear dependence of the sheet resistance upon the temperature of pyrolysis. XPS and Raman results confirmed the trend of the resistance measurements and are in good agreement with the general behavior of glassy carbon. This variation in sheet resistance affected the thickness of the SEI film formed and more generally the electrochemical activity, as pointed out by in

situ AFM measurements on carbon electrodes pyrolyzed at different temperatures.

Therefore, the resistance of the SEI film formed on HOPG and carbon electrodes was studied by ex situ current sensitive AFM. As expected, the SEI film showed a very low conductivity and a non linear resistance behavior. Furthermore, the SEI film morphology could be modified locally by applying bias voltages of 20 V.

In conclusion HOPG and carbon electrodes in different aqueous and non-aqueous electrolytes were successfully characterized by in situ SPM in conjunction with Cyclic Voltammetry. The current results on the sub-microscopic level are important for understanding the behavior of graphite and carbon electrodes, and for the optimization of electrolyte solutions for rechargeable Li batteries. Similar investigation might be extended to Metal Oxide, the positive electrode of a Li-ion battery system.

2. Introduction

2.1 Motivation

Electrochemical insertion processes play a fundamental role in several electrochemical devices such as batteries, electrochromic displays and actuators. Typical insertion/intercalation materials are graphite and metal oxides, where anion as well as cations may be inserted.

Ion insertion is also the fundamental process in the Li ion battery [2] which is considered the most promising advanced battery with very high energy density. However, despite it has been already introduced in the market of consumer electronics, several problems remain unresolved. One major drawback is the dimensional change occurring during the electrochemical process. A knowledge of this change is fundamental for an understanding of the electrochemical intercalation / insertion mechanism and for the evaluation of potential practical applications.

The macroscopic changes occurring in the mechanical properties of graphite during insertion were investigated for many years [3, 4, 5]. While the ion exchange between an electrode and the bathing electrolyte may be monitored by techniques such as Probe Beam Deflection (PBD) or Electrochemical Quartz Crystal Microbalance (EQCM) [6], an in situ observation of dimensional changes of the electrodes is difficult. Neutron [7], X-ray [8] diffraction and dilatometry [9] techniques can provide average information about the overall results of the intercalation processes, but are completely useless on a local microscopic scale.

Scanning Probe Microscopy [10] techniques can be used to investigate the surface of graphite electrodes under potential control and to probe thickness changes or local electronic properties, even on a nanometer scale [11, 12]. Recently Li^+ intercalation was observed in situ by Scanning Tunneling Microscopy (STM) [13] and Atomic Force Microscopy (AFM) [14] which proved to be powerful techniques in the context of battery research.

2.2 Carbon and graphite materials

Carbon exists, in its elementary form, in almost every possible structural order and morphology, from well defined three-dimensional ordered graphite to X-ray amorphous glassy carbon.

Carbon is selected for many electrochemical applications because of its good electrical and thermal conductivity, low density, corrosion resistance, low thermal expansion, low elasticity, and high purity. In addition, carbon materials can be produced in a variety of structures, such as powders, fibers, large blocks, and thin solid sheets. Furthermore, carbon materials are generally available at low-cost.

In a storage device like a battery, a particular form of carbon is preferred because of its good properties: graphite.

Graphite crystallizes in a layer lattice. The carbon atoms form regular sheets of linked hexagons which are displaced relative to one another.

The hexagonal structure which is shown in Figure 2-1 consists of planes of carbon stacked along the c-axis in an array usually denoted as ABAB sequence, where the lateral shift, from layer A to layer B, is 2.46 Å.

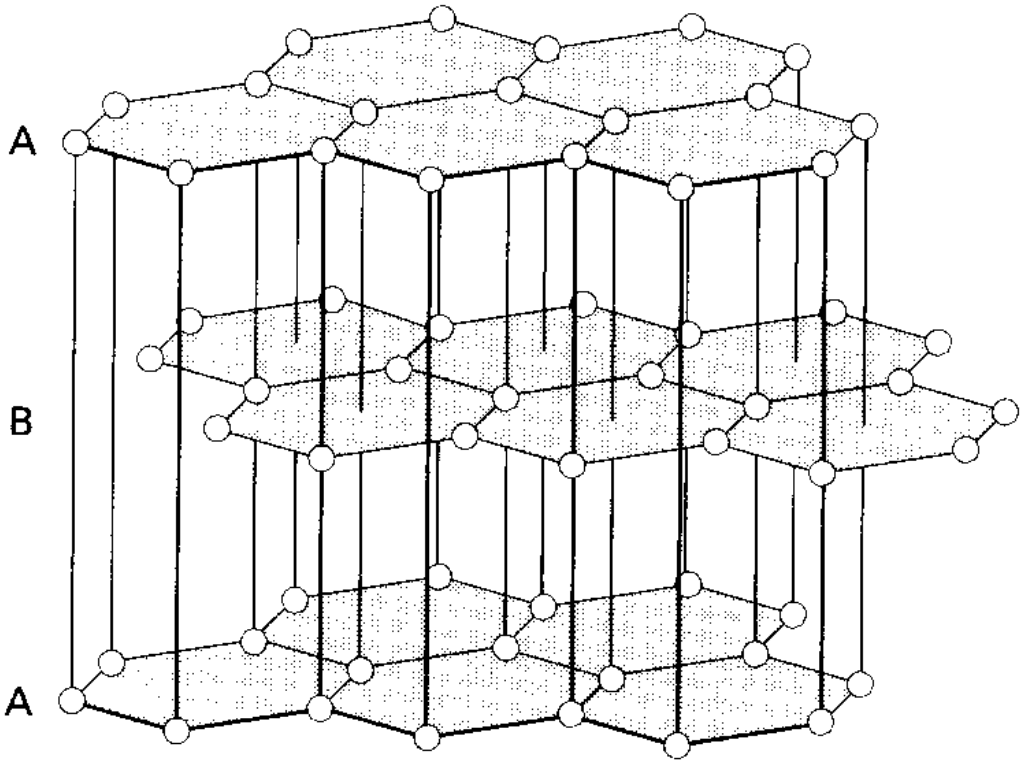

Figure 2-1: Structure of hexagonal graphite showing the ABAB stacking of honeycomb carbon layers. The layer B is shifted with respect to the layer A of 1.42 Å. The distance between two layers is 3.35 Å, while the distance between two adjacent carbon atoms in a hexagon is 1.42 Å.

Despite the normal stacking, other possible sequences exist for graphite. The second major form has a rhombohedral structure where the carbon layers are displaced in such a way that each third layer is superposed, giving a sequence ABCABC.

Within the layer planes each carbon atom is surrounded by three other atoms at a distance of 1.42 Å. The distance between layers is 3.355 Å, which is substantially greater. Corresponding to these different distances there are different types of bonding. Within the layers each carbon atom is linked by a strong covalent bond with its three neighbors (sp^2 hybridization). On the other hand the electrons representing the fourth valence of the carbon atoms are not localized in defined bonds, but are shared by the whole layer. It follows the high thermal and electrical conductivity of the graphite. A rather high energetic reaction is needed to break the covalent bonds and remove separate carbon atoms from the layers, but a suitable reactant is often able to change the state of electrons in the conduction band in order to become intercalated between the carbon planes. When this occurs the graphene planes remain intact and the inter-layer distance increases. For this reason the formation of intercalation compounds is always followed by the swelling of the graphite in a direction perpendicular to the basal planes.

Graphite is available in nature, but it can also be produced artificially from different precursor (petroleum coke, carbon blacks) by a variety of methods [15]. Generally the coke is first heated to remove volatiles. Then after further preliminary treatments, the amorphous carbon is transformed to graphite by heating at 2500°C to 3000°C. Pyrolytic graphite, which is another form of artificial graphite, is produced by the thermal decomposition of carbonaceous gases, usually methane, at the temperatures above 1200°C. When the pyrolytic carbon is heated at high temperatures and , at the same time, a high pressure is applied, the Highly Oriented Pyrolytic Graphite (HOPG) results.

2.3 Intercalation processes

Intercalation may be defined as the insertion of guest ions, atoms or molecules into the interplanar voids of a lamellar structure without destruction of the host's layered bonding network [16]. The major example is the electrochemical intercalation of ions into graphite in a high-energy density battery as Li-ion battery. Here cations and anions penetrate (during the cathodic reduction and the anodic oxidation, respectively) into the van der Waals gaps between the carbon layers and enlarge the interlayer distance. The corresponding charges are accepted into the carbon host lattice, according to the Equation 2-1, where M^+ is a cation, A^- is an anion.

Equation 2-1: $[C_x] + [M^+] + e^- = C_x^-M^+$ and $[C_x] + [A^-] - e^- = C_x^+A^-$.

The product of the intercalation process in graphite is called Graphite Intercalation Compound (GIC).

A special feature of the intercalation in graphite is the formation of a regular array of unoccupied layer gaps that is also called stage formation [17]. In compounds of stage s the guest containing layers are separated by s carbon layers. The stage formation is better described by the schematic diagram shown in Figure 2-2.

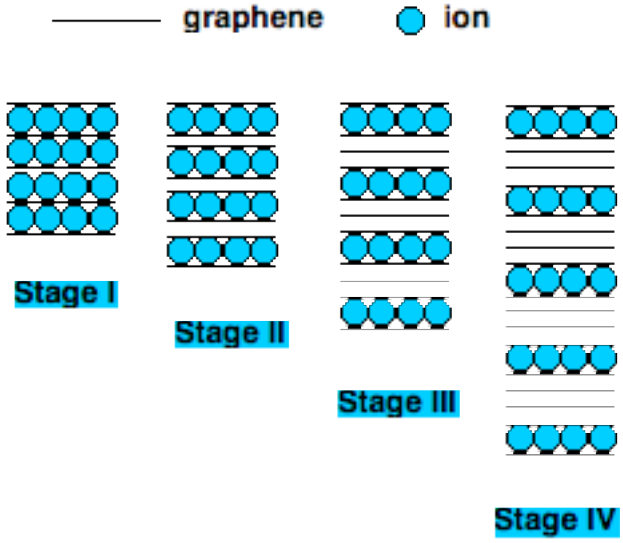

Figure 2-2: Schematic representation for the formation of stages. Graphite Intercalating Compounds are shown in four different arrangements. Solid lines represents carbon layers, while balls represents the intercalated ions.

Because the solvent from the electrolyte can be accepted into the carbon lattice, ternary phases $[C_x^+A^-]y(solv.)$ may also be produced according to Equation 2-2, where A^- is an anion. An equivalent ternary phase is produced by cations.

Equation 2-2: $[C_x] + [A^-] + y(solv.) - = [C_x^+A^-]y(solv.) + e^-$

Within a ternary phase we can distinguish between two-dimensional and three-dimensional solvated phases as shown in Figure 2-3.

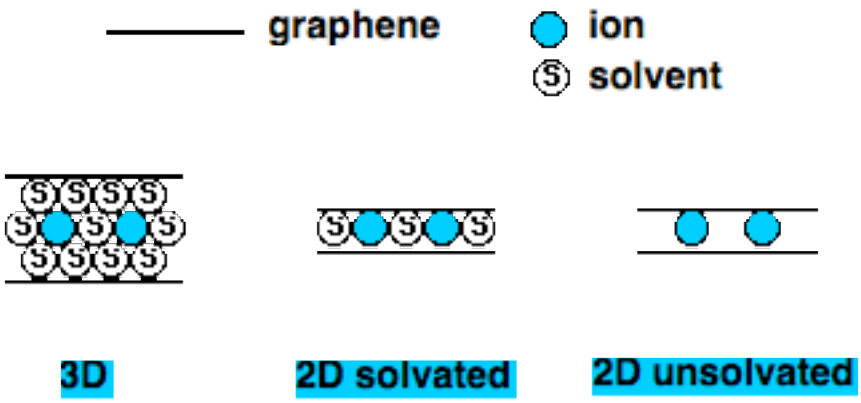

Figure 2-3: Schematic diagram showing the three dimensional and two dimensional solvated and unsolvated ion intercalation compounds. S is for solvent, solid balls are for ions, solid line is for carbon layer [17].

In the two dimensional solvates, the distance between the carbon layers is determined either by the size of the solvent molecule or by the size of the ion. The in plane arrangement of the ions in graphite proceeds in different way according to the type of ion and the experimental conditions. An example of network of graphite/alkali metal and graphite/acid salts intercalation compounds is shown in Figure 2-4.

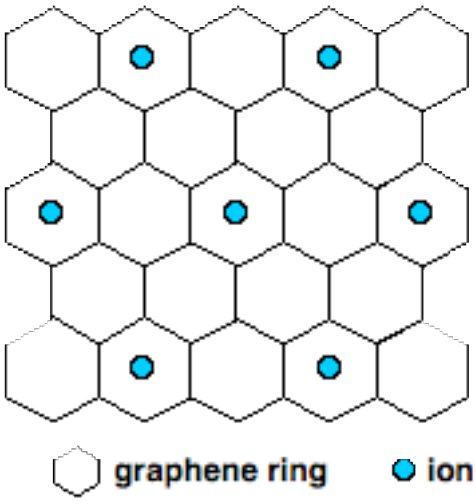

Figure 2-4: In plane arrangement of ions in hexagonal graphite typical for alkali metals and acid salts. Ions seat in the middle of a hexagon of carbons. Therefore, the two layers of carbons adjacent to the intercalated ions are realigned one each other [18].

The carbon planes adjacent to intercalated ions generally shift to lie one above the other so the sites available are prismatic rather than tetrahedral [19]. Therefore, for example, a stage IV compound would have a structure ABAB-BCBC-CACA-ABAB, where the dashes indicate the layers occupied by intercalated atoms.

2.3.1 GICs with anions from aqueous electrolytes

Several authors have already studied the electrochemical behavior of graphite in aqueous [20] electrolytes. Beck et al. [21] showed that the perchlorate ion is one of the best intercalating species at relatively low acid concentrations (2-4 M $HClO_4$), while hydrogen sulfate ions can intercalate efficiently only at higher molarities (10 M H_2SO_4) [22]. Alsmeyer and McCreery investigated the relationship between intercalation processes and side reactions such as oxidation by Raman spectroscopy [23]. They suggested that the graphite lattice be damaged by intercalation of anions. They also proposed that graphite intercalation compounds (GIC) initially formed will subsequently oxidize carbon to form graphite oxides. The observation of surface blister formation on graphite in concentrated acid electrolytes at high potentials by AFM [24] and STM [25] was taken as further evidence for a correlation between initial intercalation and subsequent oxidation. At low electrode potentials no damage of the graphite surface was observed [26]. The latter observation suggests that selecting the right combination of acid concentration and electrochemical potential can minimize the contribution of side reactions.

2.3.2 Intercalation of Li in Li – ion batteries

A fundamental intercalation reaction in terms of practical applications is the Li – GIC formation in non-aqueous electrolytes [27]. This is the major reaction in a Li ion battery, which is becoming the most popular energy storage system for portable electronics and, perhaps in the future, for the zero emission vehicles. In fact, because of the limited energy density of the active electrode components in aqueous cells based on the lead-acid or nickel-cadmium systems, conventional batteries do not meet anymore the requirements of modern electronic devices. More recent developments such as the nickel-metal hydrate system provide improved performance, but in order to achieve significant increases in energy density it has proved necessary to develop advanced rechargeable batteries based on lithium. Since in many applications the weight of the battery is an important issue, the usual goal is to minimize the weight and volume of the battery for a given amount of energy stored. Consequently, the high specific energy of the Li ion battery made it the best candidate as power supply for portable devices (Figure 2-5).

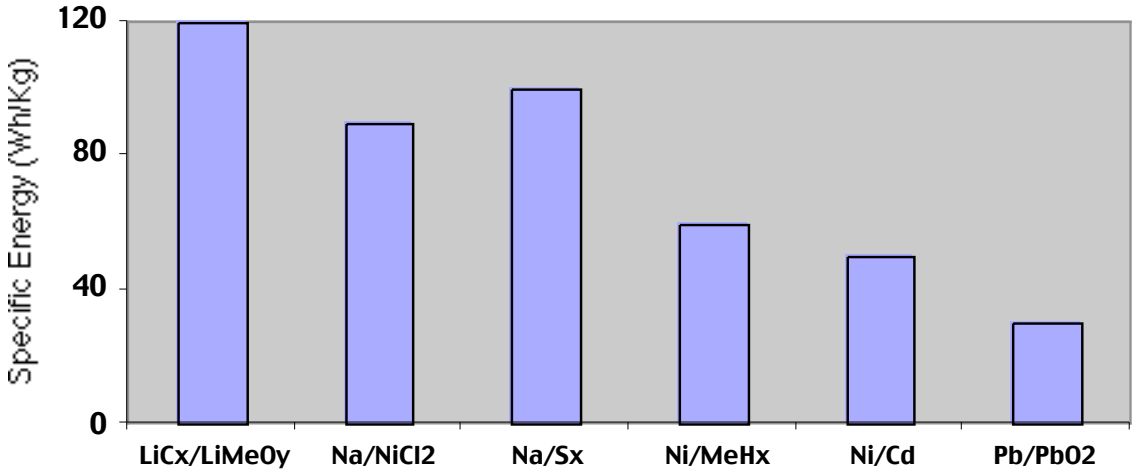

Figure 2-5: Specific Energy of rechargeable battery systems available on the market. Me is for Metal. The Li-Metal oxide cell exhibits the higher specific energy [28].

As mentioned above, graphite is the most popular anode material for a Li ion battery. Li intercalated graphite is used as carbon-based negative electrode coupled to a Metal Oxide positive electrode to form lithium cell (Figure 2-6).

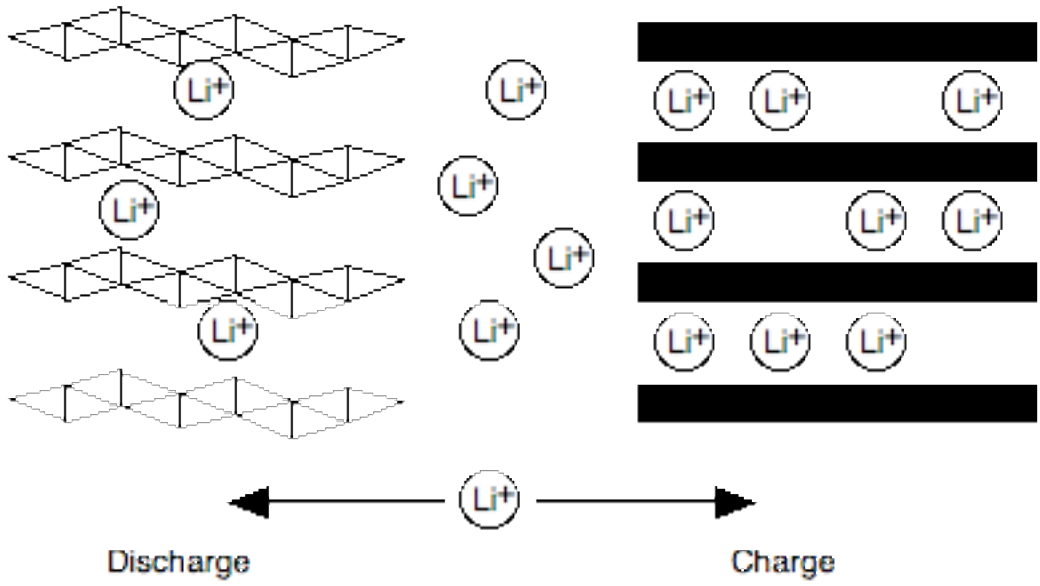

Figure 2-6: Schematic description of a Li ion cell with graphite (right) and metal oxide (left) as anode and cathode electrodes, respectively. Li^+ are intercalated and deintercalated through graphite and metal oxide during charge and discharge of the cell.

The fundamental reversible electrochemical reaction at the graphite electrode is given by the Equation 2-3. The overall cell reaction for the whole system is summarized by the Equation 2-4, where Me is for metal, s for solid and x, z, v depend upon the preparation procedure.

Equation 2-3: $xLi^+ + 6C(s) + xe^- \rightarrow Li_xC_6(s)$

Equation 2-4: $Li_xC_6(s) + Me_zO_y(s) \rightarrow 6C(s) + Li_xMe_zO_y(s)$

Currently, $LiCoO_2$, $LiNiO_2$ and $LiMn_2O_4$, are under investigation in the scientific community as metal oxide positive electrodes.

The electrolyte is another important component of a Li battery. During the last decades, non-aqueous electrolytes of many types were investigated and developed for lithium cells. In the case of lithium batteries, lithium inorganic salts dissolved in aprotic organic solvents have proved to be the most suitable electrolytes. A strong research activity exists in the development of organic solvent-based electrolytes with high decomposition potentials, high ionic conductivity and low vapor pressure.

Nowadays, the most popular organic electrolytes for Li ion batteries are

- Ethylene carbonate (EC);
- Propylencarbonate (PC);
- Dimethylcarbonate (DMC);

while the typical salts are $LiClO_4$, $LiPF_6$ and $LiN(SO_2CF_3)_2$.

Li ions are inserted into the carbon structure, when a carbon electrode in non-aqueous electrolyte is charged. In addition to Li^+ insertion, the other major electrochemical/chemical reactions that occur during the first charge are the decomposition of the electrolyte on the carbon surface and the formation of a surface layer [29]. This layer, also called Solid Electrolyte Interphase (SEI), is essential for the functioning of the carbon electrode, because it prevents the direct reduction of the electrolyte. Unfortunately the Lithium consumption necessary for the film formation reduces the energy density of the cell substantially [30, 31].

Moreover, the quality of the film and therefore the electrochemical stability and reversibility of the electrode varies greatly with the type of electrolyte used, especially when graphitic carbons are used. As a consequence, many efforts were done to determine and understand the chemical and physical properties of the SEI films [32, 33].

Among the available experimental techniques for analysis of SEI film formation processes, only few of them allow in situ investigations. X-Ray Diffraction (XRD) [34], Raman [35], Electron Spin Resonance [36], FTIR [37] and Differential Electrochemical Mass Spectroscopy (DEMS) [38] were successfully used to understand the reactions at carbon electrodes, especially the decomposition mechanism of the electrolytes. It was clarified that when a mixure of EC and DMC is used as solvent electrolyte, only the EC part is decomposed during the first

discharging of the graphite electrode [38]. The main electrochemical reactions involved in the SEI formation process are summerized as follows [106]:

≈1.3 V vs. Li/Li^+:

$H_2O + e^- \rightarrow 1/2\ H_2 + OH^-$;
Electrolyte solvents + $OH^- \rightarrow$ unknown compounds;
Salt anion $+ e^- \rightarrow$ Salt anion reduction products.

≈0.8 V vs. Li/Li^+:

$2\ EC + 2e^- \rightarrow (CH_2OCO_2Li)_2 + CH_2{=}CH_2$;
$(EC + 2e^- \rightarrow Li_2CO_3 + CH_2{=}CH_2)$.

However, the knowledge of the structure and the physical properties of the SEI layer is still very poor. Recent in situ Ellipsometry [39] studies indicated that the SEI layer on a carbon film electrode was 40 Å thick, where data were fitted using a single-layer effective medium approximation model. Winter and co-workers observed the interlayer expansion of graphite in different electrolytes by Dilatometry investigations [40], but the sensitivity of the method is too low to provide information about the thickness and the morphology of the SEI films. To overcome the limits of the above mentioned techniques, Scanning Probe Microscopy was chosed to probe dimensional changes in the nanometer scale in situ.

2.4 General aspects of Scanning Probe Microscopy

In 1986 a Nobel Prize was awarded for scientific progress made five years earlier: a microscope based on electron tunneling [41] which enabled direct atomic-scale measurements to be made (Figure 2-7).
This high-resolution measuring and imaging technique permitted an enormous magnification, allowing atomic information not from an average over many atoms, but rather recorded locally, atom by atom.

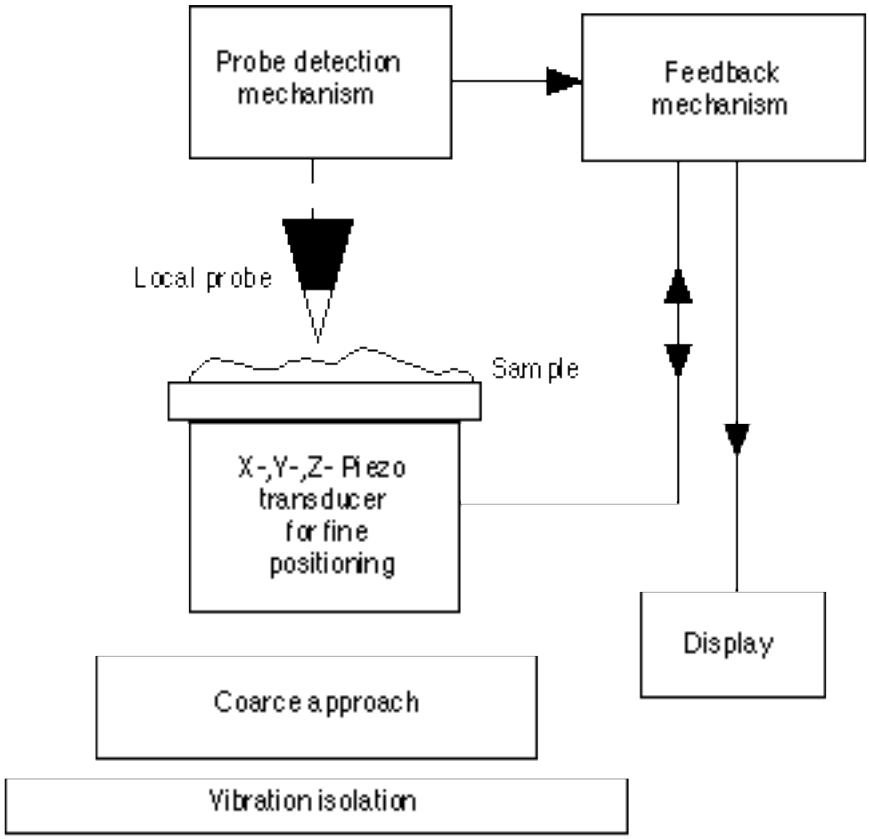

Figure 2-7: Schematic set-up for a scanning probe microscope. The probe is in proximity of the surface of the sample, which is moved by a three dimensional piezo transducer. A stepping motor enables coarse approach, while undesirable mechanical waves are minimized by a vibration isolation system. A feedback circuit is used to keep the relative tip – sample position at a constant value. The topography signal is proportional to the compensation of the feedback circuit.

The operating principle of the scanning tunneling microscope (STM) takes advantage of an electrical current that flows between two conductors that are separated by very small distances, typically angstroms. This current, known as tunneling current, is an electrical current through an extremely thin, insulating layer such as vacuum, air or liquid. The electrons tunnel through this electrical insulating layer, generating a measurable current (typically nanoampers) which is exponentially depending on the distance between the two electrodes, i.e. the thickness of the insulating layer, as described by the Equation 2-5.

Equation 2-5: $I_T \mu V_B \exp[-K(\Phi) s)]$

Here, I_T is the tunneling current, V_B is the bias voltage applied across the two electrodes, Φ is the effective tunneling barrier (eV), K is a constant and s is the spacing between the two electrodes (Å) [42]. It is the exponential dependence of the tunneling current on the distance between the two electrodes (STM tip and the

surface of the sample) that provides the sub-angstrom resolution of the technique in vertical direction.

Five years after the first STM experiments, an STM was mounted in a novel configuration above a cantilever [43]. A diamond tip was mounted to the underside of the cantilever to act as a stylus. A sample mounted on a piezomover was then placed in contact with the stylus and scanned in a x, y plane. Repulsive and attractive interactions between the stylus and the sample surface were registered as deflections in the cantilever. The new imaging tool, the atomic force microscope (AFM) could be extended to non conductive materials. In contrast to the STM, which is based on the electron, tunnel effect, the AFM measures interactions between the scanned tip and the surface such as electrostatic, van der Waals, frictional, capillary and magnetic forces (Figure 2-8).

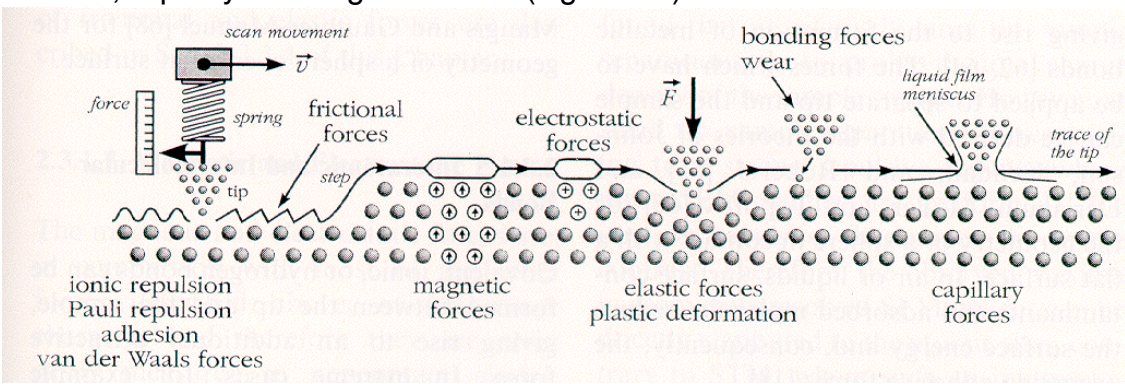

Figure 2-8: Summary of the forces relevant to AFM [44]. Different forces can be probed to investigate local properties of the surface, like friction, adhesion, visco-elasticity, magnetism, electrostatic forces.

Within few years after the first AFM was presented, a family of new instruments was introduced to measure all these interactions. A summary of main scanning probe microscopy (SPM) techniques is shown in Figure 2-9.

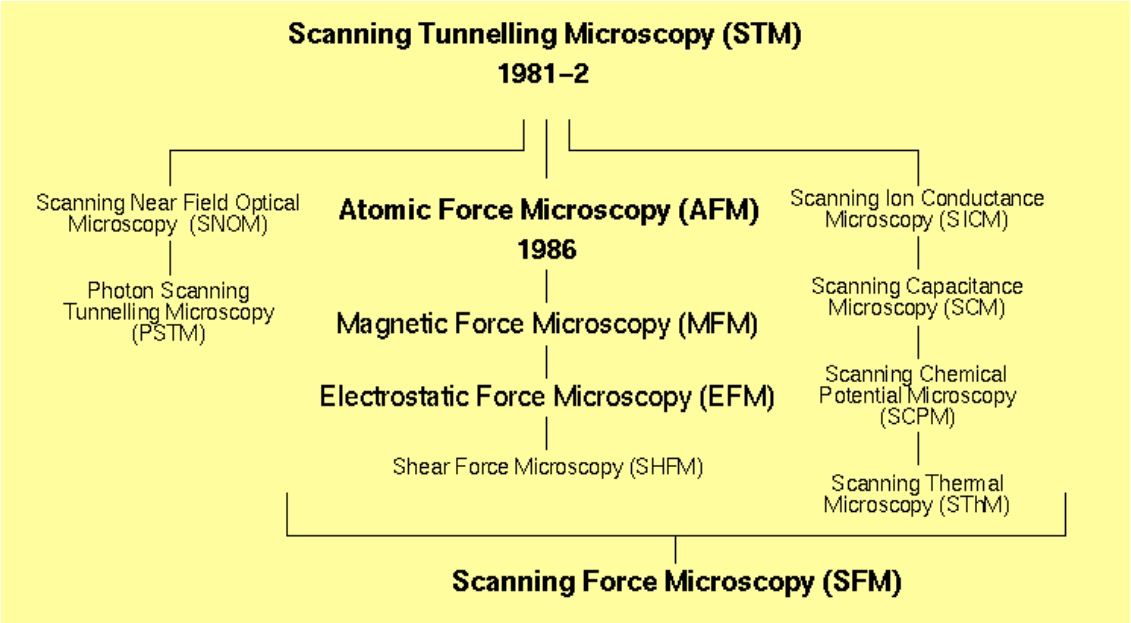

Figure 2-9: Family of SPM techniques. After the introduction of the first STM system in the scientific community, a wide variety of investigating tools was developed up to now.

Because of the possibility to apply STM and AFM in liquid, both techniques were soon applied to investigate biological samples [45, 46] in their physiological environments and electrode surfaces [47] in electrolytes. Therefore, nowadays SPM methods are routinely used as analytical tools in Biophysics [48] and Organic Chemistry [49].

Sonnenfeld and Hansma proposed one of the first applications of STM as a structure-sensitive tool in electrochemistry [50] in 1986, who obtained high resolution images in electrolyte solutions. This aspect is of basic importance because of the conservation of the interfacial environment of the electrochemical processes. The final step towards the great success of scanning probe techniques in Electrochemistry was the introduction of the potentiostatic STM concept in 1988 [51, 52] which enabled the control of the electrochemical processes at the electrode during STM imaging. More recently AFM was also successfully extended to electrolytic imaging [53].

3. Experimental details

3.1 Electrochemistry

Potentiostatic and galvanostatic measurements were performed with an EG&G Princeton Applied Research (PAR) Model 273 potentiostat/galvanostat, which was piloted by a PC Intel 486 station equipped with a 100 MHz processor.
A standard three electrode glass cell, equipped with a Pt foil as counter-electrode, was used during the experiments in aqueous electrolytes.
A Saturated Mercury Electrode (SME) which is

$$Hg \mid Hg_2SO_4 \mid K_2SO_4 \text{ saturated in water}$$

was used as reference electrode. A difference of 680 mV was measured against a Normal Hydrogen Electrode (NHE).
Cyclic Voltammetric experiments in non-aqueous electrolytes were performed in the closed Steel cell developed by Novák et al. [54] In this cell the sample is located between a coin current collector and a lithium foil as reference. A paper foil impregnated of the electrolyte separates the sample from the reference electrode. Two springs press the two current collectors against the sample. In such a way a stable and sealed sandwich configuration is secured. A technical drawing is shown in Figure 3-1.

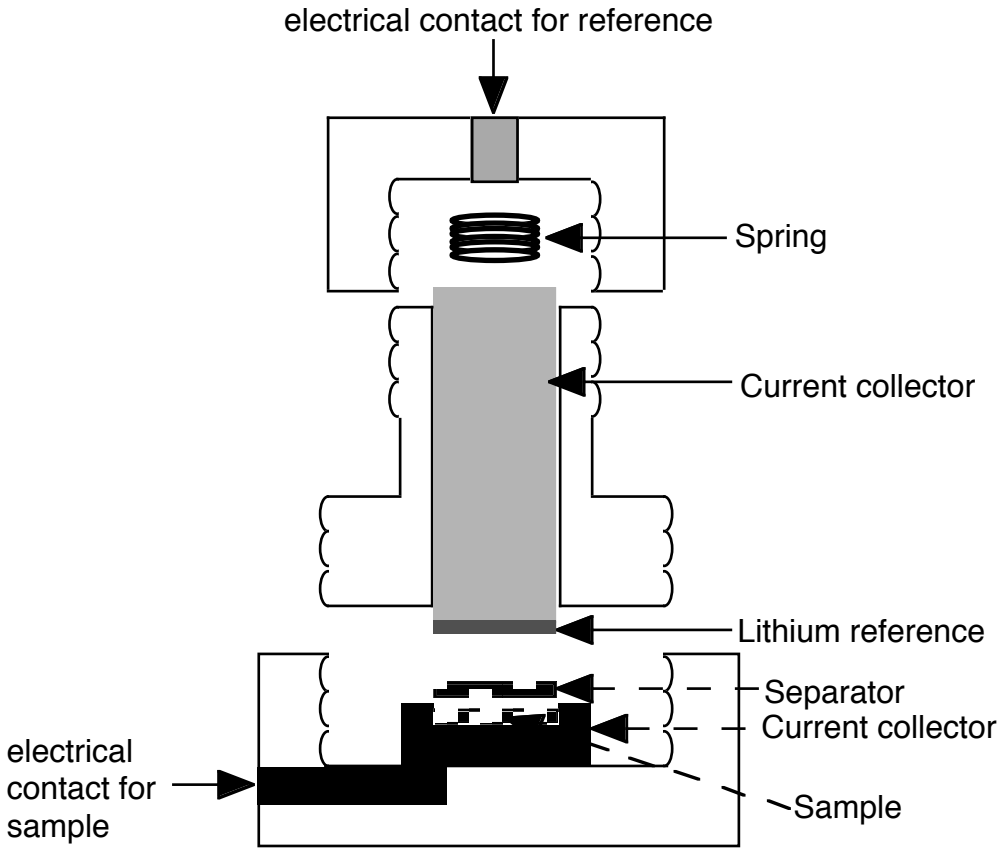

Figure 3-1: Technical drawing of the closed cell for experiments in non-aqueous electrolytes. The small upper cylinder contains the reference mounted on a current collector. The sample is housed in the big cylinder located at the base. A separator impregnated of electrolyte is sandwiched between the sample and the lithium foil. Electrical contacts are provided through external cables.

3.1.1 Electrochemical set-up for in situ SPM measurements in aqueous media

3.1.1.1 Electrochemical SPM cell

Cyclic voltammetry curves during in situ SPM measurements were acquired with an EG&G PAR Versastat 270 potentiostat, directly interfaced with the SPM system.

A commercial electrochemical cell provided by Park Scientific Instruments was used for in situ SPM experiments in aqueous electrolyte. The cell is made of Kel-F, a fluoroplastic that has excellent chemical resistance properties and is thermally stable up to 200°C. The cell contains two compartments which are separated by a ceramic (ZnO_2) diaphragm [55]. The main compartment surrounds the sample and

holds up to 1 ml of liquid. To assure a stable electrical contact with the external SPM sample holder, the sample plate is linked to a solid rod of nickel in a plastic sheath through a conductive epoxy resin (epo-tek® H20E by Polyscience). The metal rod was introduced by mechanical pressure into the insulating plastic sheath (Kel-F). To facilitate dilatation, the sheath was previously heated at 80°C for 1 hour. Then the surface of the assembly, rod and Kel-F sheath, was polished by means of a Mimmet® 1000 polisher equipped with a 9 μm diamond suspension on a Texmet® Polishing cloth (Buehler Company). After polishing, the assembly was washed in an ultrasonic bath with ultra pure water by an Elgastat® UHQPS system (Elga). Finally, the plastic sheath is fixed on a metal plate with a silver conductive paint. The corresponding scheme is shown in Figure 3-2.

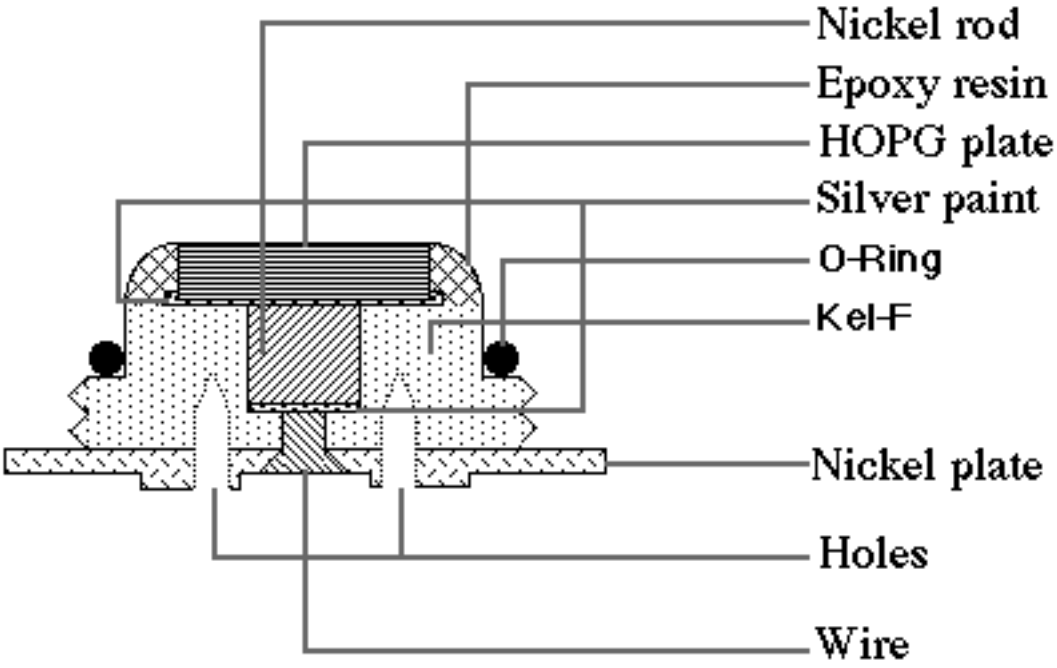

Figure 3-2: Scheme of the working electrode. The edge planes of the HOPG plate are covered with a varnish layer to prevent any contact with the electrolyte. An O-ring assures a sealed connection of the electrode frame to the electrolytic cell. A nickel rod is contacted to the bottom of the HOPG electrode and the top of the nickel plate to provide an external electrical link.

Particular care was made to avoid any crevices between electrode and sheath, where otherwise solutions can penetrate and cause corrosion of the metal sample holder.

The main compartment also houses the counter electrode, which is a Pt wire 1 mm in diameter. The secondary compartment is for the reference electrode (Figure 3-3).

Figure 3-3: Top view of the commercial cell for in situ SPM measurements in aqueous electrolytes. The main compartment houses the sample surrounded by the counter electrode Pt wire. The reference electrode is in the small second compartment on the left.

The diaphragm allows only very small ions, such as H^+, to move from the reference compartment to the main compartment, while larger ions are held back. This design prevents very reactive chemicals from contacting the counter electrode, which could cause a reaction.

3.1.1.2 Pt-Qref electrode

With the cell configuration described in the above paragraph, many electrochemical couples can be used as reference electrodes. Nevertheless, it was decided to adopt a Platinum quasi reference electrode (Pt-Qref) [56], during experiments in aqueous electrolytes. This reference electrode consists of a Pt wire (1 mm in diameter) merged in acid. Before being used, the Pt wire was cleaned with acetone and stored for three days in 3M H_2SO_4. A platinum wire in concentrated acid is normally a practical solution when the high reproducibility of potential is not necessary. The major advantage is the absence of any contamination of the cell. In fact, when an electrochemical couple involving a different electrolyte is used as reference, the risk of an accidental transport of liquid from the reference compartment to the main compartment cannot be excluded.

To study the temporal stability of potential, the position of the oxidation peak of a Glassy Carbon electrode (Hoch Temperature Wekstoffe) in 1 M H_2SO_4 was measured vs. the Pt-Qref. Since this oxidation peak has a well known characteristic potential value [57], it was possible to calculate the reference potential. To investigate possible effects of different storing conditions, two Pt wires were used as reference: one Pt wire was permanently stored in 1 M H_2SO_4, while a second one was dried and stored in air when not used. The results are shown in Figure 3-4.

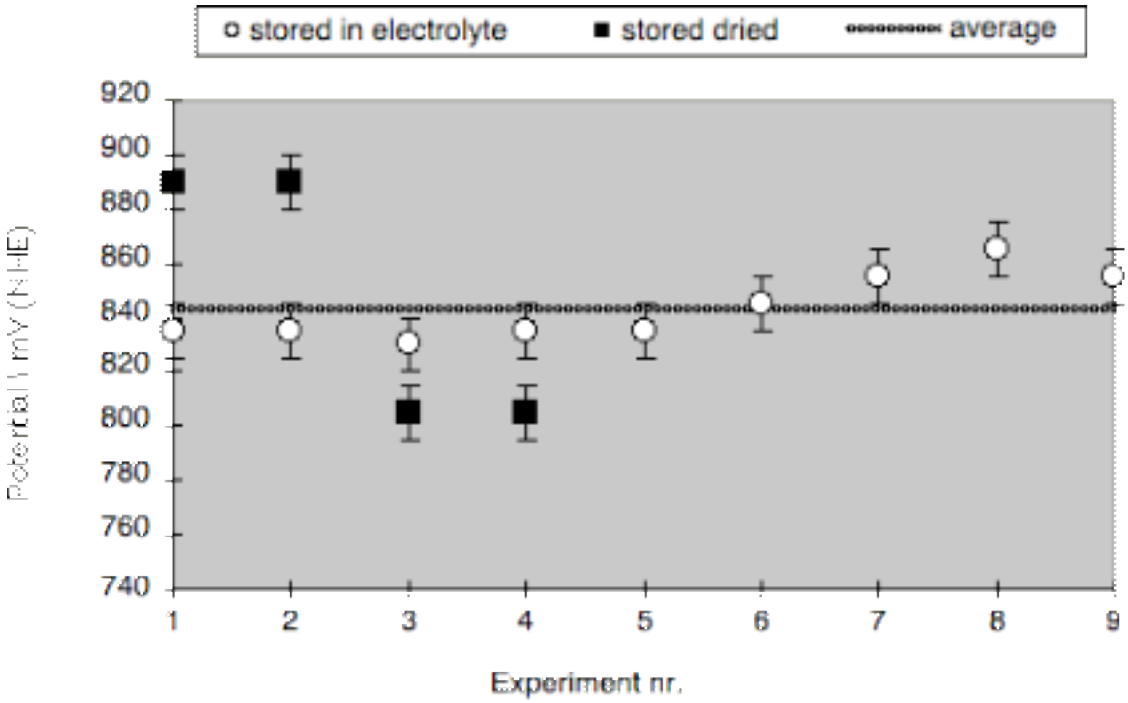

Figure 3-4: Potential of the Pt-Qref electrode in 1 M H_2SO_4 vs. NHE. Data were acquired in a period of three months. The effect of two different storing conditions was tested. Circles and squares indicate the storing of the reference in electrolyte and in air, respectively.

It results that the average potential for our Pt-Qref electrodes was +843 ± 20 mV vs. NHE.

The two half reactions described in Equation 3-1 and Equation 3-2 can explain the origin of this value. They concern the reduction of Platinum oxides, which is carried out in acid solutions.

Equation 3-1: $PtO(s) + 2\ H^+ + 2\ e^- \rightarrow Pt\ (s) + H_2O$ $E° = 0.980$ V;

Equation 3-2: $PtO_2(s) + 4\ H^+\ (aq) + 2\ e^- \rightarrow Pt^{2+}\ (aq) + H_2O$ $E° = 0.837$ V.

The standard potentials for the above reactions were evaluated by Pourbaix et al. by thermodynamic data [58].

A further reaction to be considered at a platinum electrode in acid solution [59] is the reduction of oxygen (Equation 3-3).

Equation 3-3: $O_2 + 2\ H^+ + 2\ e^- \rightarrow HOOH$ $E° = 0.695$ V.

The standard potential measured for the Pt-Qref electrode in acid solution is the combination of the three half reactions written in Equation 3-1 and Equation 3-3.

To control the stability of the Pt reference, its potential was measured at the beginning of every experiment. Since the reference compartment of the ECAFM cell was too small to introduce a standard reference electrode (SCE or SME), the potential of the Pt-Qref was measured vs. a Palladium wire, which was previously activated in sulfuric acid to form a stable Pd/H_2 reference. The experimental set-up used to activate the Pd wire is described in Figure 3-5.

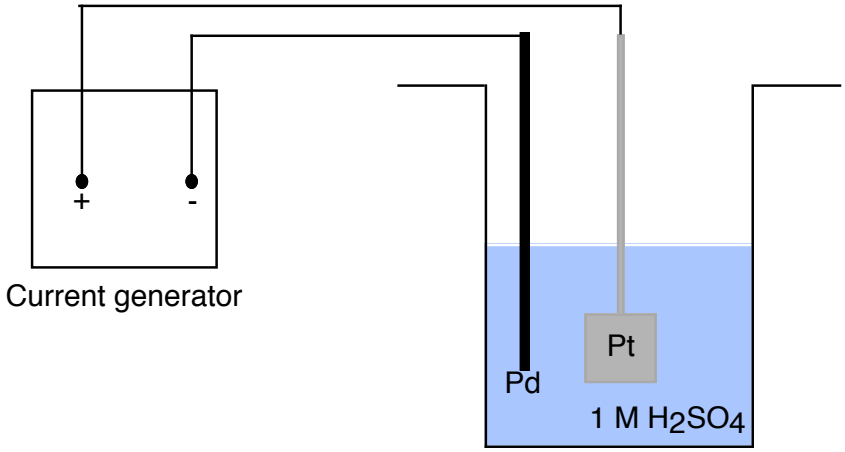

Figure 3-5: Schematic diagram showing the experimental set-up used to activate the Palladium. The Pd wire and a Pt plate are in a sulfuric acid solution (1 M concentrated) and are connected to a current generator.

A 1 mm diameter Pd wire is deep in a solution of 1 M H_2SO_4 together with a Pt foil as counter electrode. Initially, a constant current of ca. 10 mA is applied to the Pd wire with a Varistab® current generator until the first H_2 bubbles are produced. Then the current is increased to ca. 100 mA. Therefore, H_2 bubbles are generated at the Pd wire at a constant rate as long as the Pd bulk is not completely filled with H_2. As soon as the bubble rate grows, the process can be stopped since the Pd wire is fully activated.

When palladium is electrochemically charged with hydrogen, two phases are coexisting. The α-phase is formed first and remains the only one as long as the concentration of hydrogen is below 0.3 atom percent. At higher concentrations the β-phase appears. The coexistence of the two phases is manifested by a constant potential of approximately +50 mV vs. NHE [60].

3.1.2 Non-aqueous media

The investigation of Li intercalation requires an organic electrolyte, which is free of water. Otherwise, before the intercalation of Li can start, water is reduced at the graphite electrode according to the Equation 3-4.

Equation 3-4: $2\ H_2O + 2\ e^- \rightarrow H_2 + 2\ OH^-$ $E° = -0.830$ V.

Therefore, the control of the electrochemical environment is of extreme importance. The following three possible solutions were investigated:

- closed electrochemical SPM cell
- open cell in a glove bag
- open cell in a glove box

The first solution was abandoned due to the impossibility to build a closed cell enough big to prevent bubble accumulation: when a closed cell is too small the bubble generated by electrochemical reactions cannot be removed. At the same time, the electrochemical SPM cell has to be moved by the scanner piezo tube and therefore its dimension and specially its weight have to be limited.
Setting the complete SPM system within a glove bag was an attractive solution because of the low cost of the glove bags and their flexibility in use. This solution was eventually abandoned because of the impossibility of reducing the concentration of water to values less than 100 ppm.
Therefore, we decided to put the cell and the SPM in a glove box filled with an inert gas.
A newly designed SPM cell was manufactured because the Kel-F material reacts with Lithium. The new cell is in Polypropylene with only one main compartment, where all the electrodes are located (Figure 3-6).

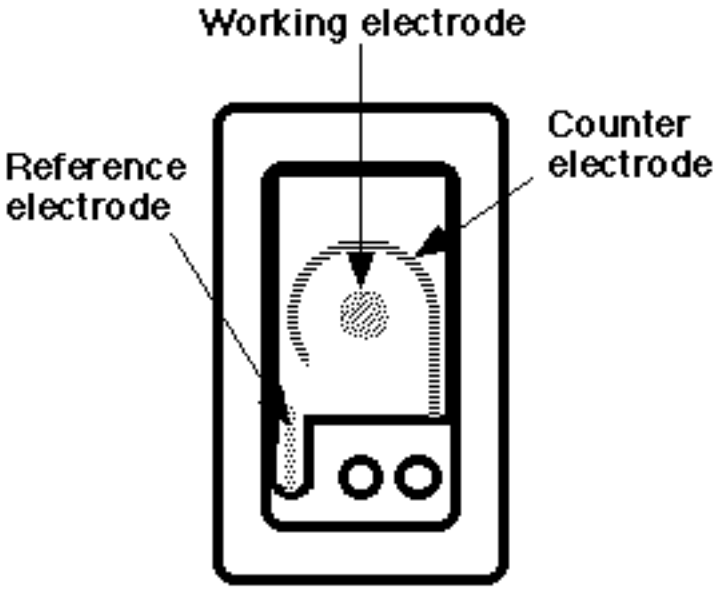

Figure 3-6: Scheme of the new SPM cell for non-aqueous media. Reference, counter and working electrode are housed in the same compartment.

The choice of the Polypropylene material avoids any undesired reaction with the inner electrodes (mainly the two Lithium wires that work as reference and counter electrodes). A Polypropylene cell based on the original design of Molecular Imaging Corporation was also used (Figure 3-7).

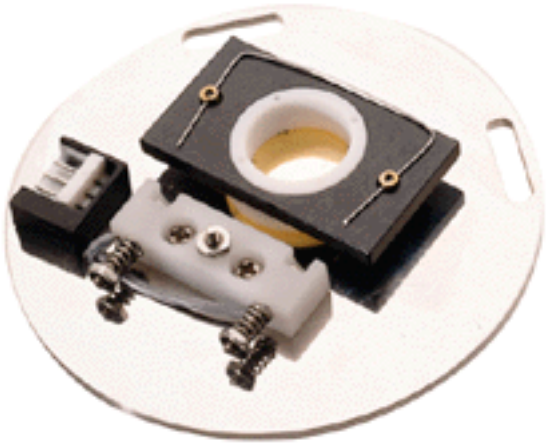

Figure 3-7: Electrochemical cell fitting the PicoSPM instruments. Two springs are used to fix the reference and counter electrodes to the cell. Electrical contacts are provided with the three pin jack visible on the left. To prevent a short circuit among the three electrodes, the bottom of the cell is isolated from the metal supporting plate by a sheet of mica.

Special efforts were spent to dry the cells. The routine procedure that was adopted consists of heating the Polypropylene cell at 80°C for 4 days under

vacuum in a Gallenkamp vacuum oven OVL-570-010J (Fision Instruments). Then the cell was directly transferred into a glove box filled with Argon (dew point -80°C). Here, the reference and counter electrodes were assembled as soon as the cell was planned to be used.
The reference and the counter electrodes were from Lithium. A Lithium wire (2 mm ∅) was scratched with a knife until the surface was bright. Then, a piece of wire was pushed into the reference compartment and a Pt wire was connected to the Lithium as current collector.

3.2 SPM instruments

Two commercial instruments were used for SPM experiments. An Autoprobe CP (Thermomicroscope Corp.) and a PicoSPM (Molecular Imaging Corp.).
The Autoprobe CP system consists of three principal components:

- Base;
- electronics module (AEM);
- Computer with monitor and keyboard for data acquisition.

The computer, an Intel Pentium (166 MHz) CPU, was connected to the AEM module and to the Potentiostat through a GPIB interface.
Since external vibrations can influence the SPM measurements, the base of the Autoprobe was put on an IsoStation VH 3648 table (Newport Corp.). This vibration isolated workstation resulted to be essential to cut the 20-50 Hz floor vibration frequency which is common to multi-floor buildings. The anti vibration system is based on the IsoStation pneumatic isolators which provide very effective isolation of vibration frequencies above 5 Hz. Four pistons pointed on flexible rolling diaphragms support the table.
The main characteristic of the Autoprobe CP are a 20-bit electronics which ensures a sub angstrom resolution also with a 100μm scanner and the direct access to the most of the electronic signals which enables a personalized configuration of the system.
The full system is shown in Figure 3-8.

Figure 3-8: Autoprobe CP system (Thermomicroswcopes Corp.). A base module, which houses the probe and the scanning unit, seats on a vibration isolated table. The base is connected to the AEM electronic module, the acquisition computer and the potentiostat.

Depending on the system configuration in use, the Autoprobe CP allows taking images with many different techniques, including contact AFM, non contact and intermitted contact AFM, lateral force microscopy and STM. All the above scanning techniques can be applied in air as well as in liquid.

For part of the experiments in non-aqueous electrolytes and for the electrical measurements we used a PicoSPM scanning unit. This system was equipped with three environmental chambers, which encloses sample and probe allowing controlled atmosphere and humidity. A two port chamber in Pyrex (diameter 10.5 cm) was used to perform current sensitive AFM under Nitrogen. The assembling of the cell under controlled atmosphere was ensured by a glove box in Plexiglas. A PicoAPEX six port chamber (diameter 15 cm) in Pyrex was used to move the scanning unit into the PicoIC acoustic isolated chamber to ensure adequate protection against external undesired vibrations.

The scanning unit is shown in Figure 3-9.

Figure 3-9: PicoSPM scanning unit. The in situ SPM cell is housed in a Pyrex cylinder. Two gaslets, which are visible in the front of the cylinder, enable exchange of the atmosphere. A piezo scanner provides the movement of the probes from the top of the cell.

The PicoSPM unit was piloted through an electronic interface by an AEM electronics (Park Scientific Instruments), connected to an Intel 486 (100 MHz) computer for data acquisition.

The main advantages of this instrument are the scanning of the tip instead of the sample which allows more flexibility in the electrochemical cell design, the current sensitive AFM mode (CSAFM) to study the conductance behavior of the sample, and a set of well designed environmental chambers which allow an easy control of the atmosphere without any risk for the instrument itself.

Since both instruments were piloted with similar electronics, the same software package could be used for data acquisition and image processing of the resulting raw data.

3.2.1 Cantilevers

Two types of cantilevers were used for in situ AFM measurements: Ultralevers□ ULCT-AUMT and Microlevers□ MSCT-AUMT purchased by Thermomicroscope.

Ultralevers consist of a Silicon cantilever triangular beam (0.6-1 μm thickness) with integrated Si conical tip. The top of the cantilever is gold coated for increasing the reflectivity. The typical radius of curvature of the tip is 100 Å and the tip is 4 μm long. Four cantilevers, which differ in spring constant and resonant frequency, were available. Mechanical characteristics are summarized in Table 3-1.

Cantilever type	A	B
Cantilever length, l, μm	180	180
Cantilever length, w, μm	18	36
Cantilever thickness, μm	1.0	1.0
Resonant frequency, KHz	19	19
Force constant, N/m	0.03	0.06

Table 3-1: Mechanical characteristics for Ultralevers (Data sheet by Thermomicroscope).

The ultralever B was used especially for in situ experiments, because it provides the highest optical signal to noise ratio.
Ultra sharp Microlevers are made of Si_3N_4 beam with an integrated pyramidal tip. The top of the microlever is also gold coated and the typical tip radius is 200 Å. The tip is ca. 3 μm long. Up to five triangular cantilevers different in spring constant were available. A rectangular cantilever optimized for LFM measurements was also available. Mechanical characteristics are summarized in Table 3-2.

Cantilever type	A	B	C	D	E	F
Cantilever length, l, μm	180	200	320	220	140	85
Cantilever length, w, μm	18	20	22	22	18	18
Cantilever thickness, μm	0.6	0.6	0.6	0.6	0.6	0.6
Force constant, N/m	0.05	0.02	0.01	0.03	0.1	0.5

Table 3-2: Mechanical characteristics for Microlevers (data sheet by Thermomicroscope).

The microlever A was used for in situ experiments because of the best mechanical stability during scanning in liquid.
Two types of cantilevers were used for CSAFM measurements. The first type is based on a triangular cantilever made of Silicon and equipped with a very sharp conical tip and it was purchased from Molecular Imaging Corp. (Part number 62-011). The typical radius of curvature of the tip and the cone angle are less than 1000 Å and 20°, respectively, while the tip height is 7 μm. The major mechanical characteristic of the cantilevers are summarized in
Table 3-3.

Cantilever type	A	B
Cantilever length, l, μm	290	110

Cantilever length, w, μm	40	40
Cantilever thickness, μm	1.0	1.0
Resonant frequency, KHz	10	140
Force constant, N/m	0.12	2.0

Table 3-3: Mechanical specifications of the first type of cantilevers (data sheet by Molecular Imaging).

To allow good electronic conductivity, tip and lever side of the chip are coated with Pt. The thickness of the Pt film is 800 Å. The specific resistance of the Pt film is ca. 30 $\mu\Omega$ cm. This first group of cantilevers was characterized by a very good mechanical stability, but also by a quite critical conduction behavior. From tip to tip the specific resistance was changing too much to reproduce the similar results.
To overlap this problem, Pointprobe® sensors (Nanosensors GmbH) were also used. The Pointprobe sensor consists of a single crystal silicon cantilever with integrated single crystal Si tip. The tip is pointing into the <100> direction. A single crystal Si holder supports the cantilever and the tip. The tip is shaped like a polygon based pyramid. The half-cone angle is better than 10° at the apex. This shape changes at the apex of the tip. In the last 200 nm the vertex angle goes virtually to zero enabling good imaging resolution also on rough surfaces. The typical tip radius is 100 Å. Mechanical properties are summarized in
Table **3-4**.

	minimum	maximum
Cantilever length, l, μm	445	455
Cantilever length, w, μm	45	55
Cantilever thickness, μm	1.5	2.5
Resonant frequency, KHz	9	17
Force constant, N/m	0.07	0.4

Table 3-4: Mechanical properties of Pointprobes (data sheet by Nanosensors).

To increase the electron conductivity tip and cantilever are coated with a thin layer of Pt/Ir. Pt/Ir coating is an approximately 23 nm thick double layer of Chromium and Platinum Iridium on both sides of the cantilever. The front side coating enhances the conductivity of the tip and allows electrical contacts. The backside coating enhances

the reflectivity of the laser beam by a factor of two. The coating process is optimized for stress compensation and wear resistance.

3.3 SPM methods

3.3.1 Scanning Tunneling Microscopy

STM measurements were performed with the Autoprobe CP system. The experiments in an electrochemical ambient require control of the potential of the STM tip and of the sample simultaneously. Therefore, two working electrodes coexist in the electrochemical cell and a bi-potentiostat has to be used. The electrolytic STM configuration used is shown in Figure 3-10, schematically. In our setup the potential of the sample electrode was controlled vs. the reference electrode, while the potential of the tip was linked to the potential of the sample and hold at a constant difference. As a consequence, a change of the sample potential causes also a modification of the tip potential. The current flowing between tip and sample was converted to potential by an I/V converter, whose factor of conversion was 1 nA / 1 V.

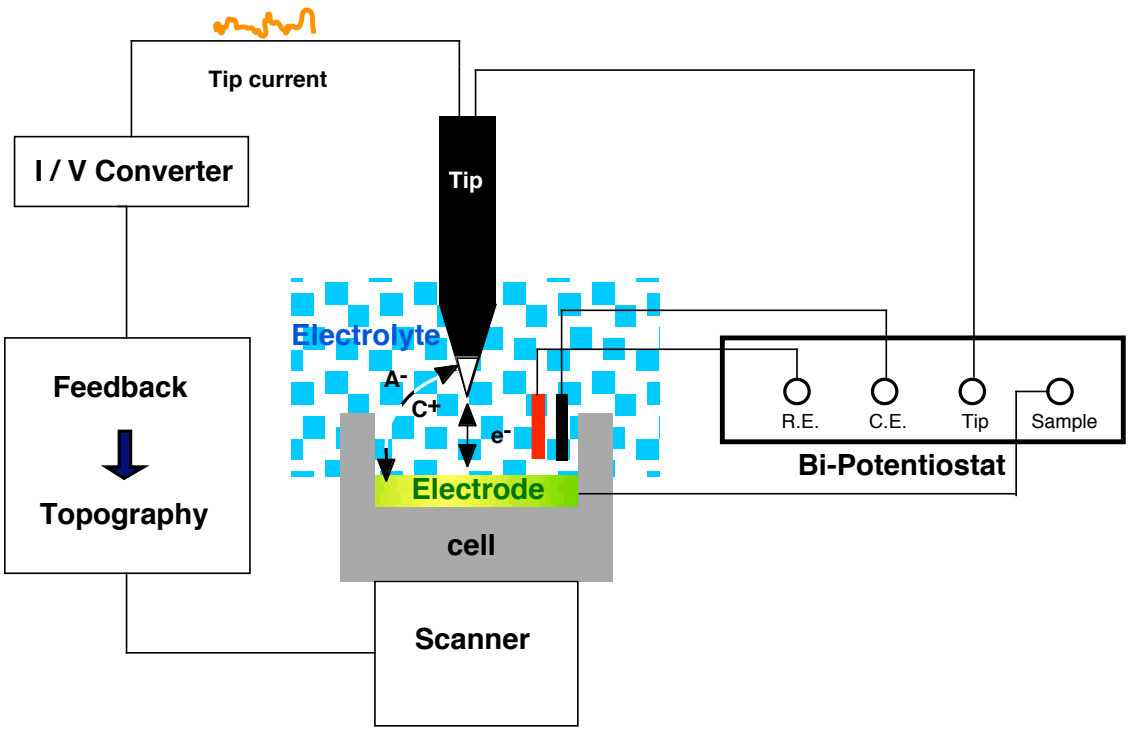

Figure 3-10: Scheme of configuration of STM in electrolyte solution. The Tip and the Sample are potential-controlled by the Bi-potentiostat. The overall Tip current is the sum of the tunneling current (e^-) and possible electrochemical currents (A^-, C^+). The Tip current is used as

feedback signal for the image acquisition. The potential of the Tip can be defined with respect to the reference electrode or to the sample.

Because of the presence of sample discontinuities, such as steps, the current between tip and sample was always kept constant and the feedback was used to compensate during the scanning of the surface in X and Y. The compensation signal of the feedback system was registered and used to generate the STM image. Only for high resolution images, i.e. when atomic resolution was required, the constant height mode was used. In this mode the feedback is not compensating the variation in Z and the output tunneling current is directly used to generate the topography signal. In such a way the noise due to the feedback circuit can be avoided. All images in liquid were acquired with bias voltage in the range 0.05-0.1 V and output current in the range 1-5 nA. The typical scanning frequency was 1 Hz and a matrix of 256 × 256 pixels was acquired for each image. Consequently, the time consumed during a single acquisition was typically 4 min and 16 sec. Two images were normally acquired simultaneously: the forward and the backward scan, corresponding to the signal from left to right and from right to left, respectively.
Since the flowing current between tip and sample in an electrochemical cell is the sum of the tunneling and the Faraday current generated at the tip, special care is required to minimize the exposed surface of the STM tip.

3.3.1.1 Etching of STM tips

STM tips for in situ electrochemical analysis were prepared by electrochemically etching a Pt/Ir wire (0.25 mm in diameter) in liquid salts. The salts solution used was made out of 10 g NaOH plus 11.7 g $NaNO_3$ which was heated up to the melting point in a nickel basket. During etching an AC voltage of 10-15 V was applied with a frequency of 2 KHz and an off set of 8 to 10 V with the negative polarity on the Pt/Ir wire. The setup used is shown in Figure 3-11.

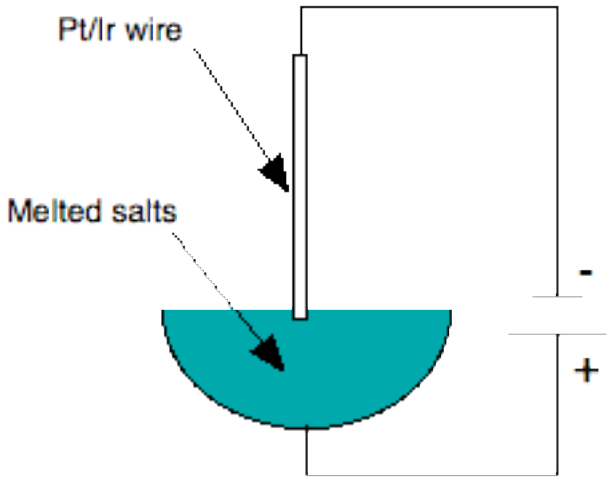

Figure 3-11: Setup for the preparation of STM tips. A Pt/Ir 0.5 mm wire is electrochemically etched in a bath of melted salts (10 g NaOH plus 11.7 g $NaNO_3$). AC voltages of 10-15 V with a frequency of 2 KHz and off set of 8 to 10 V are applied on the Pt/Ir wire.

The tip was washed in an ultrasonic bath with water. Finally, the tip was dipped in a mixture of $HClO_4$ and HNO_3 and then held in an alcohol flame to get rid of sodium on the tip.

To be used as probes in the electrolytic STM, the tips were covered with a thin layers of Apiezon® W wax (M&I Materials Ltd), a hard sealing used in Vacuum technology. By means of a tool mounted on an Ersa® Digital 80 A solder, the wax was heated to his melting point (130°C) and held at that temperature for about 20 minutes to stabilize the viscosity. Then the tip is driven through the thin wax liquid membrane and a thin layer is transferred to the wire. Because of the tension forces of the liquid, the very last apex of the tip is not covered.

3.3.1.2 Calibration of the Tip-Sample bias potential

To be sure that the potential applied between tip and sample is exactly corresponding to the value desired, the bias voltage has to be calibrated. For this purpose, the parameter E_{TIP}, which indicates the bias applied to the tip vs. the sample, is plotted as a function of the $E_{measured}$(Tip;Sample), that corresponds to the potential difference measured with a Voltmeter between the tip and the sample. The typical linear dependence is shown in Figure 3-12.

After calibrating the bias voltage, the systematic error due to the electronics of the SPM system was ± 5 mV.

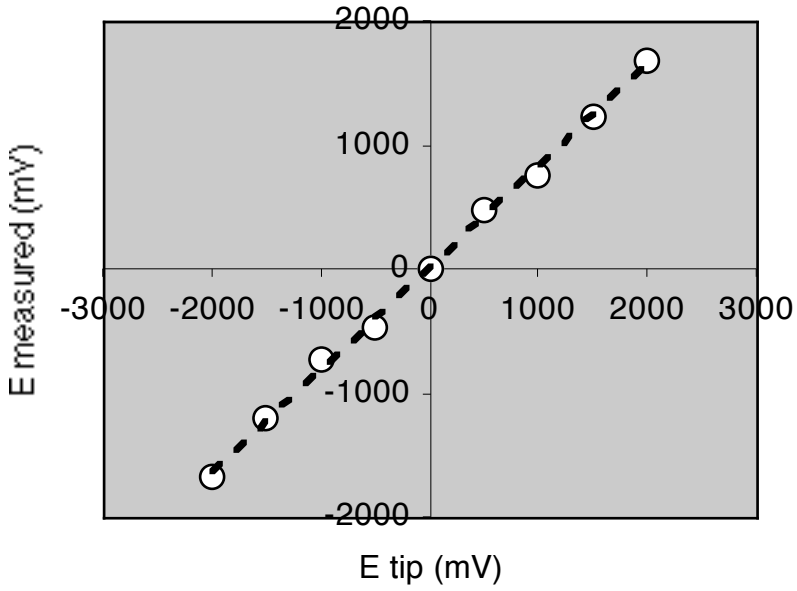

Figure 3-12: Linear dependence between E_{TIP} and $E_{measured}$(Tip;Sample). E_{TIP} is the nominal potential of the Tip as defined in the ProScan 1.5 acquisition program (Thermomicroscope). $E_{measured}$ is the difference in potential between the tip and the sample as measured by a voltmeter.

3.3.2 Atomic Force Microscopy

AFM measurements were performed in contact mode (AFM), i.e. the tip was always in contact with the sample surface during scanning. The schematic description of the setup used during in situ measurements with the Autoprobe CP is shown in re 3-13.

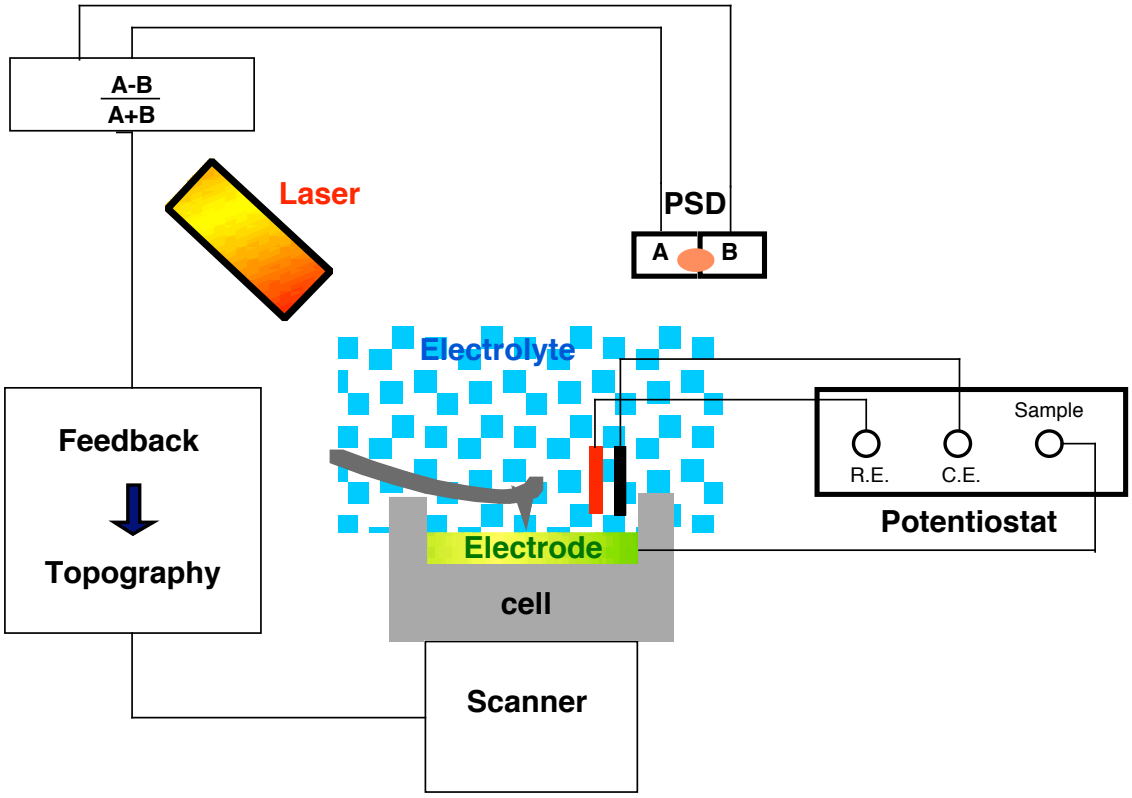

Figure 3-13: Contact mode AFM setup (Autoprobe CP); A and B are the two quadrant of the photodetector used to read out the laser deflected beam. The Potentiostat controls the sample potential. The A-B/A+B output is used as feedback signal for the image acquisition.

The procedure followed to perform an AFM measurement in liquid consists of mounting the cell on the top of the scanner through the magnetic holder and fill the cell with ca. 1 ml of liquid solution. Then the cartridge is driven down till the liquid is also covering the tip. The laser beam is realigned to maximize the A+B signal (typical values are 0.8-1.1 V) and to minimize the A-B signal at less than 100 mV. The realignment step is essential since the path of the laser beam in liquid differs from the path in air (Figure 3-14). Due to the different refractive indices for liquid and air, the laser beam changes path when the air-liquid interface is crossed.

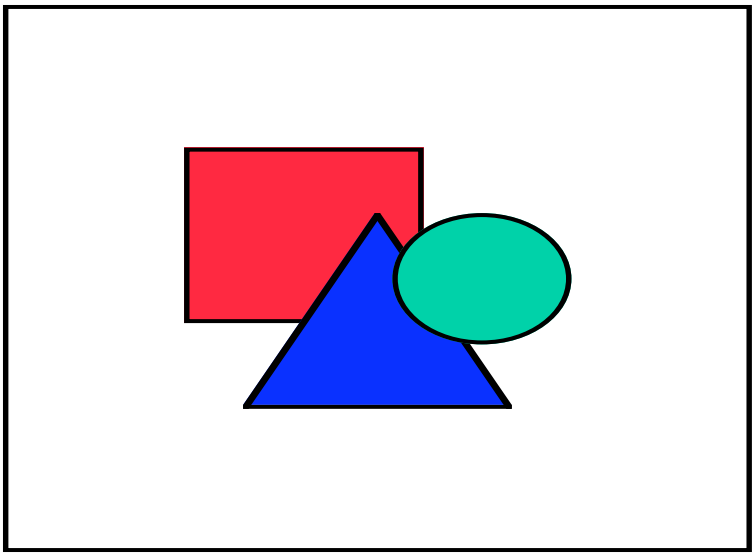

Figure 3-14: Schematic description of the optical read-out system. A laser beam is collimated to the top of the cantilever. Then, the beam is reflected to a four quadrant photodetector. The horizontal and vertical movements of the beam are proportional to the deflection and torsion of the cantilever, respectively. The change in the path of the beam when crossing the liquid-air interface is because of the different refractive index of the two media.

Depending of the liquid, the laser beam tends to drift and typically the A-B signal has to be realigned within the first 30 to 60 min. Then normally the path of the beam is stable for several hours. We succeeded to run an AFM session for up to 12 hours without loosing the signal. Different acid solutions were used during the experiments, without any corrosion problem in the cell or the cartridge.

3.3.3 Lateral Force Microscopy (LFM)

Lateral force microscopy, also called friction force microscopy, discriminates between materials by measuring their relative frictional differences through torsional deflections of the cantilever. This is a powerful method for measuring non-homogeneity in surfaces. Thanks to the use of a four quadrant photodetector, deflection and torsion of the cantilever can be easily separated by the optical read out system. The setup used is shown in Figure 3-15.

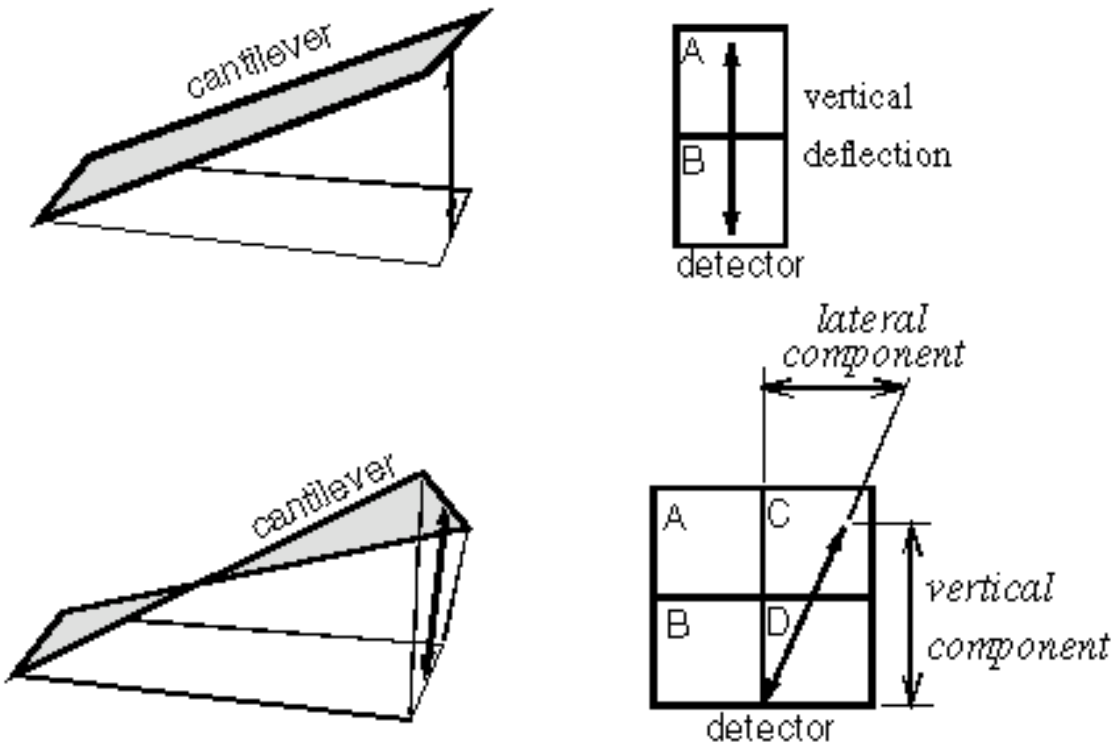

Figure 3-15: Setup used for LFM measurements; A, B, C and D represent the four quadrant of the photodetector. The top and the bottom schemes describe the effect of a vertical, respectively, torsional displacement of the cantilever on the shift of the laser beam. A-B and C-D signals are proportional to topography and friction, respectively.

By this technique, we directly probed the friction interaction between the AFM tip and the surface of the sample. As it is shown in Figure 3-16, a change in friction coefficient causes an opposite lateral force signal when the forward and the backward signals are compared.

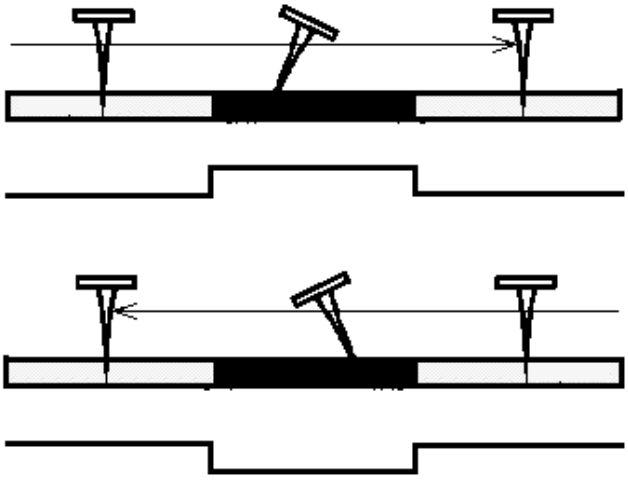

Figure 3-16: Effect of a change in friction coefficient on the lateral force signals. Forward and backward profiles show an opposite contrast.

A change in topography can affect also the lateral force mode. Anyway, in this case the forward and the backward lateral force signals are equal (see Figure 3-17). Therefore, by simply comparing the two scan directions, topography and friction changes can be easily discriminated.

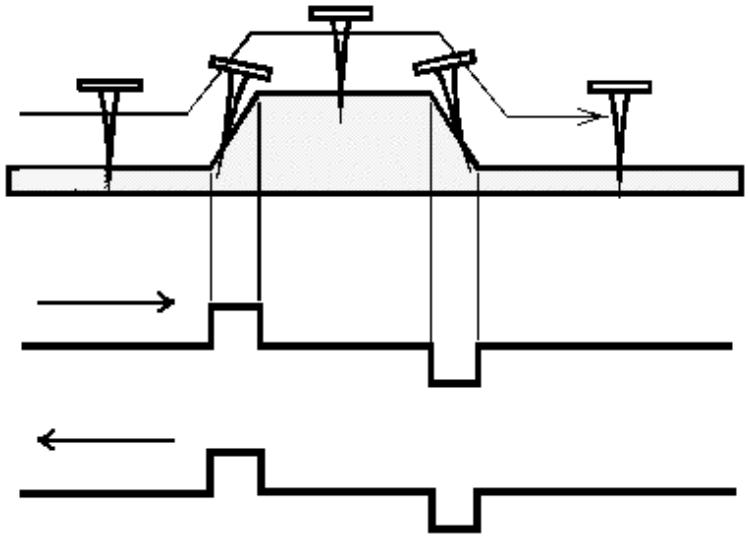

Figure 3-17: Effect of a topographic step on the lateral force signals (forward and backward). Forward and backward profiles are identical. Therefore, it is possible to discriminate between real change in friction and topography steps by comparing the forward and the backward lateral force signals.

3.3.4 Current Sensitive AFM (CSAFM)

This method consists of scanning a surface in contact mode by applying a bias voltage between a conductive tip and the sample. The deflection signals of the cantilever and the current flowing between tip and sample are recorded simultaneously. To measure the current, an I/V converter (1nA / 1V) is placed near the conductive tip.

CSAFM was performed with the PicoSPM equipped with a DC Voltage generator. A ±20 V bias voltage could be applied between the tip and the sample. The systematic error was ±2 mV. The maximum saturation current of the I/V converter was ±10 nA. The setup used is shown in Figure 3-18. When a negative bias is applied, positive and negative currents correspond to high and low conductance signals, respectively. When a positive bias is applied, the correspondence is inverted.

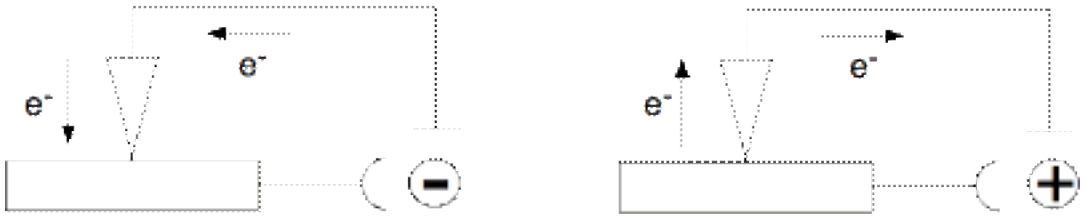

Figure 3-18: Setup used for CSAFM mode. A conductive AFM tip is biased to the sample. For a negative bias (left scheme), the higher is the current signal the lower is the resistivity of the sample. For a positive bias (right scheme) the dependence is opposite.

This method cannot be applied in liquid since the AFM tip would also generate a Faraday current which could strongly perturbate the conductance signal. All samples were measured in dry atmosphere (Nitrogen) to work at the same relative humidity. This is because the presence of a water film on the surface can perturbate the electrical investigation and a dry atmosphere helps to minimize this effect.
Local electron spectroscopy was performed by ramping the potential in a single point and recording the current produced. For sample showing a pure ohmic I / V characteristic, the resistance of the sample was calculated by the slope of the I / V plot according to the Equation 3-5.

Equation 3-5: $R = 1 / \text{slope}(V,I)$

Since the electrical output depends on the contact area of the AFM conductive tip, the same nominal loading force of 50 nN was applied to the cantilever. In order to compare the data from different samples, the same AFM tip was used. Resistance data were not renormalized vs. the contact area of the tip. As a consequence, only the relative resistance, and not the specific resistance, was always indicated here.

3.3.5 In situ measurements of dimensional changes

To measure dimensional changes during an in situ investigation, different approaches can be followed. Normally, a three dimensional image is acquired either at a constant potential or during a potential sweep. This procedure is relatively slow and non ideal when an electrochemical surface reaction has to be reproduced several times. To overall this problem, non conventional in situ scanning modes were developed to investigate the dimensional changes as a function of the potential applied to an electroactive sample [61]. They consist of recording the vertical piezo displacement vs. time in a single point or a line scan.

These techniques are of particular interest to follow thickness changes of the sample from μm to sub-nanometer range. The change of the sample thickness is measured as the change of the driving signal for the z-piezo in the direction of the surface normal, as depicted schematically in Figure 3-19.

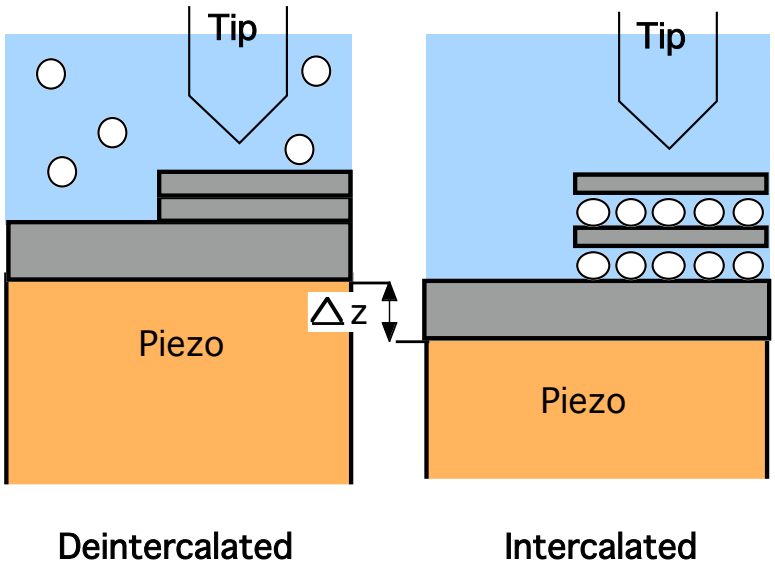

Figure 3-19: Principle of measuring changes of sample thickness. Δz is the variation of the driving signal, which corresponds, in first approximation to the change of sample thickness. In this example Δz corresponds to the difference in height of the step between the non intercalated and the intercalated phase.

3.3.5.1 tz-mode

The tz-scan method [62] offers the possibility of studying the film thickness changes at a certain location. This mode consists of holding the AFM tip in a fix X, Y position while the potential is cycled between two values at a constant sweep rate. The measurement is performed with the AFM tip in contact with the surface. During cycling, feedback indicating changes in thickness and bias of the sample are simultaneously recorded. In the resulting image the vertical axis (slow scan direction) represents the time during cycling, whereas the horizontal axis (fast scan direction) corresponds to the time of a pseudo-line scan, i.e. does not contain topographic information.

3.3.5.2 xtz-mode

The xtz-scan mode permits comparison of swelling/shrinking behavior of the film at different location along a line. Along the horizontal (x) axis, the topographic information is displayed over a fix distance, while the time is plotted along the vertical (y) axis. With this mode changes in Z at different points located on the

same line can be compared. This scan mode was particularly suitable for thickness change measurements at steps, since top and bottom of the step could be monitored simultaneously.
Since the Autoprobe CP system cannot performed a scan only in one direction, a special electronic access signal interface box was built up by Häring et al. [63]. This extra interface allows to reconfigure the circuit of the scanner to scan the tip only on a single line.

3.3.6 Measurements under controlled atmosphere

As already mentioned above, in order to perform an in situ SPM experiment in a non aqueous electrolyte, an inert atmosphere has to be used. At this purpose, the SPM base of the Autoprobe CP system was transferred into a portable Glove Box, which was small enough to fit on the anti vibrating table.
The glove box (Le Petite 815/220-PGB Model, Plas Labs Inc.) consists of an upper part formed of rigid acrylic plastic and a bottom part in Noryl® thermoplastic (figure Figure 3-20).

Figure 3-20: “Le Petite” glove box for in situ SPM investigations in inert atmosphere.

The two parts are sealed with a gel, which provides an air tight seal. Homemade gas tight electrical connections were installed in the main access door to link the inside SPM base to the outside AEM electronics.
The glove box was equipped with a free oil pump (Model D0A-V112-BN, Gast MFG Corp.) to evacuate the inner atmosphere. Dry Argon gas was supplied by a laboratory gas line. Since the glove box could work at a maximum external pressure of 1 atm, the pressure of the Argon line was always adjusted to

compensate the counter pressure of the pump. With this procedure the relative humidity could be reduce from 60% to less than 5% in approximately three hours

3.3.7 Calibration

A common problem when calibrating SPM instruments is the dependence of the sensitivity of the piezo actuators on the voltage sweep, i.e. the scan size [64]. This means that the sensitivity has to be determined for various scan ranges to obtain an overall calibration of the piezoscanner. For small scan ranges calibration is usually done by imaging crystalline surfaces as, for example, HOPG or mica [65, 66]. In order to calibrate the SPM system in X,Y directions, the structure of the HOPG surface was resolved at atomic level. The 0.246 nm pitch of the graphite and the hexagonal geometry of the unit cell were used to find out the right sensitivities of the piezo scanner, according to a procedure developed years ago [67], which eliminate the effects of thermal drift in a first order approximation. The characteristic lattice structure of the HOPG is shown in Figure 3-21.

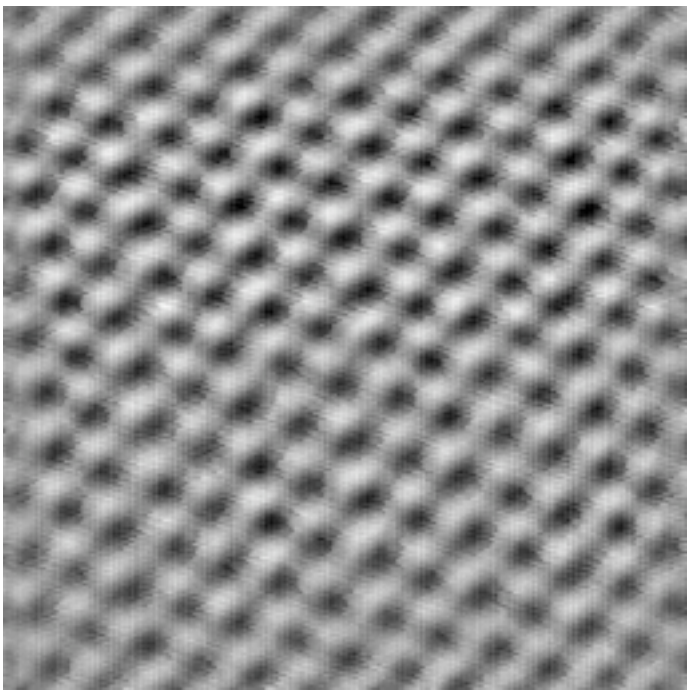

Figure 3-21: STM image of the HOPG surface at atomic resolution (size 50 □ 50 Å).

For calibration of the SPM system in Z direction, different reference samples were used. Since the piezo scanner can be driven in low voltage mode from angstroms to 1.2 μm and in high voltage mode from 1.2 μm to 7.5 μm, two different calibration

factors can be defined according to the Z range measured. For high resolution measurements, a monoatomic step on HOPG of nominally 3.35 Å was considered as calibration standard. For measurements in μm scale a SiO_2 grid with steps of 98.7 ± 0.9 nm was used as standard reference (Figure 3-22). The height of the steps was measured by ellipsometry.

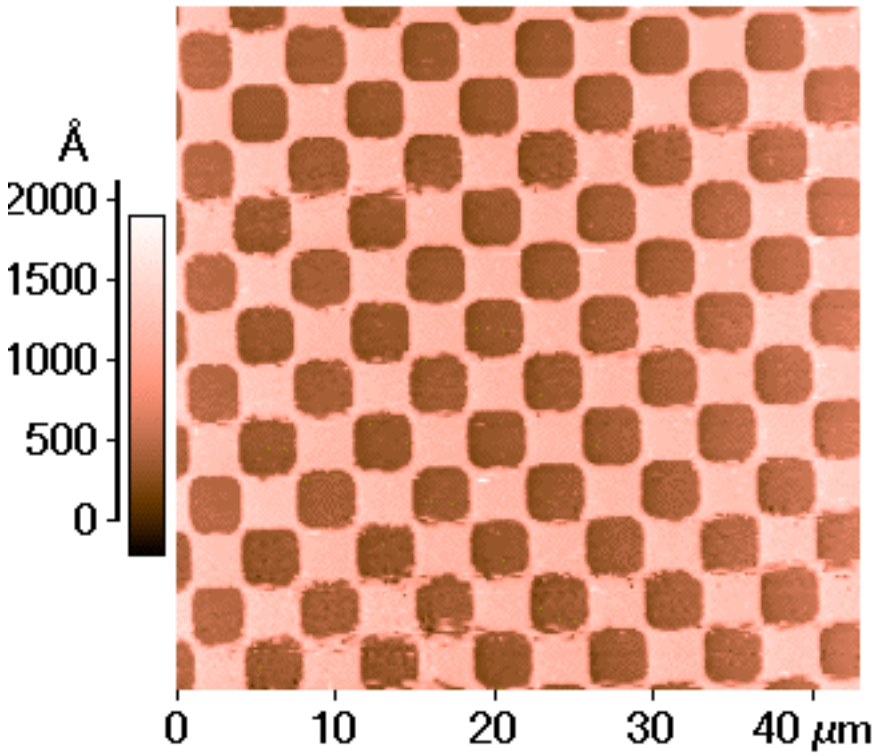

Figure 3-22: SiO_2 calibration grid imaged by AFM. The pitch of the grid is 10 μm, while the height of a step is 98.7 nm as measured by ellipsometry.

3.3.8 Evaluation of the systematic error

The SPM technique, as all the scanning methods, is subject to an indetermination, which can be quantified by the systematic error.
For the evaluation of this parameter in Z direction, three different sources of errors were considered:

- 20-bit electronics;
- calibration procedure;
- Fit correction.

To estimate the contribution of the electronics, we defined the resolution R_Z of the SPM in Z direction as the minimum distance that can be stored in one bit. The resolution R_Z can be calculated by the Equation 3-6.

Equation 3-6: R_Z = Full Range / 2exp(number of bits)

For the 100 μm scanner in low voltage mode, the full range is and the Z resolution is 0.025 Å. Therefore, the measure of a graphene layer, which is nominally 3.35 Å, is subjected to a systematic error of 0.75% (0.025/3.35). The calibration and the fitting procedures contributed also with a systematic error of 1.5% [67] and 2%[68], respectively.

By summing the single contributions in square, we estimated a systematic error of 2.61% for measuring a graphene step with the 100 μm scanner in low voltage mode.

3.4 Further analytical methods

3.4.1 Raman Spectroscopy

Raman spectroscopy was carried out at room temperature in ambient atmosphere using an Argon-ion laser source (Coherent Inc. Model Innova 70) which was tuned to 514.5 nm. After passing through a tunable laser filter monochromator (Cooke Corp., Model Laserspec 111), the beam was focused onto the stationary sample at 50° from its surface normal. Scattering light, which was collected from the sample surface at 20° from its normal and in the plane of light incident, was passed through a filter (Kaiser Optical Systems, Inc., Super Holographic Notch Filter) that was adjusted to cut the 514.5 nm laser source and focused onto the entrance slit of an ISA He-320 single monochromator. The spectral characteristic of the dispersed light were measured with a 1024 channel intensified photodiode array (EG&G PAR, Model 1420) cooled to -30°C. This device was controlled by an optical multichannel analyzer (EG&G PAR OMA III) wherein the collected data were initially processed. The monochromator was calibrated using an argon lamp (Oriel Model 6045) to provide reference frequencies. The resolution of this instrument is approximately 1.7 cm^{-1}. The power of the incident laser beam measured at the sample position was maintained at 50 mW. The possible effect of laser-induced sample degradation was investigated by comparing a series of spectra taken at different times of light excitation of the sample. No change in the shape of the spectra was detected from laser heating even upon long exposures of the sample to the laser beam.

A deconvolution analysis of the Raman spectra of carbonaceous materials was conducted to identify the individual peaks and to monitor the change in the carbon structure and crystalline parameters upon material processing. We used a

deconvolution procedure that consists of two major subroutines: background correction and nonlinear fitting. The background correction subroutine employs cubic interpolation combined with a filtering procedure. The curve-fitting function subroutine allows a choice of three typical forms (Lorentzian, Gaussian, or Voigt) to represent a vibration peak; however, the Lorentzian function was used exclusively to fit the spectra reported here.

3.4.2 X-Ray Photoelectron Spectroscopy (XPS)

XPS analysis was performed using an ESCALAB 220I XL (VG Scientific) photoelectron spectrometer (Figure 3-23) equipped with a hemispherical analyzer and a 200 W (10 KV, 20 mA) AlK_{α} x-ray source (1486.6 eV). Monochromated AlK_{α} radiation was used to improve the energy resolution. The spectra were recorder in the CAE mode with a pass energy of 50 eV for the survey scan and 20 eV for the detail scans. This pass energy results in a full width at half maximum of <0.6 eV for the Ag $3d_{5/2}$ peak. The base pressure in the analysis chamber was typically $5x10^{-9}$ mbar. The photoelectron emissions were measured at a take-off angle of 90° (normal to the surface).

Figure 3-23: Picture of the ESCALAB system.

Binding energy was referred to C 1s at 284.6 eV to correct possible shifts of the peaks. The XPS instrument was described in details in [69]. The composition of the samples was determined by quantitative analysis using the cross-section of Scofield [70].

After electrochemical preparation, the samples were removed from the electrolyte under potential control, blown dry with nitrogen and introduced into the UHV chamber. Sample treated in non-aqueous electrolytes were mounted in a home-made transfer chamber, in a glove box filled with Argon at a dew point of -80°. Then the sample was mechanically transferred from the small chamber to the main UHV chamber. In this way any exposition of the sample to the ambient air was prevented.

3.4.3 X-ray diffraction and Scanning Electron Microscopy

X-ray diffraction (XRD) was performed with a Philips X-Pert diffractometer having a copper target X-ray tube (CuK_{α}, λ = 1.54056 Å). The samples were placed on a glass support linked to the sample holder. The section of the incident beam on the sample was 5×5 mm^2. All the experiments were carried out in the reflection mode.
Scanning Electron Microscopy (SEM) was performed with a Topcon ABT-100 electron microscope.

3.5 Electrode preparation

3.5.1 Graphite electrodes

Two types of graphite electrodes were used: HOPG and powder graphite.
The HOPG electrodes consist of grade STM-1 HOPG ZYH-type crystal (Advance Ceramic Corp.), as determined by XRD measurements which are shown in the Results and Discussion chapter (paragraph 4.1). The typical HOPG electrode to be investigated by the Autoprobe CP was prepared in rectangular shape, with a length and width of 3-4 mm and a thickness of 1 mm. The surface of the HOPG was freshly cleaved with adhesive tape prior to each experiment. We observe the existence of a preferential direction to remove the top graphene layer without breaking it. Whether the tape was applied in the orthogonal direction, the surface of HOPG was not perfectly cleaved, but only some fragments were removed.
When an acid solution was used as electrolyte, the total side faces of the sample were painted with an insulating varnish in order to prevent exposure of the HOPG

edge planes to the electrolyte. In case of organic electrolytes, the side faces were masked with liquid Teflon.
In alternative to the cleaving process, three methods were used to artificially create sites active to the intercalation of ions: STM lithography, laser ablation and thermal oxidation. These methods will be discussed in details in the following three paragraphs.
For some electrochemical studies in organic electrolytes, powder graphite electrodes were used. These electrodes were prepared from the synthetic graphite SFG 6 (TIMCAL AG). A slurry of graphite suspended in a solution of poly(vinylidene fluoride) (PVDF) in a 1-methyl-2-pyrrolidone was sprayed on a thick copper current collector and then dried under vacuum at 120°C overnight. The electrodes contained ca. 8 mg cm^{-2} of graphite and 5 wt.% of PVDF binder.

3.5.1.1 STM lithography

STM pulse mode lithography was performed using Autoprobe CP. The technique involves positioning the STM tip at a desired position above the sample and then applying a short duration voltage/current pulse between the sample and the tip. The configuration used for pulse mode lithography is shown schematically in Figure 3-24.

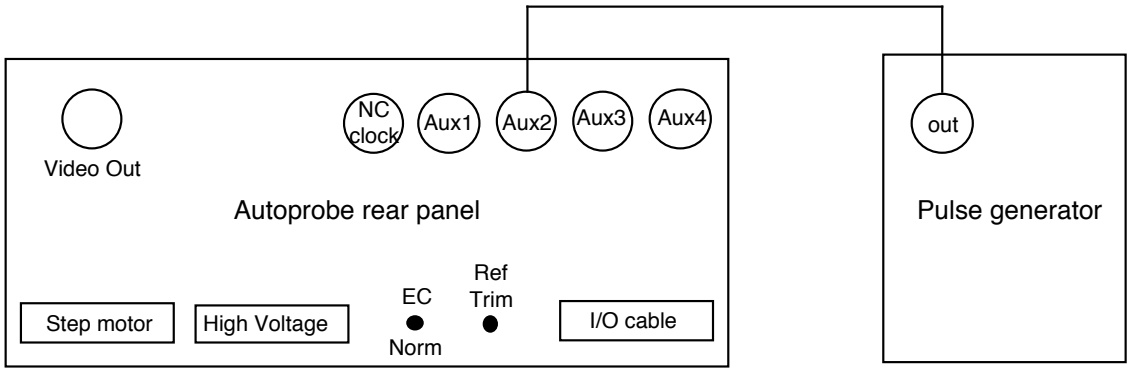

Figure 3-24: Setup for pulse mode lithography using the STM probe head and the auxiliary BNCs on the Autoprobe CP rear panel.

The pulse was applied between the tip and the sample by connecting the pulse generator output to the BNC connector labeled AUX2 on the Autoprobe rear panel. In Electrochemistry mode, AUX2 provides a direct connection to the sample.
Fresh cleaved HOPG surfaces were modified by STM pulse mode lithography. A 6 V square pulse was applied between the sample and a Pt/Ir (20:80) tip, which

was electrochemically, etched and wax coated to minimize the Faradaic current. The pulse shape is shown in Figure 3-25.

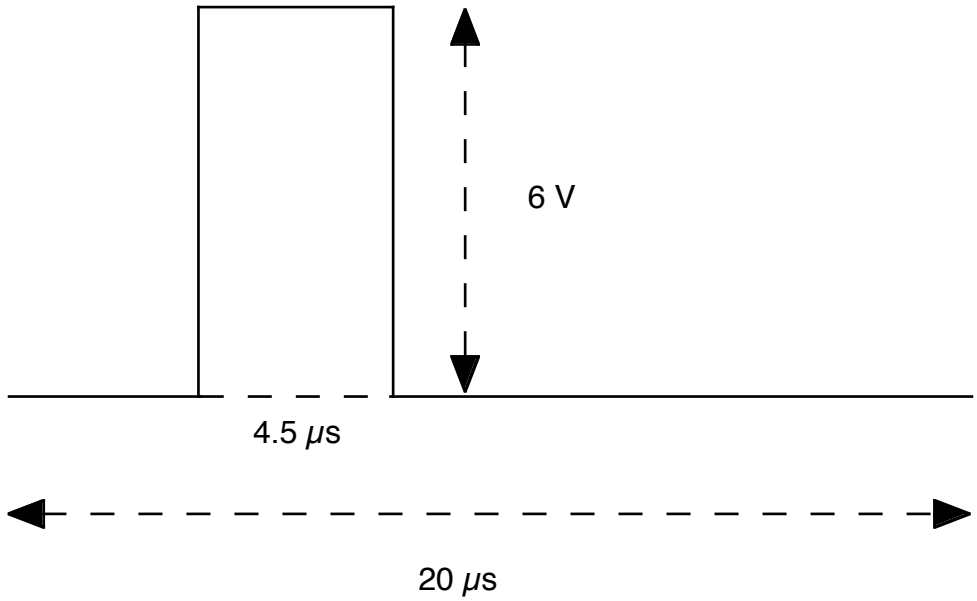

Figure 3-25: Shape of the pulse applied between the tip and the sample.

Both tip and HOPG sample were under distilled water during the lithographic process.

A 10 MHz external programmable function generator (Wavetek, Model 29) was used to generate the pulse between the sample and the tip. In this instrument waveforms are generated by Direct Digital Synthesis (DDS). One complete cycle of the waveform is stored in RAM as 1024 10-bit amplitude values. Thanks to the DDS, the frequencies can be set with high resolution from mHz to MHz and non-standard waveforms such as multi-lever square waves are easily generated.

3.5.1.2 Laser ablation method

The principle of laser ablation is based on the deposition of a high intensity laser pulse in a small volume of the sample. As a result, bond breaking occurs and the molecules are decomposed into small fragments. In Figure 3-26 the principle of surface patterning by pulsed laser ablation is illustrated.

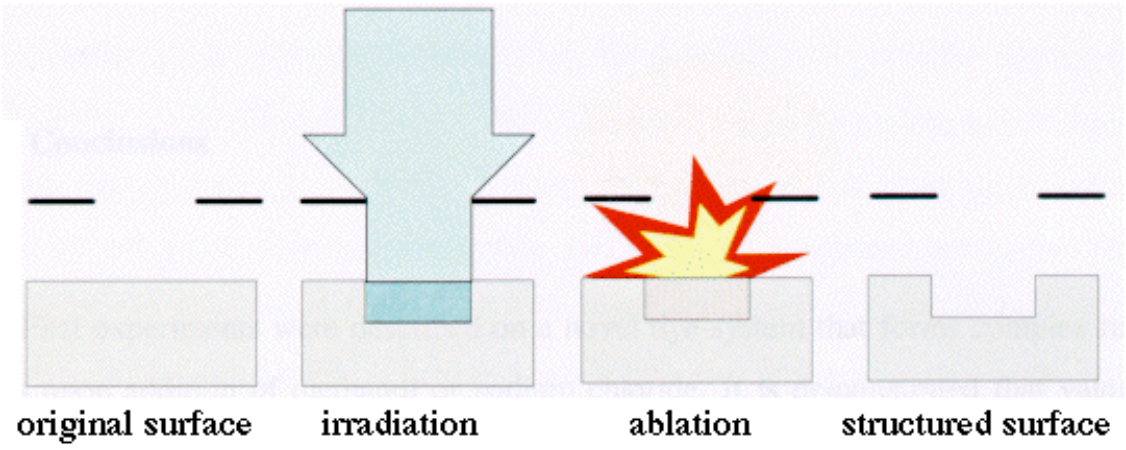

Figure 3-26: Principle of surface patterning by pulsed laser ablation. The dashed line represents the mask. From left to right the scheme of the four main step of the process are described. In the first the surface was not yet irradiated. In the second, the laser beam passed through the mask. In the third, the irradiated matter exploded. In the fourth, a hole resulted.

For the ablation of the HOPG electrodes a XeCl-excimer laser (Lambda Physik Compex 205), emitting UV-light pulses at 308 nm, was used as an irradiation source [71]. A pinhole mask (diameter 4 mm) was demagnified with a coated quartz lens (f=150 mm) onto the surface of the sample, resulting in a hole with a diameter from 15 to 250 μm. The laser was operated at a frequency of 5 Hz. A pneumatic shutter was used to deliver a well defined number of pulses onto the sample. The irradiation energy was varied with a dielectric attenuator. The pulse energy was measured with a pyroelectrical joulemeter (Gentec 200) just before the irradiation experiments. The irradiated area of the sample was measured on an irradiated thermo printing paper using an optical microscope. In addition, the area was controlled with a surface profiler (Dektak 8000), by scanning the ablated circular crater. With the setup described above, a matrix of 10×10 holes was ablated onto the HOPG electrodes with the laser under ambient conditions.
The experimental setup used is shown in Figure 3-27.

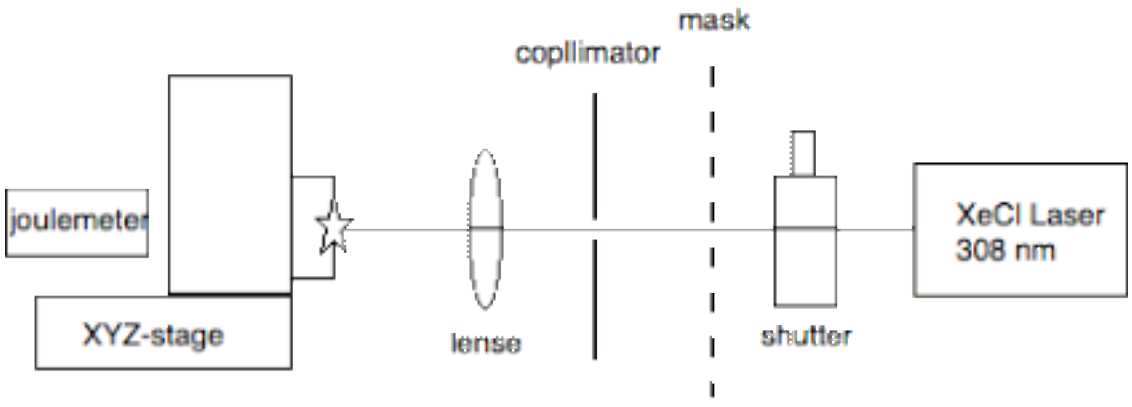

Figure 3-27: Setup employed for ablation experiments. The laser beam is attenuated by a shutter, collimated and focused on the sample surface where the interaction with the matter results in a micro-explosion. A joulemeter is used to measure the intensity of the laser beam. An XYZ stage is used to position the sample. A mask is used to produce the desired pattern on the surface.

3.5.1.3 Thermal oxidation

HOPG electrodes were thermally oxidized in a furnace (Nabertherm®, Program Controller S27), the temperature of which was controlled to ± 5°C. Typically the surface of the HOPG electrode was fresh cleaved and immediately introduced in the furnace to be heat for 30 min in air at 800°C. Once removed from the furnace, the hot sample cooled down at ambient atmosphere.

3.5.2 Carbon films

Carbon electrodes were obtained by pyrolysis of photoresist on silicon wafers. The carbon films were prepared in the Microfabrication Facility in the Electronic Research Laboratory of the campus of the University of California at Berkeley. Two photoresists were used in this study: XPSU negative photoresist (Shipley Corp.); OiR 897-101 positive photoresist (Olin Corp.).

Chemical analysis to determine the composition of the photoresists was not performed. However, these types of photoresists are organic mixtures based on Novolak® polymer, according to Material Safety Data Sheet information provided by the manufacturers.

The negative photoresist was spin coated onto 10 cm diameter silicon wafers. Plasma enhanced chemical vapor deposition (PECVD) was used to deposit an insulating layer of Si_3N_4 on the 10 cm Si wafer. The deposition occurred at a power of 20 W, chamber pressure of 0.8 Torr, substrate temperature of 310°C, and silane:NH_3 ratio of 10:90. The deposition rate was 100 Å/min and the final thickness was 1000 Å.

One layer of XPSU photoresist was applied on the Si_3N_4/Si wafer and spinned at 3000 rpm. In such a way, a final thickness of 8-10 μm was produced. This photoresist was heated in nitrogen for 1 hr at 600°C, 800°C and 1000°C to form the carbon film [72]. The temperature was increased at a heating rate of 5°C/min and held at the final temperature for 1 h to carbonized the photoresist.

Four thin layers of OiR photoresist were spin coated on the Si wafer, without Si_3N_4 insulating layer. This photoresist was heated in nitrogen for 20 hours at 150°C,

followed by heating for 1 hour at 500°C, 600°C, 700°C, 800°C, 900°C, 1000°C and 1100°C in nitrogen to form the carbon film.
The carbonizing temperatures for both photoresists are summarized in Table **3-5**.

XPSU (negative) photoresist	OiR (positive) photoresist
	500°C
600°C	600°C
	700°C
800°C	800°C
	900°C
1000°C	1000°C
	1100°C

Table 3-5: Temperatures of pyrolysis for XPSU and OiR photoresists.

4. Results and Discussion

4.1 Characterization of the HOPG surface and step preparation

The morphology of the Highly Oriented Pyrolytic Graphite was investigated by AFM and XRD. AFM characterization revealed the presence of well defined natural steps on the HOPG surface, which was freshly cleaved by a tape. The density of the bilayer steps is at least 1 μm^{-2}. Monolayer and multilayer steps could also be revealed, but with a very low density compared to the number of bilayers. The density of monolayers is ca. 0.05 μm^{-2}, while the density of multilayer steps, i.e. steps of more than tens of layers, is ca. 0.1 μm^{-2}.

XRD characterization was performed to determine the grade of quality of the HOPG crystals used to study the intercalation processes. We measured the so called "mosaic angle" that is the full width at half maximum (FWHM) of the Cu-K rocking curve (1.54 Å is the corresponding wavelength). This term is a measure of the order of the HOPG. The lower the mosaic spread, the more highly ordered is the HOPG, resulting in a surface that exhibits virtually no steps. The typical range of mosaic angle is between 0.4° to 3.5°.

The typical diffraction pattern obtained from our HOPG samples is shown in Figure 4-1.

The presence of a (002) double peak at ca. 26.5° and at the corresponding higher orders indicates that our set of HOPG crystals consists of two types of pristine graphite:

- GRAPHITE 2H d=3.35 Å
- GRAPHITE 3D d=3.38 Å

From the position of the (002) peak in the X-ray diffractogram, the layer distance "d" is determined using Equation 4-1 [73], which correlates the "d" interlayer distance with the "T" glancing angle.

Equation 4-1: $\lambda = 2 d \sin T.$

The different periodicity in the graphene structures is due to the different sequence of graphene planes. In graphite 2H the sequence is ABABAB, while in graphite

3D the sequence is ABCABC, where B is the graphene layers with a small shift with respect to A and C with respect to B.
The Mosaic spread was 3.5 degree, corresponding to the HOPG ZYH type. This means that the density of defects on the surface is high, that is in agreement with the step density measured by AFM.

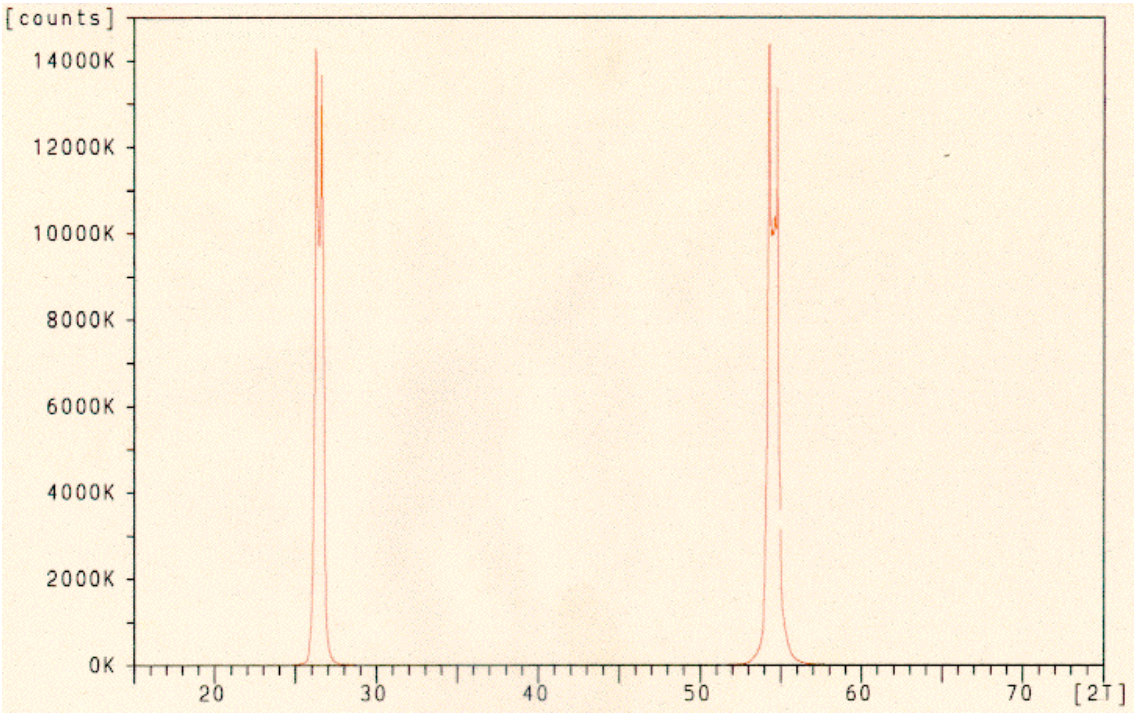

Figure 4-1: Typical diffraction pattern of HOPG samples used for intercalation experiments. 2T is the glancing angle. The double peak revealed at ca. 26. 5° and higher orders indicates that our set of HOPG crystals consists of two types of pristine graphite 2H and 3D. The corresponding interlayer distance is 3.35 Å and 3.38 Å, respectively.

In alternative to natural steps, three different methods were considered to create artificially new sites for intercalation of ions: STM nano-fabrication; laser ablation; thermal oxidation.

4.1.1 STM nano-fabrication

Holes or hills can be created onto the HOPG surface by applying voltage pulses with a STM, according to the procedure developed by Penner et al. [74,75], already described in the experimental chapter. In agreement with Penner's work, we observed a pulse threshold of about 4 V for HOPG in H_2O liquid. With smaller voltage pulses, no modification of HOPG surface was observed. With voltage pulses larger than 4 V, we succeeded to modify the HOPG surface in about 50 % of tries. In this case, the surface of HOPG exhibits hills and holes. When the

voltage of the pulse is enlarged, also the probability of modifying HOPG increases. For instance, a hole created on the HOPG surface is shown in Figure 4-2.

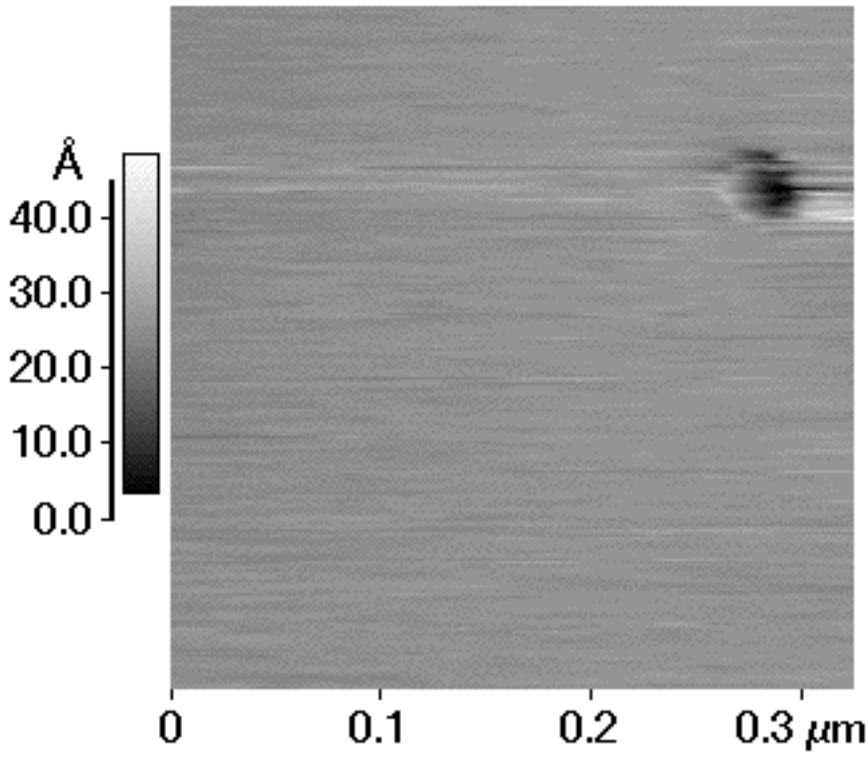

Figure 4-2: STM image of a hole created on an HOPG surface by applying a 6 V pulse, 10 μs long. The hole is 40 nm wide and 2 nm high. Tunneling current 2 nA. E_{bias} 50 mV.

The hole is 40 nm in width and 2 nm in height, which is corresponding to 6 HOPG layers, for a 6 V pulse, 10 μs duration.

By applying a sequence of 5 V pulses for 10 to 50 μs, several hills were produced (Figure 4-3). The bigger one is about 30 nm in width and 6 nm in height and it was obtained after application of a 50 μs pulse. Shorter pulses generated smaller hills.

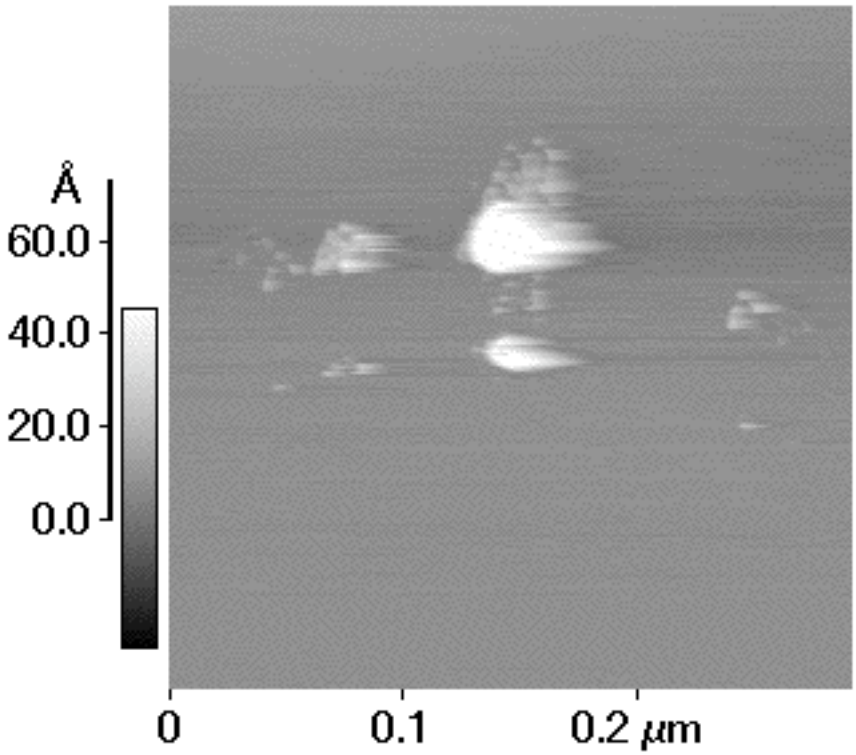

Figure 4-3: STM image of hills created on an HOPG surface by applying 5 V pulses, form 10 to 50 μs long. Tunneling current 3 nA. E_{bias} 50 mV.

Despite this method allows creation of holes on HOPG in situ, the process cannot be very well controlled and several times the result of the applied pulse is a hill instead of a hole.

4.1.2 Laser ablation

Holes can also be created on the HOPG surface by laser ablation technique. According to this method, the surface temperature of the target sample is instantaneously heated past its vaporization temperature through linear one-photon absorption, multi-photon absorption, dielectric breakdown and additional undefined mechanisms [76]. Lithography tests were run with the PSI laser facility.

First, the applied energy of the laser beam was correlated to the depth of the holes produced on the surface. A mask with circular holes different in width was used to vary the energy of the beam. Three series of twenty pulses at different energies were applied onto HOPG. SEM, Contact-AFM, and Profilometer (Dektak) characterized the sample modified by laser ablation.

Table 4-1 shows the correlation between the beam energy of the laser and the amount of HOPG removed from the surface, according to Profilometer and AFM measurements.

beam energy	mask width	hole depth
1.5 J/cm^2	150 □m	4 □m
7.5 □J/cm^2	25 □m	2 □m
2.5 □J/cm^2	15 □m	1.6 □m

Table 4-1: Holes created by Laser Ablation Technique. The intensity of the beam was varied by changing the aperture of the mask. For each energy intensity, twenty pulses were applied. AFM and Profilometer measured heights of the generated holes.

SEM (Figure 4-4) images showed that the surface around the holes was partially damaged by secondary waves, which were generated under the HOPG surface by the primary laser beam.

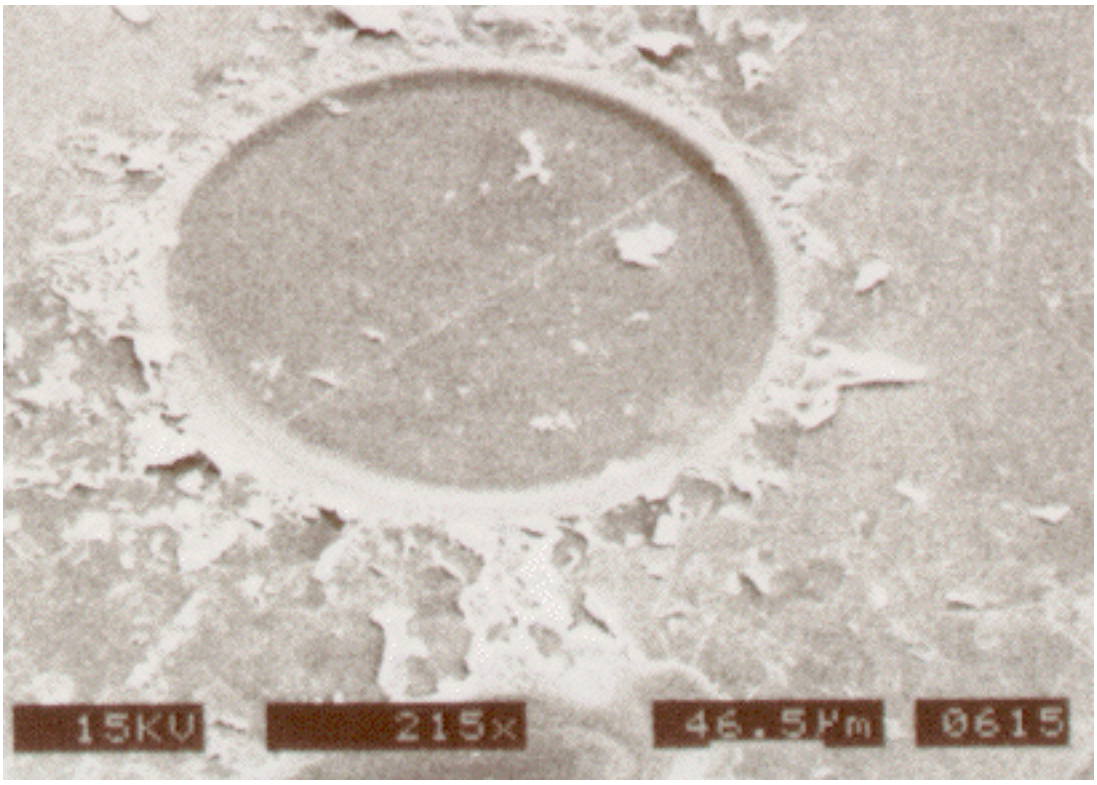

Figure 4-4: SEM image of a hole created by laser ablation of the HOPG surface; 20 pulses at 1.5 J/cm^2.

By decreasing the number of the pulses applied, also the effects of the secondary waves was of minor importance as shown in Figure 4-5.

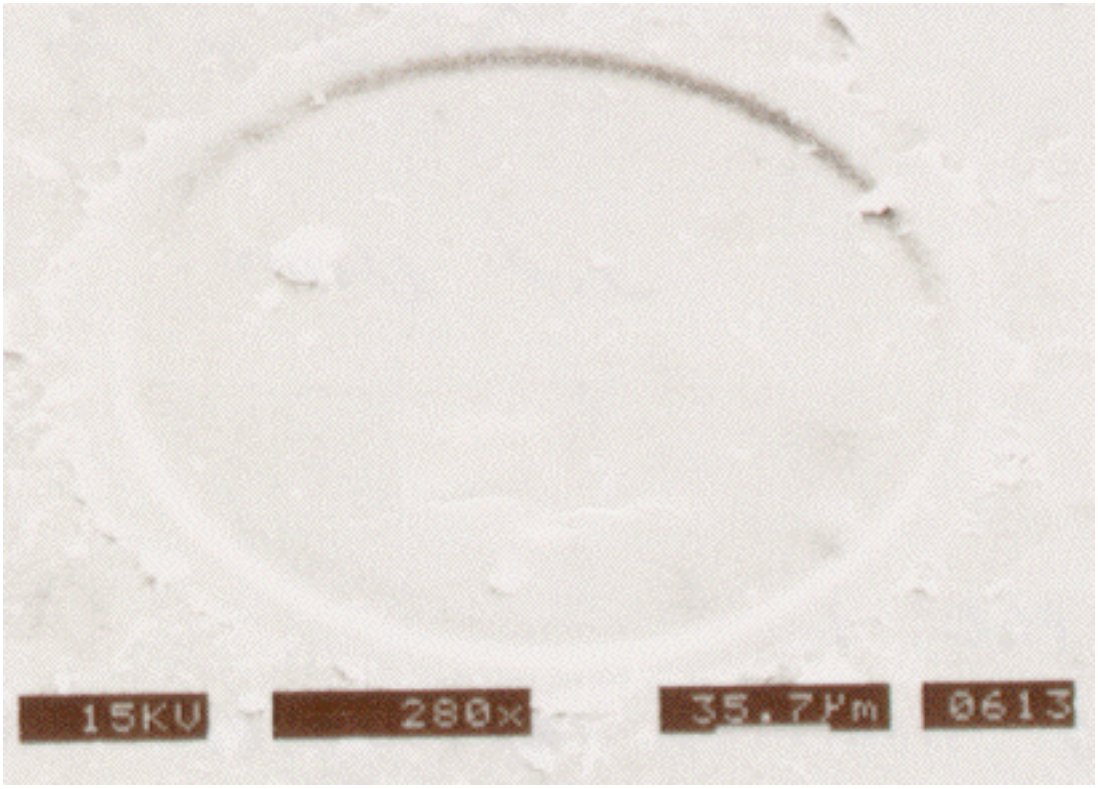

Figure 4-5: SEM image of a hole; 2 pulses at 1.5 J/cm^2.

Another way to reduce the secondary waves effects was to apply a smaller beam energy.

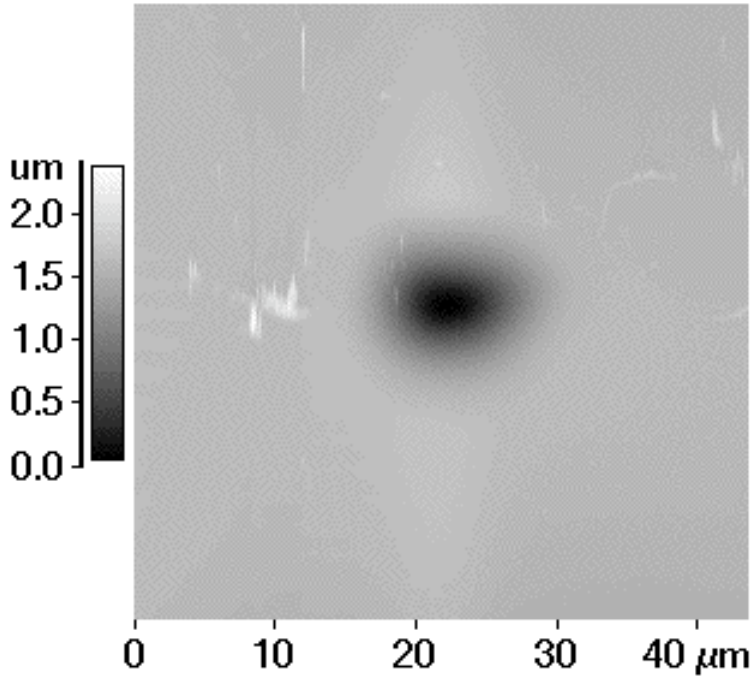

Figure 4-6: AFM image of a hole on HOPG by laser ablation; the beam energy was 2.5 μJ/cm^2. The depth of the hole is 1.6 μm. The width is 9.7 μm.

Figure 4-6 shows a 12 μm wide hole generated by a pulse of 2.5 μJ/cm^2.
Occasionally, such holes were also surrounded by cracks (Figure 4-7) of irregular shape.

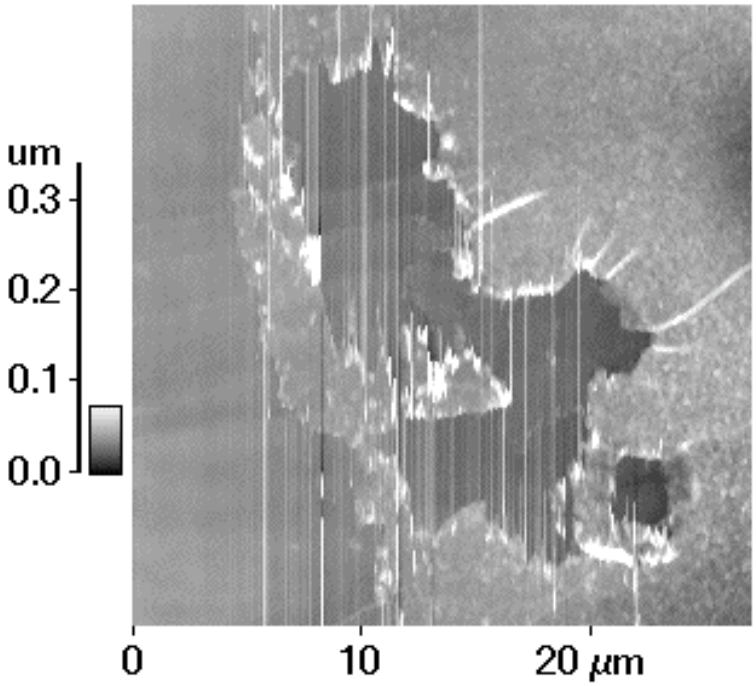

Figure 4-7: AFM image of cracks on HOPG as result of the laser ablation process. The beam energy was 2.5 μJ/cm^2.

Even considering the convolution of the AFM tip and the sample, the hole exhibited too broad edges. This means that the ablation process cannot preserve the original structure of the graphene planes at the edge of the hole. Possibly, part of them was melted and the gaps closed. Therefore, the holes generated by this method cannot be suitable for intercalating ions, anymore.
The second drawback of this method is that we could not avoid making cracks near the border of the holes.

4.1.3 Thermal oxidation

Thermal oxidation is an interesting and elegant method to artificially structure the surface of an HOPG electrode. This process leads to the removal of monoatomic carbon layers and formation of circular pits on the exposed plane. Recent works in literature [77,78] documented that the dimension of the pits can be tuned by changing the temperature and the time of oxidation. The etched pits are produced by the reaction of O_2 molecules with natural defects on graphite [79].

To study the thermal oxidation as an alternative method to create active sites for intercalation, an HOPG electrode was heated at 800°C for 30 min in air. The resulting surface was imaged by STM and AFM. The STM image (Figure 4-8) shows the presence of circular pits on different graphene planes as result of the O_2 etching.

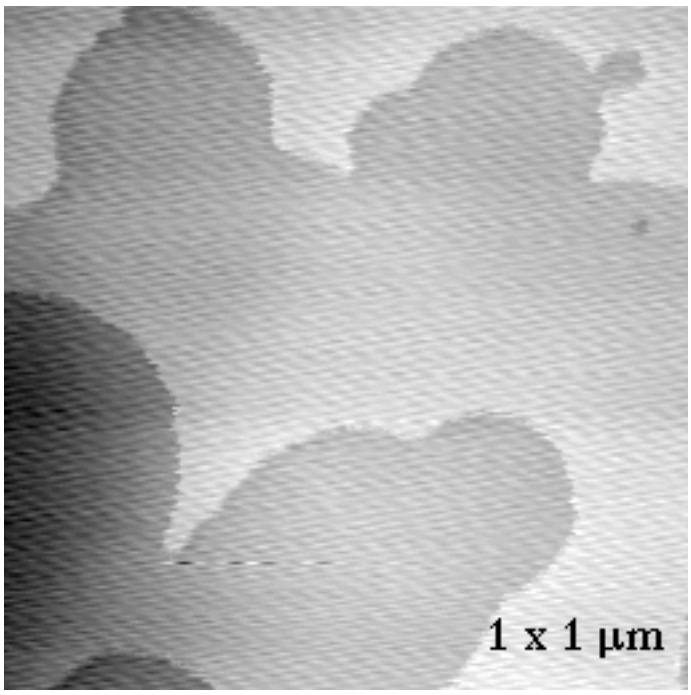

Figure 4-8: STM image of an HOPG electrode heated in air at 800°C for 30 min. I_T 0.5 nA; E_{bias} 50 mV.

Circular pits were also imaged by AFM as shown in Figure 4-9.

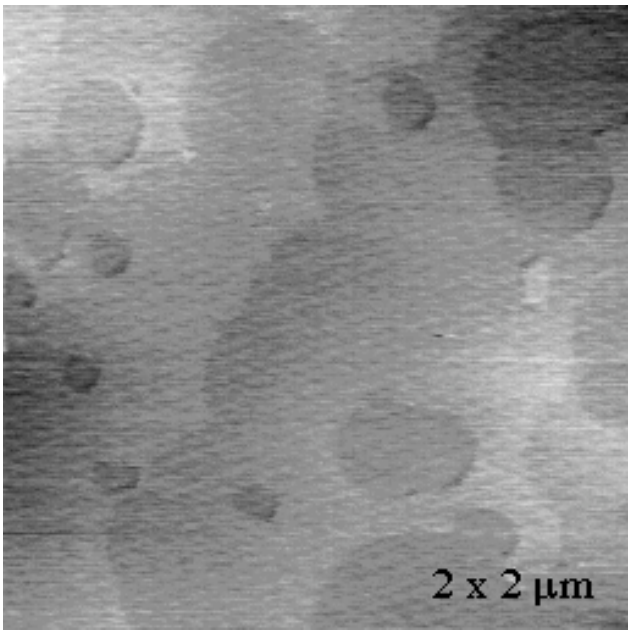

Figure 4-9: AFM image of an HOPG electrode heated in air at 800°C for 30 min. I_T 0.5 nA; E_{bias} 50 mV.

Several hexagonal holes were also localized on the HOPG surface (Figure 4-10). The diameter was about 1.5-2 μm, while the depth was between 60 Å and 650 Å.

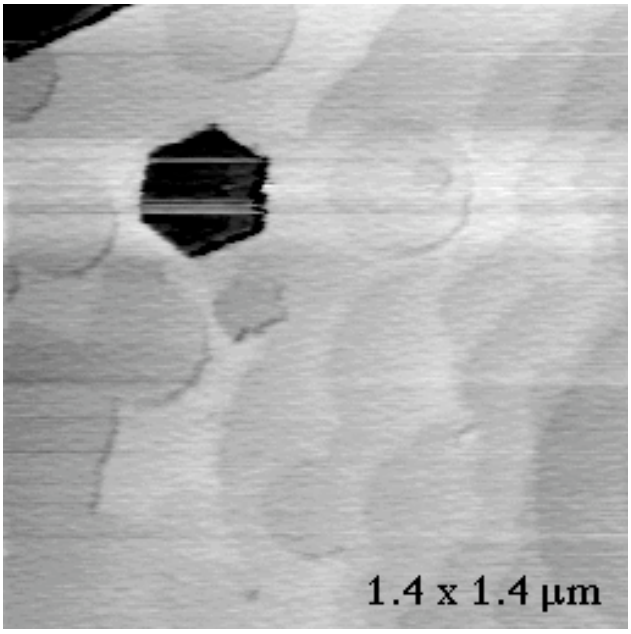

Figure 4-10: AFM image of an HOPG electrode heated in air at 800°C for 30 min.

The three methods investigated to produce artificially holes on the HOPG surface have the advantage of producing holes in a range that is ideal for an in situ SPM

investigation. In fact, the natural steps resulting of the peeling off method are normally too long to be fully imaged by an SPM, while the holes generated artificially can be imaged in the field of view of the SPM. By the way, these methods exhibited also several drawbacks and limits. The STM lithography, even being the only in situ method, is not reproducible since the most of the time hills were generated instead of creating holes. The major limit of the laser ablation and of the thermal oxidation procedures is that the sample has to be exposed to an unclean atmosphere for hours. Therefore the surface of the treated electrode normally is not enough clean to performed an electrochemical experiment. In principle a sample can be also ablated or oxidized in a UHV chamber, but in this case ad hoc expensive apparatuses have to be developed. In conclusion, the peeling off method still remains the only realistic method to prepare sites suitable for intercalating ions.

4.2 HOPG in aqueous electrolytes

HOPG was examined in perchloric and sulfuric acids to elucidate the mechanism of electrochemical anion intercalation in graphite and to develop the necessary know how, in terms of sample preparation techniques, control of intercalation processes and in situ characterization methods. Intercalation of anions from an aqueous electrolyte into HOPG can be considered a kind of “Model” system to study these electrochemical reactions. In fact, no secondary reactions, like film formation in organic electrolytes, are present.

Perchlorate ions were selected because of their excellent intercalating property at relatively low acid concentrations. Further experiments were conducted with sulfuric acid in order to see the effect of the electrolyte.

More specifically, we performed a local and time-dependent investigation of dimensional changes of the host material on the nanometer scale during the electrochemical intercalation processes. STM and AFM/LFM, combined with Cyclic Voltammetry, were used as an in situ analytical tool during intercalation and deintercalation of perchlorate and hydrogen sulfate ions through the surface of HOPG.

4.2.1 Theoretical expectations

The systems of graphite and perchlorate or hydrogen sulfate ions are of great interest as models to study intercalation reactions.

In quite concentrated acid the two corresponding intercalation processes are described by the Equation 4-2 and Equation 4-3 [80].

Equation 4-2: $C_{24} + ClO_4^- + y\ HClO_4 = [C_{24}^+\ ClO_4^-]\ y\ HClO_4 + e^-$

Equation 4-3: $C_{24} + HSO_4^- + y\ H_2SO_4 = [C_{24}^+\ HSO_4^-]\ y\ H_2SO_4 + e^-$

The number of solvated molecules per ion intercalated (y) is ca. 2 for $HClO_4$ and 2.5 for H_2SO_4 [81]. Therefore, the GICs are arranged in a two dimensional solvated structure. When a pure "hard sphere" model is considered [82], the spacing for a gap filled with perchlorate ions is 7.95 Å, while for a gap filled with hydrogen sulfate ions is 7.98 Å [81]. Therefore, the percentages of expansion of the interlayer spacing, expected upon formation of stages, are summarized in Table 4-2.

Anion	**Stage IV**	**Stage III**	**Stage II**	**Stage I**
perchlorate	34.2%	45.7%	68.5%	137%
Hydr. sulfate	34.95%	46.5%	69.1%	138.2%

Table 4-2: Percentages of interlayer distance expansion predicted by the "hard sphere" model. Stages IV, III, II, I for perchlorate and hydrogen sulfate.

When a too high anodic potential is applied, especially in low concentrated acids, irreversible side reactions can also occur. The formation of graphite oxide (Equation 4-4), carbon dioxide (Equation 4-5) and the electrolysis of water (Equation 4-6) are expected to cause substantial destruction of the graphite lattice.

Equation 4-4: $C_x + 2H_2O \rightarrow C_xO_2H_y + (4-y)H^+ + (4-y)e^-$ (x=8-12, y=1-2).

Equation 4-5: $C + 2H_2O \rightarrow CO_2 + 4H^+ + 4e^-$.

Equation 4-6: $2H_2O \rightarrow O_2 + 4H^+ + 4e^-$.

It is believed that the above side reactions can lead to formation of blister-like structures in HOPG basal planes. A model was recently proposed by Murray and coworkers [24] to explain the blister formation. In this model the authors proposed that, following intercalation of electrolyte and water into the HOPG, blisters form as

a result of electrolytic gas evolution at subsurface active sites, like crystal grain boundaries, with accompanying parallel Electrolytic formation of Graphite Oxide (EGO). A scheme of the model is shown in Figure 4-11.

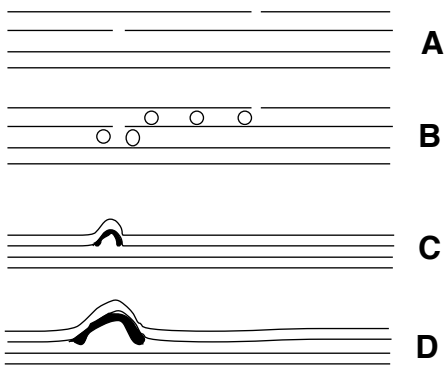

Figure 4-11: Scheme of blister formation model proposed by Murray et al. [24]. (a) Cross section of basal plane HOPG electrode/solution interface with electrode at initial potential prior to oxidation. (b) After scanning the electrode potential anodically. Intercalation of ions and water molecules has occurred. (c) EGO formation and gas evolution is started. The dark area represents electrochemically formed graphite oxide. (d) Final blister structure after scanning electrode potential back to initial value. Between (c) and (d) the blister grew due to mechanical stress attributed to gas evolution and to the expulsion of intercalated electrolyte ions during the cathodic scan.

4.2.2 HOPG in Perchloric acid

4.2.2.1 Electrochemical behavior of HOPG

Electrochemical behavior of HOPG in perchloric acid was first examined by cyclic voltammetry to obtain information about surface reactions on the HOPG. This method was selected because of its suitability for obtaining current-potential results, which are indicative of dynamic processes that occur at the electrode surface. The main intent of this study is to illustrate that acid concentration and anodic potential limit play an important role in the efficiency of intercalation.

The cyclic voltammograms obtained during the first five potential scans of the HOPG edge planes are shown in Figure 4-12 as a function of the perchloric acid concentration. The electrolytic solutions were prepared at concentrations from 0.1 M to 6 M. The HOPG working electrodes were dipped in the $HClO_4$ solutions and drawn back in order to expose only the edge planes of one side to the electrolyte (hanging meniscus). The potential of the working electrode was referred to a SME reference electrode and the scan rate was 10 mV/s.

Error! Disk Full. Free some disk space and recalculate this field.

Figure 4-12: Typical voltammograms for the edge planes of a HOPG crystal exposed to perchloric acid in different concentrations, at a can rate 10 mV/s.

Examination of the potential region 0.8-1.4 V (SME) of the cyclic voltammograms shown in Figure 4-12 indicates electrochemical processes that are related to intercalation of perchlorate ions. We have only evidence of stage IV formation for 0.1 M concentrated acid. The voltammograms acquired at 2, 4 and 6 M concentrations exhibit also the presence of stage III and possibly II, as indicated by the counter peaks in the cathodic current.

For potential higher than 1.5 V a strong formation of bubbles was observed which were possibly due to oxygen evolution or to formation of CO_2. When the potential was held too long at 1.5 V, the bubbles destroyed the electrode since they induced a strong exfoliation of the HOPG planes.

Cyclic voltammetry was repeated for 2 M and 4 M concentrated acid solutions with the "window opening" procedure, which consists in increasing the anodic potential limit of 10 mV after each potential scan. In this way the anodic peak due to the formation of a particular stage can be better correlated to the corresponding counter peak. The anodic production and cathodic reduction potentials of the intercalation stages for the above two acid concentrations are resumed in Table 4-3.

	1st peak	2nd peak	3rd peak
anodic scan (2 M)	1.150 V	1.225 V	1.275 V
cathodic scan (2 M)	0.975 V	1.025 V	1.125 V
anodic scan (4 M)	1.050 V	1.100 V	1.150 V
cathodic scan (4 M)	0.875 V	0.975 V	1.075 V

Table 4-3: Peaks resulted from cyclic voltammograms of HOPG edge planes in 2 M and 4 M $HClO_4$.

These results are in agreement with the previous work of Beck et al. [83].

Furthermore, the potential, where the anodic current begins to rise, decreases with the acid concentration. To show this effect, the onset potentials corresponding to a current density of 1 mA/cm^2 (second cycle) were plotted vs. the acid molarity in Figure 4-13.

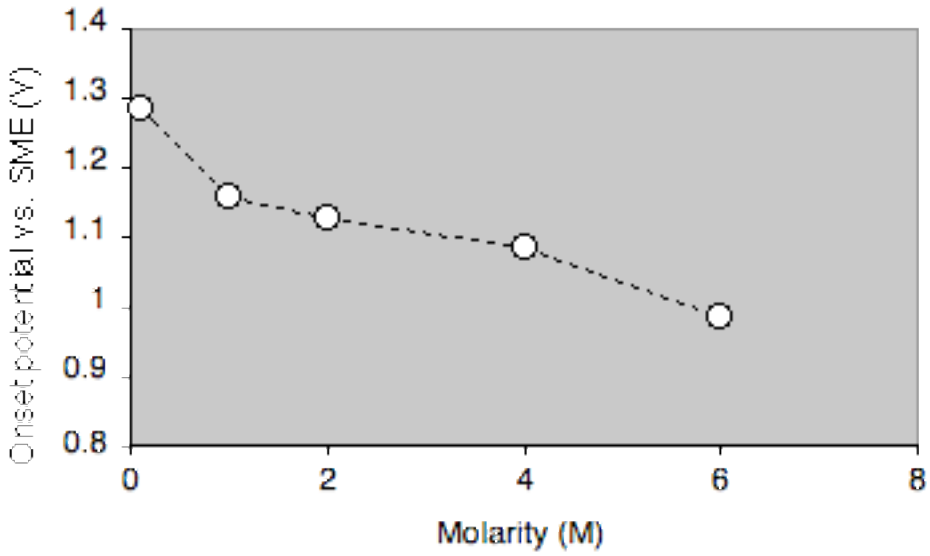

Figure 4-13: Influence of perchlorate concentration on the onset potential, corresponding to an anodic current of 1 mA for HOPG in $HClO_4$ for the second cycle. Potentials are indicated vs. SME.

By integrating the area under the anodic and cathodic part of the voltammograms, the oxidative (Q_A) and reductive (Q_C) charges were determined. Therefore, the current efficiency (Q_C / Q_A) was calculated over a wide range of acid concentrations. Evaluations were made by acquiring CV curves at the same anodic potential (1.42 V vs. SME) and considering always the second cycle. In Figure 4-14 the current efficiencies were plotted vs. the acid molarity. In agreement with the literature [21], the efficiency at 4 M concentration is 15% and 20% higher than at 2 M and 6 M concentrations, respectively.

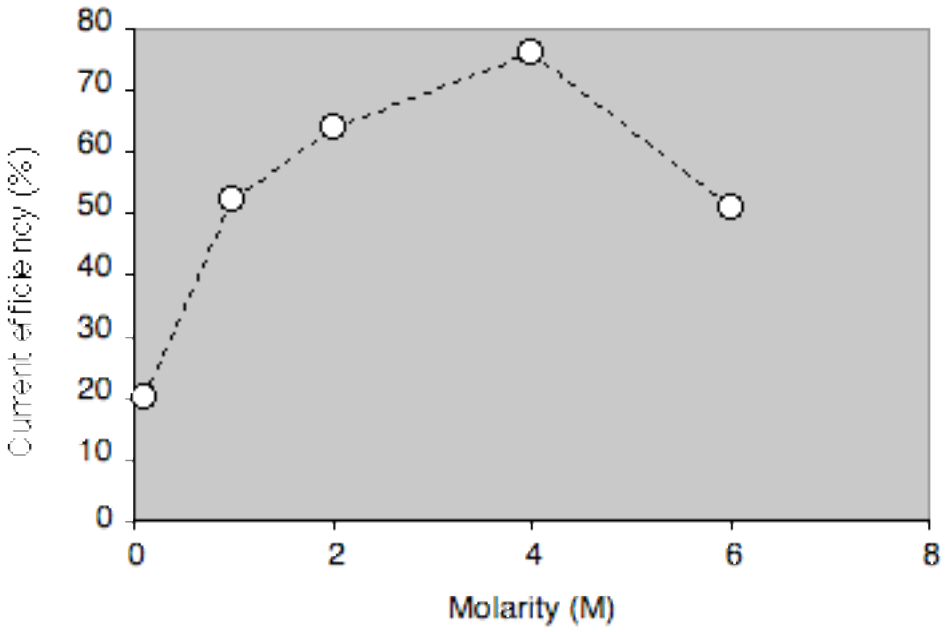

Figure 4-14: Current efficiency = Q discharge / Q charge for voltammetric curves with HOPG in different concentrations of perchloric acid. Charges were determined by integrating the area under the anodic and the cathodic part of the voltammograms shown in Figure 4-12**.**

In order to quantify the intercalation effect on HOPG, the specific capacity was measured in the double layer region (0-0.8 V vs. SME), before and after having induced the intercalation process. The edge planes were exposed to the electrolyte and the potential was cycled from –0.5 V to 0.5 V at 100 mV/s to measure the capacity in the double layer region. The intercalation and deintercalation of anions was induced by cycling for 10 times from 0 V to 1.45 V at 10 mV/s. Then, the potential was cycled again from –0.5 V to 0.5 V at 100 mV/s to measure the capacity after intercalation and deintercalation.

The specific capacity was calculated according to the Equation 4-7, where *i* is the current at 0 V vs. SME.

Equation 4-7:

$$C_{DL} = \frac{i_{anodic} + i_{cathodic}}{2 \cdot scanrate \cdot area}$$

The resulting specific capacity as a function of the acid concentration is shown in Figure 4-15, before and after intercalation.

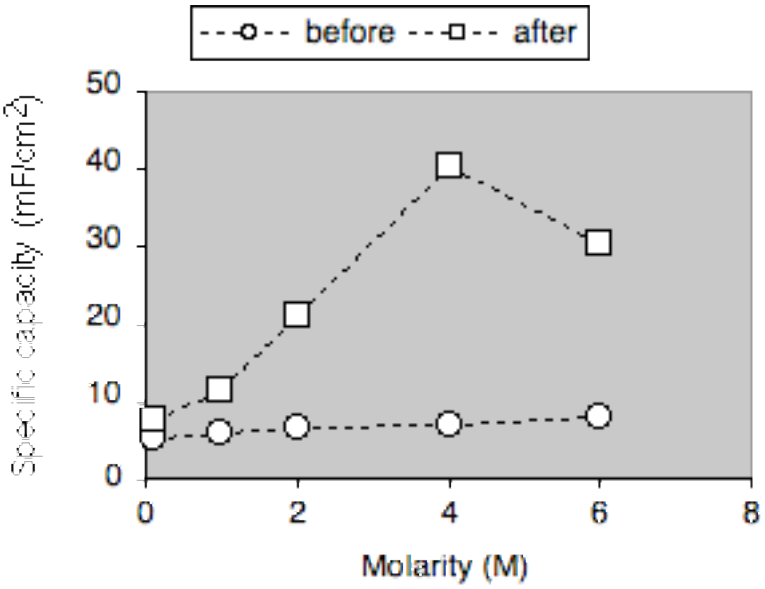

Figure 4-15: Specific capacity in double layer region before and after having intercalated and deintercalated the perchlorate ions. Specific capacity was determined by the Equation 4-7, where the current was measured at 0 V vs. SME.

The same procedure was also applied to the case of 2 M concentrated acid to study the influence of the plane geometry (basal or edge) on the specific capacity. Results are summarized in Table 4-4.

HOPG	C_{DL} before	C_{DL} after
edge planes	3000	25000
natural steps on basal plane	1.0 ± 0.4	4.1 ± 0.7

Table 4-4: Specific capacity is in $\mu F/cm^2$ and was determined by the Equation 4-7, where the current was measured at 0 V vs. SME before and after intercalation. Specific capacity is compared for HOPG edge and HOPG basal planes exposed to a solution of 2 M concentrated perchloric acid.

Cyclic voltammetry investigations on HOPG edge planes demonstrated that intercalation of perchlorate ions is favorite in concentrated acid solutions (higher than 2 M) and that the maximum efficiency is reached at 4 M concentration. The selection of an anodic limit potential lower than 1.4 V_{SME} is also important to minimize the contribution of unwanted side reactions, like CO and CO_2 production, which can even destroy the electrode.

4.2.2.2 Electrochemistry of the basal planes

Cyclic voltammetry was performed to HOPG basal plane to study the intercalation process, which occur through the natural steps on it. The purpose of this experiment is to demonstrate that the HOPG basal and edge planes show similar electrochemical behavior, in terms of stage formation efficiency. The extension of the cyclic voltammetry study from edge planes to basal planes is because the HOPG basal plane is an ideal electrode to investigate intercalation reactions with SPM techniques. In fact, such electrode exhibits very low roughness, but also many surface defects, like steps, which can be used to investigate dimensional changes correlated to intercalation processes.

For the above reason, cyclic voltammograms were acquired by using the electrochemical cell for in situ SPM measurements, which was described in paragraph 3.1.1. HOPG basal planes were exposed to a 2 M concentrated $HClO_4$ electrolyte.

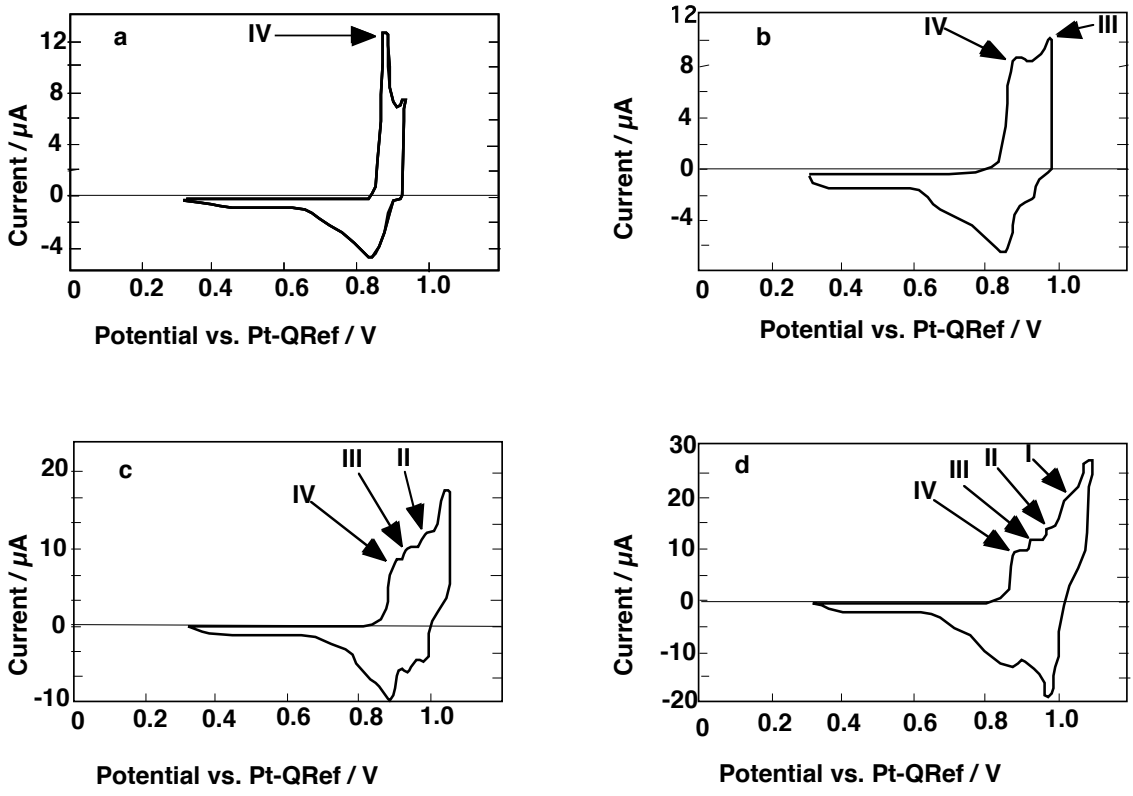

Figure 4-16: Cyclic voltammetry curves of HOPG, 100 mV/s, in 2 M $HClO_4$. Points of scan reversion vs. PtQref: (a) 950 mV; (b) 1000 mV; (c) 1050 mV; (d) 1100 mV.

This acid concentration represents a good compromise between a high intercalation efficiency and reasonable low corrosion, in order to avoid any damage of the cell for in situ SPM investigations.

As shown in Figure 4-16, different stages of graphite intercalation compounds (GIC) can easily be distinguished. Here the potentials are expressed vs. the PtQRef value.

Over a potential range of only ca. 200 mV, at least three different stages are visible in the form of anodic peaks in the positive scan and reappear as cathodic peaks in the negative scan. The stages are produced by the intercalation of anions and associated solvent or acid molecules into the graphite lattice, as described by Equation 4-8.

Equation 4-8: $[C_x] + [A^-] + y(solv.) = [C_x^+A^-]y(solv.) + e^-$

For $HClO_4$ concentrations greater than 2 M [84], the reaction above, which describes stage formation, is the only electrochemical process, until the anodic potential limit is lower than 1050 mV_{Pt}. For lower concentration of the electrolyte or for higher anodic potential limit, other reactions (graphite oxide formation, carbon dioxide formation, and water electrolysis) can take place.

The fine structures in the anodic scan of Figure 4-16 are due to the intercalation reaction, as proved by the presence of corresponding cathodic counter peaks. In Table 4-5 the oxidative (Q_A) and reductive (Q_C) charges associated with the voltammograms in Figure 4-16 are compared in order to estimate the degree of reversibility of the intercalation process.

CV	stage	Q_A ($mCcm^{-2}$)	Q_C ($mCcm^{-2}$)	Q_C/Q_A
1a	IV	2.64	2.74	1.04
1b	IV-III	4.16	4.25	1.02
1c	IV-II	7.15	5.51	0.77
1d	IV-I	10.7	7.39	0.69

Table 4-5: Charge densities in the voltammograms of Figure 4-16. Q_A is the anodic charge density between 0.85 V and the potential of anodic scan reversal.; Q_C, is the cathodic charge density above 0.3 V.

The values of Q_A were calculated by integrating the CVs in the potential range between 0.85 V and the potential of anodic scan reversal. The values of Q_C represent the total cathodic charge above 0.3 V.

Value of Q_C/Q_A of about 1 for the CVs in Figure 4-16a,b indicate a reversible intercalation process during stage IV and stage III GIC formation. For higher potentials (Figure 4-16c, d) the intercalation process is not totally reversible (Q_C/Q_A

< 1). About 20 – 30 % of charge cannot be recovered after the formation of stages II and I respectively. The additional anodic current is probably due to irreversible oxidation of the graphite.
Our results are in agreement with earlier findings [20] by Cyclic Voltammetry at natural graphite in perchloric acid.
The cyclic voltammetry study of HOPG basal plane showed that this electrode is suitable for investigating intercalation reactions in perchloric acid, because the peak structure due to the stage formation is clearly resolved. Therefore, well defined potentials can be held to perform in situ STM or AFM results can be correlated to the potential where a certain stage is formed.

4.2.2.3 In situ electrochemical STM of perchlorate intercalation

An in situ STM study of HOPG in 2 M $HClO_4$ was performed under potential control. In order to stabilize the intercalation process, the potential of the HOPG electrode was cycled between 200 mV_{Pt} and 900 mV_{Pt} for several times. When the intercalation process began to be reproducible and, therefore, controllable in terms of stage formation, the STM characterization started by imaging the HOPG electrode at a potential in the double-layer region, where anions cannot intercalate (Figure 4-17a). Then the same area was imaged after having reached the first relative maximum in anodic current and waited until no more current was flowing (Figure 4-17b). Subsequently, the HOPG potential was driven into the double-layer region to de-intercalate anions (Figure 4-17c), and so on (Figure 4-17d).
The sequence of STM images shown in Figure 4-17 is a typical example of how the morphology of HOPG surface changes because of the intercalation process. The Y-like feature visible on the surface was used as inner reference marker to be sure that we were always imaging the same area.

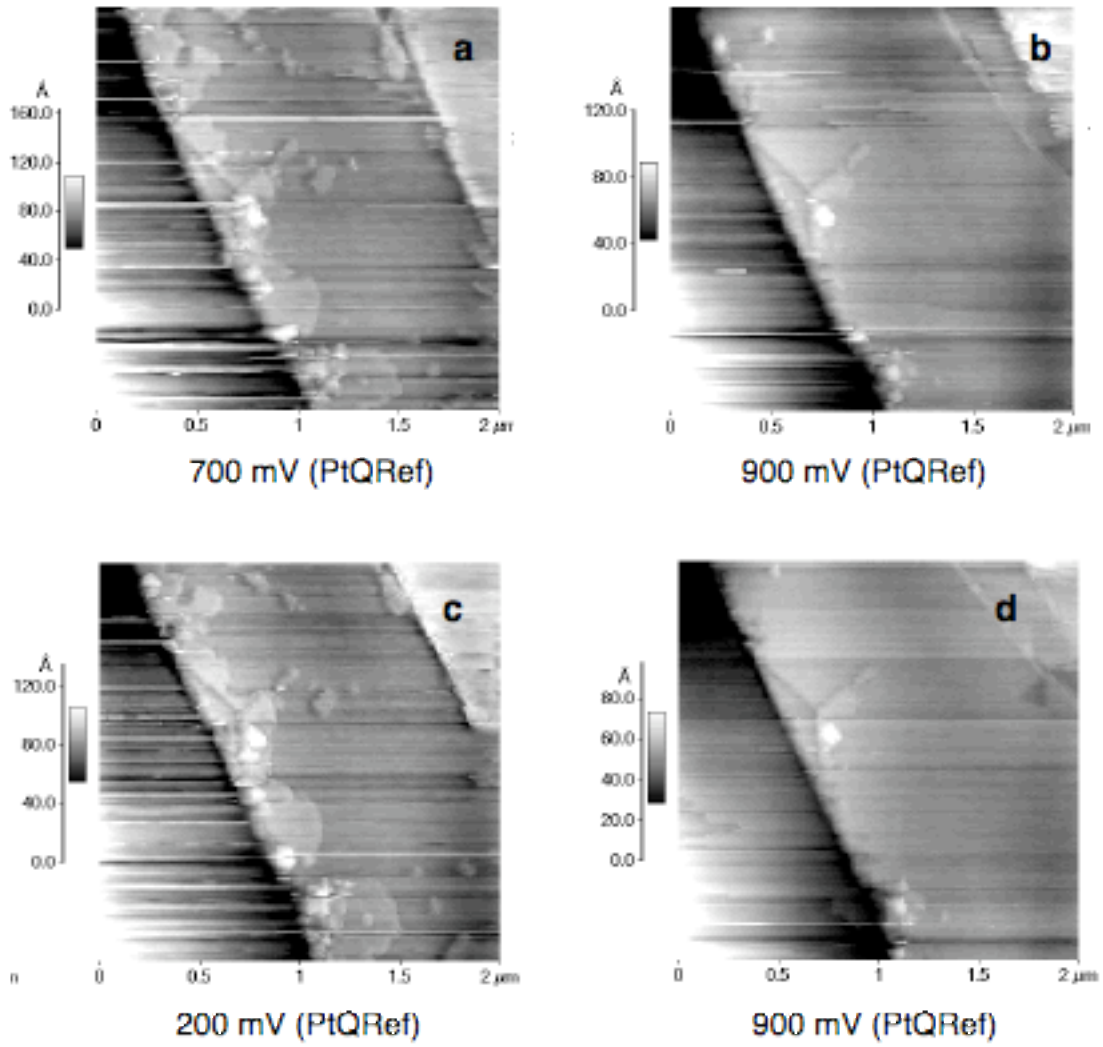

Figure 4-17: STM images of HOPG at different potentials. I_T 5 nA, E_{TIP} –40 mV vs. E_{SAMPLE}. Potentials vs. PtQRef: (a) 700 mV, (b) 900 mV, (c) 200 mV, (d) 900 mV.

STM images pointed out that anions penetrate into HOPG planes easily since no discontinuities were checked on the upper region of the step (Figure 4-17b). On the contrary, when anions are de-intercalated some domains are still present on the top of the surface (Figure 4-17c), indicating that anions cannot completely go away from the step. Probably these domains were filled during the first cycle by anions, which couldn't go out anymore.

Unluckily, STM images are not good enough to quantify the intercalation process. The noise is too high to see any change in the height of the step. A possible reason is the too high acid concentration. This could affect the insulating Wax layer, which covers the STM tip. Indeed, the Faradaic current, as measured when the tip is in the electrolyte far from the tunneling regime, was observed to increase from pA to nA within some hours. As a consequence, the tip-sample current (tunneling current plus Faradaic current) was more subjected to fluctuations due to the Faradaic component.

To overcome this problem, the same investigation was repeated by in situ AFM.

4.2.2.4 In situ AFM of perchlorate intercalation: stage IV

The process of stage IV formation and dissolution was investigated on HOPG in 2 M $HClO_4$. Dimensional changes of the HOPG steps were studied over a range of step heights between 6.7 Å, corresponding to a bilayer of HOPG planes, and a micrometer, corresponding to thousands of HOPG planes. A bilayer step on a HOPG crystal was imaged under potential control, before and after formation of stage IV.

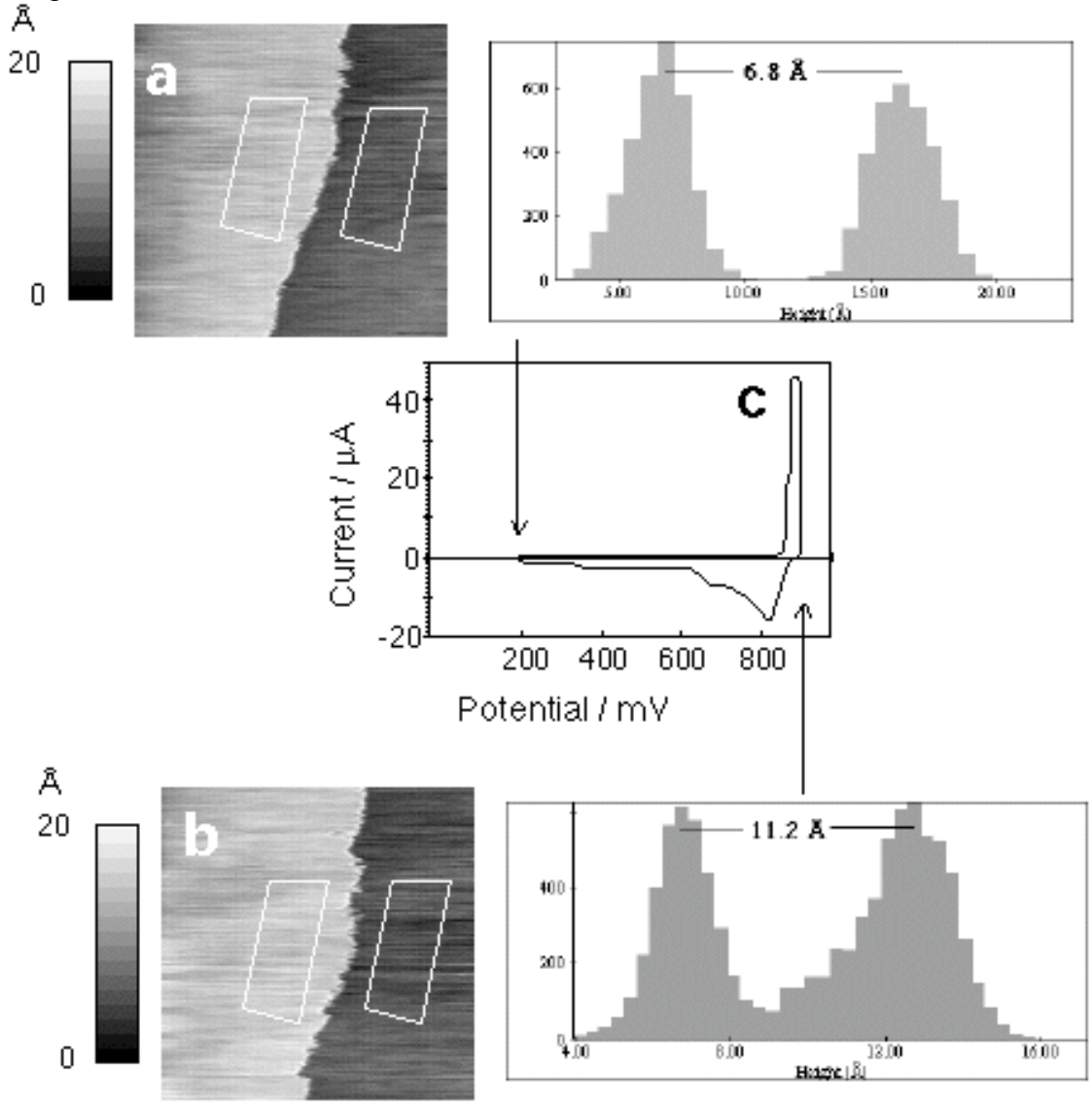

Figure 4-18: AFM images of a given HOPG bilayer in 2 M $HClO_4$ at different potentials vs. PtQRef. (a) HOPG before intercalation (+200 mV). (b) The sample was imaged after waiting for 4 min to intercalate the anions (+920 mV). (c) Corresponding cyclic voltammogram acquired at a scan rate of 25 mV/s. For each AFM image the acquisition time was about 4 min. The height distributions pertaining to the regions marked are shown on the right.

Before intercalation (+200 mV), the height of the step was 6.8 Å, as shown in Figure 4-18. After formation of stage IV (+900 mV), the height of the step was increased to 11.3 Å (Figure 4-18b). Since the distance between carbon layers upon incorporation of perchlorate ion is assumed to be 7.95 Å (see paragraph 4.2.1), the step was expected to expand up to 11.3 Å (one filled gap plus one unfilled gap). Therefore, this predicted increase in step height is exactly what we measured. Then, the potential was returned to the original value and maintained for 10 min. As a result, the height of the bilayer decreased to 6.7 Å (image not shown), which is very close to the initial value.

The experiment was repeated for a step of six layers. Figure 4-19 shows a sequence of images obtained by AFM for a multi step region on a HOPG electrode during the formation and dissolution of a stage IV GIC in 2 M $HClO_4$.

At 200 mV (Figure 4-19a), the height of the double step was 20.7 Å, which is closed to the expected height for six HOPG layers (20.1 Å). Then the intercalation of perchlorate ions was induced by potentiostating the sample to +920 mV for 4 minutes, at which time the anodic current had dropped to zero. As a result, the height of this double step increased to 28 Å (Figure 4-19b). Finally the potential was lowered to +200 mV and held at this value for 10 minutes. As a result, the height of the double step decreased to 20.5 Å (Figure 4-19c), which is very close to the initial value.

This result is in good agreement with stage IV GIC formation in HOPG. During the formation of this stage, every fourth graphite layer is available for intercalation of the ClO_4^- anions, and is filled when the corresponding critical potential is reached. As a consequence, the interlayer spacing is expected to increase only at these planes, thus causing an expansion of the original HOPG structure of about 34%.

Since the step was composed of six layers, in principle we have the same probability to fill one gap or two gaps in the HOPG layer sequence. The corresponding expected expansion is 24.7 Å (one gap filled) and 29.3 Å (two gap filled). Our experimental estimation was 28 Å; therefore we think that two of the six available gaps were filled with anions.

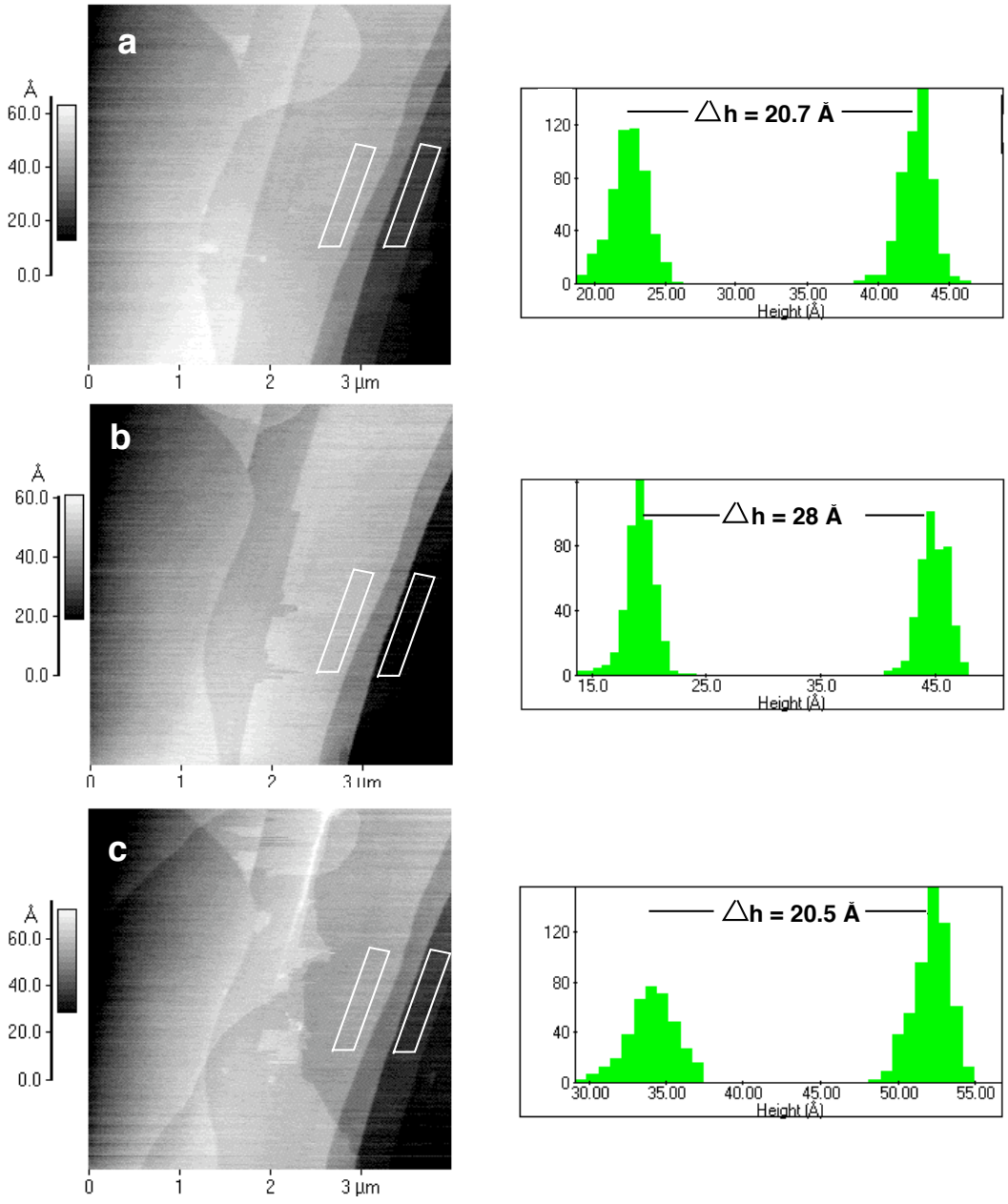

Figure 4-19: AFM images of the same HOPG step in 2 M $HClO_4$, at different potentials: (a) 200 mV, HOPG before intercalation; (b) 920 mV, the sample was imaged after waiting for 4 min to intercalate the anions; (c) 200 mV, the sample was imaged after waiting for 10 min to deintercalate the anions. For each AFM images the acquisition time was 4 min and 16 s. The height distributions related to the marked regions are shown on the right.

Similar increases in step height were obtained under the same conditions with three different HOPG samples. In Table 4-6, the increase in step height at HOPG upon intercalation is compared with the theoretical expected expansion of the HOPG interlayer spacing during the stage IV formation.

Because the anions can intercalate in different way when forming stage IV, we have calculated the minimum and the maximum value of expected expansion. For the

sample 3, we calculated just one value, because every layer sequence which is a multiple of four is expected to expand exactly 34% of the initial value, independently in which position of the sequence the gaps are filled.

Data source	before intercal. (Å)	after intercal. (Å)	after deintercal. (Å)	expected expansion (Å)
Sample 1	20.7 (200 mV)	28 (920 mV)	20.5 (200 mV)	24.7 (one gap filled)
6 layers				29.3 (two gaps filled)
Sample 2	29.3 (200 mV)	37.8 (920 mV)	33.8 (400 mV)	39.35 (two gaps filled)
9 layers				43.95 (three gaps filled)
Sample 3	39.9 (200 mV)	55.3 (920 mV)	40.7 (100 mV)	54 (three gaps filled)
12 layers				

Table 4-6: Summary of height measurements by AFM and comparison with values for stage IV formation expected from theoretical considerations (see the text for more details).

To study the influence of the number of graphene layers on stage IV formation, the thickness measurement was repeated at steps with different height, i.e. different number of carbon layers. According to the dimensions cited above for the perchlorate ion, we always expected an increase in height of about 34 % for every sequence of four - or multiple of four - graphene layers (stage IV). However, this expectation was only confirmed for steps smaller than 50 Å. As shown in the diagram plotted in Figure 4-20, the percentage change of the interlayer distance decreases with increasing number of graphene layers involved in the intercalation process.

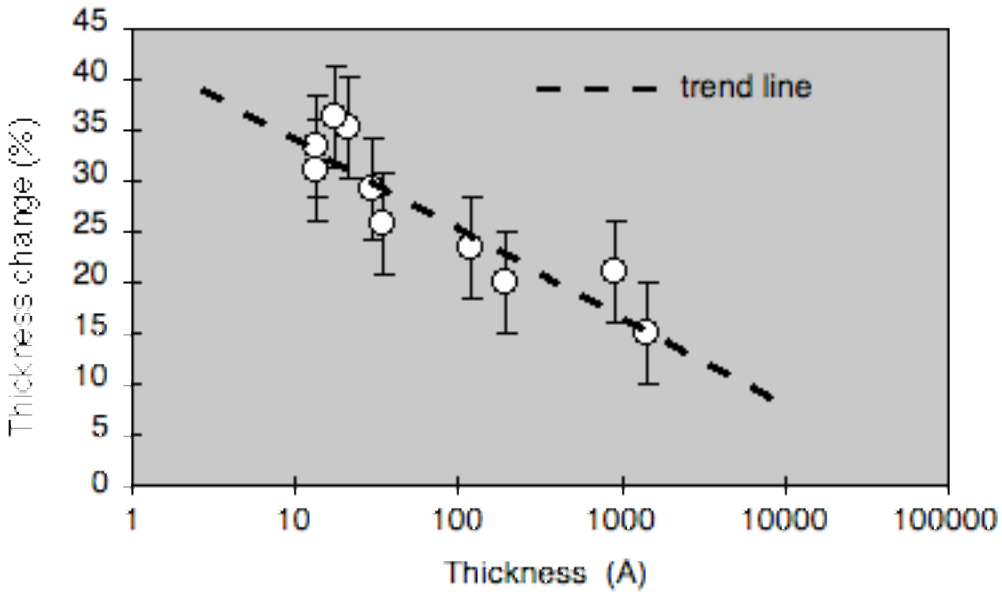

Figure 4-20: Increase in interlayer distance between graphene layers (percentage value) after formation of stage IV in 2M $HClO_4$, as a function of the thickness of the step. The potential was scan from the open circuit value to 920 mV (scan rate 25 mV/s) and held for 4 min.

This result is not completely surprising. As already discussed by Winter and coworkers [85] when studying graphite as a negative electrode for Lithium-Ion Cells, the intercalation of species into graphite generally requires considerable energy, since the gaps between the graphene layers held together by van der Waals forces must be expanded. The expansion energy depends on the mechanical flexibility of graphene layers deformed by the intercalation process. The energy increases with the number of adjacent graphene layers present on both sides of a particular gap [86]. Therefore, intercalation generally begins close to the surface, in the gap adjacent to the top basal planes. Then the intercalation progresses toward internal layer gaps.

A second additional explanation for this result resides in the fact that the probability of defects and vacancies increases with the number of graphene layer, i.e. with the thickness of the step. The presence of these defects can prevent the perchlorate ions from intercalating, since the adjacent layers are pinned together and difficult to move with respect to one another. As a consequence, the usable capacity for insertion is reduced, which was actually shown in resent studies of the properties of synthetic and natural graphite [87].

The movement of graphene layers, for instance from AB- to AA-stacking, can also influence the interlayer distance. However, this is mainly important for stage I compounds as suggested by Moret [88] and it should be less effective for stage IV compounds which are investigated here.

Our AFM measurements of relative expansion are in apparent discrepancy with previous dilatometry measurements of crystals in highly concentrated sulfuric acid [89], which had shown a relative thickness variation of 34% during stage IV formation for 0.01 mm thick HOPG. This may be due to a different quality of the HOPG samples. In fact, the importance of a highly graphitized structure for the effective formation of GIC [90] is well known.

Figure 4-19 shows another important results. The time dependence of the two processes (intercalation and deintercalation) appears to be different. In fact, Figure 4-19b, which was acquired after 4 minutes, is already showing a stable condition: no more current is flowing at the HOPG electrode. The next AFM picture acquired at the same potential after other 4 minutes (image not shown) looks very much the same as Figure 4-19b. On the contrary, when the potential was moved back to 200 mV, a cathodic current flowed for a considerably longer time and only after 10 minutes a stable situation was reached.

By comparing Figure 4-19b and c, it is evident that in addition the local kinetics of the two processes is different. In one direction (intercalation) the process is relatively isotropic (Figure 4-19b), i.e. changes in height appear to be similar at different locations long the step. The reverse process (deintercalation) is much more complicated as is evident from the existence of different kinetic regions for the diffusion of ClO_4^- anions in the HOPG structure. In the upper part of Figure 4-19c, the step is already completely went down, while in the lower part of the same image the step is still a little bit higher than originally, therefore here the deintercalation process is not yet finished.

It is not yet clear whether the presence of different kinetic regions within a few micrometers along a step is general or not. This aspect is still under investigation.

In an effort to study the reproducibility of the intercalation process, we imaged a step on a HOPG crystal with the AFM working in the xzt mode. In this case the AFM tip was forced to cross a step of 146 nm, corresponding to 438 HOPG layers, at the same fixed line position while the electrode potential was scanned between 550 mV and 950 mV (see Experimental session for more details). The resulting image is shown in Figure 4-21.

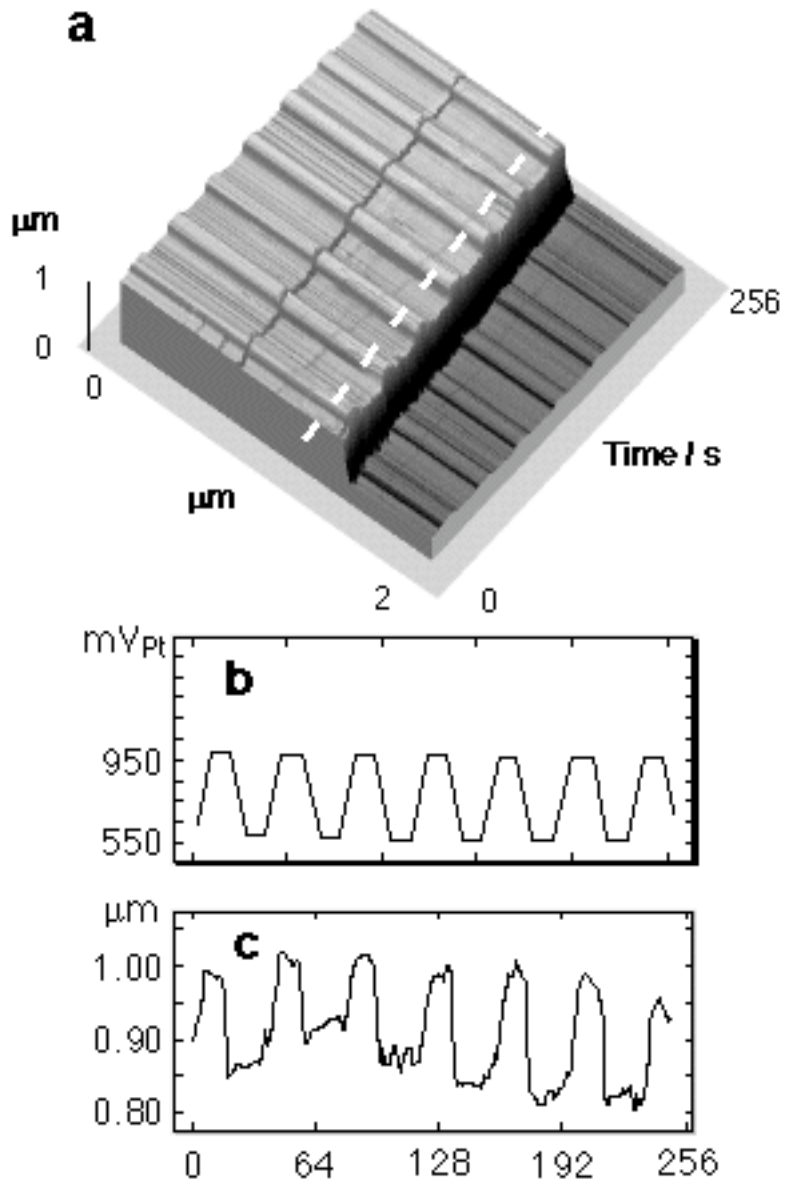

Figure 4-21: AFM image of a HOPG step region in 2 M $HClO_4$ recorded with the probe scanning a line while cycling the potential of the sample between +550 mV and +950 mV. (a) 3-dimensional view. (b) Potential transients. (c) Height profile corresponding to the dashed line in the 3-dimensional view.

The thickness variation is clearly reflected in the alternating peaks and valleys, which correlate with the intercalation and deintercalation of perchlorate ions in HOPG, respectively.

The thickness change observed at the bottom of the step in Figure 4-21 is a consequence of the intercalation of perchlorate ions into a second step outside the field of view.

The correlation between thickness variation and HOPG potential is more clearly visible when we examine the height profile plotted across a line parallel to the HOPG step (Figure 4-21c) together with the potential transients (Figure 4-21b). The contribution of the above-mentioned second step was subtracted in order not to overestimate the change in thickness. The change is about 26 nm, corresponding to a percentage variation of 18.7 %. This result proves that the interlayer distance of the graphene layers varies reversibly between the original value typical for a sequence of unfilled gaps and the "intercalated" value for a sequence of gaps filled with perchlorate ions. In this case, since the number of graphene layers involved in the process is high, the expansion measured by AFM (18.7 %) is lower than that theoretically expected for stage IV (34%). Also this results can be explained with the same arguments used for Figure 4-20.

4.2.2.5 Stages IV, III, and II

The procedure adopted to investigate the dimensional changes and the kinetics of stage IV formation was here applied to study the lower stages (stage III and stage II). To do this, a step of four graphene layers on a HOPG crystal was imaged at different potentials.

First, the step was imaged at 0 V_{Pt}. The corresponding AFM picture and height distribution is shown in Figure 4-22a. Then the same step was imaged at 1.04 V_{Pt} (Figure 4-22b), 1.07 V_{Pt} (Figure 4-22c) and 1.1 V_{Pt} (Figure 4-22d), corresponding to the potentials for the formation of stages IV, III and II, respectively.

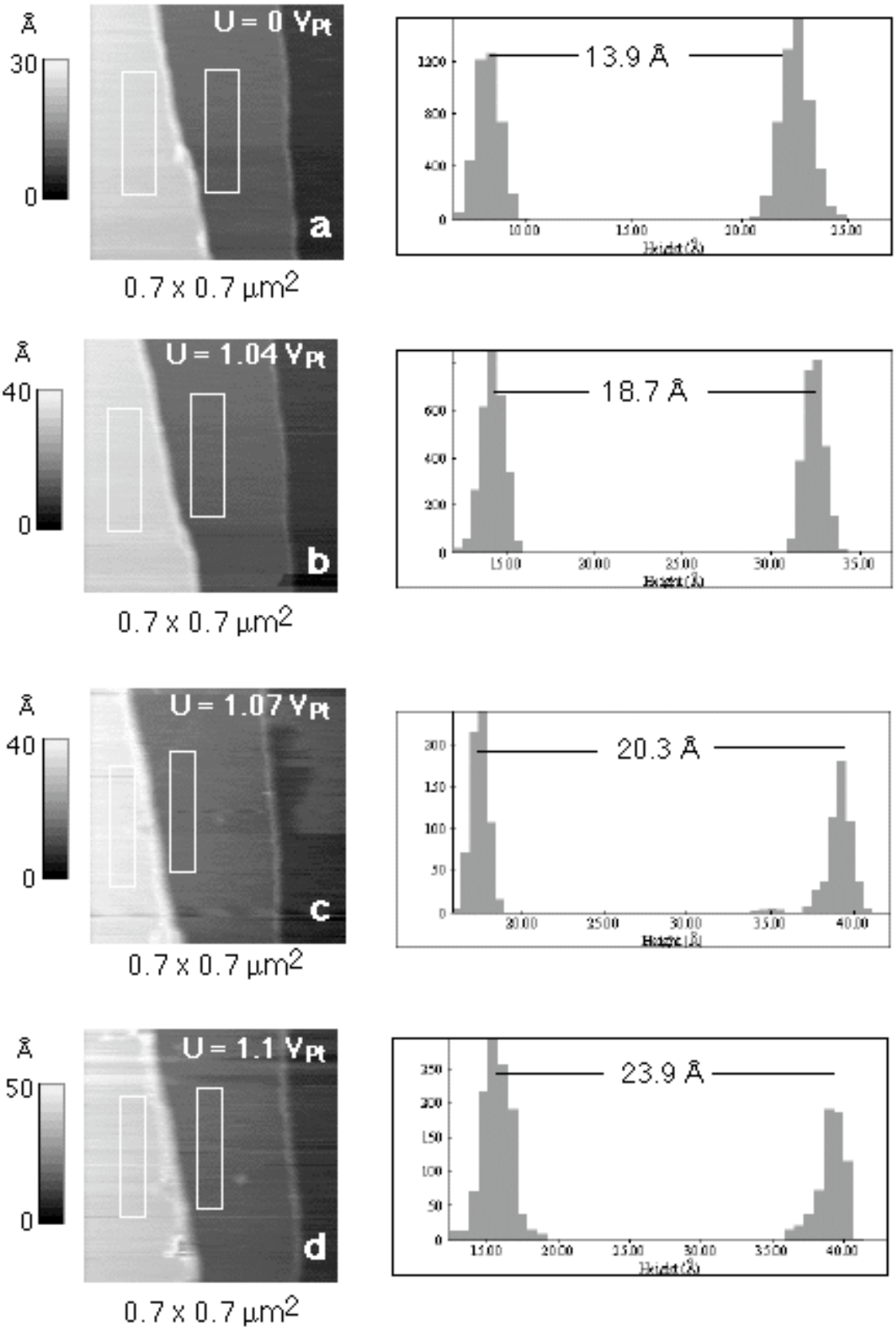

Figure 4-22: Sequence of AFM images of a given HOPG four-layer step in 2 M $HClO_4$ at different potentials: (a) before intercalation, (b) stage IV, (c) stage III, (d) stage II.

After the formation of each stage, the potential was returned to 0 V_{Pt} in order to dissolve the stage, and then the step was imaged again to test the reversibility of the process. The histogram plotted in Figure 4-23 summarizes the resulting percentage changes for the interlayer spacing and the expected theoretical values.

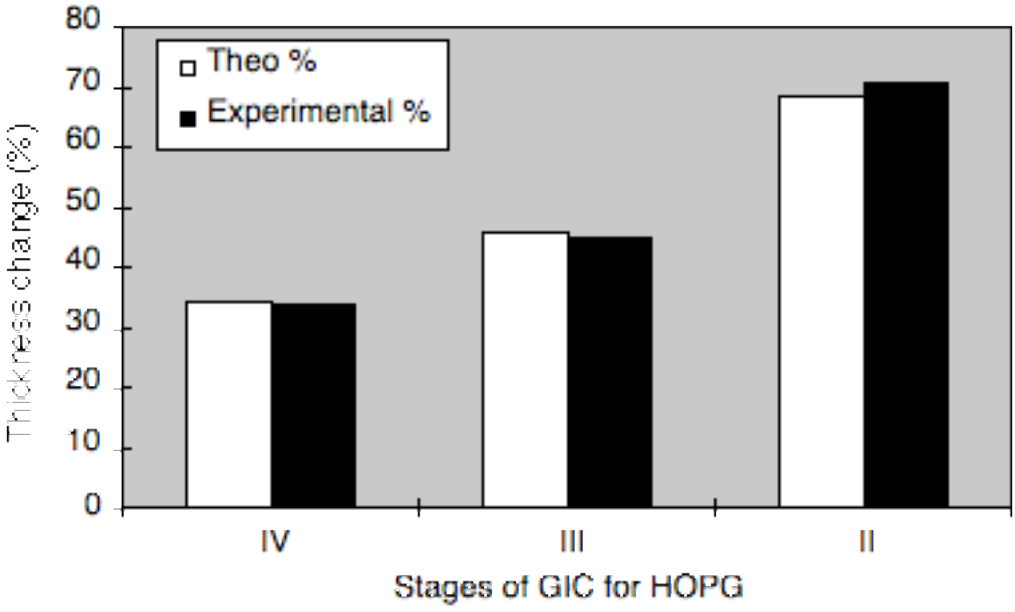

Figure 4-23: Histogram showing the percentage interlayer distance change for different stages: comparison of experimental and theoretical values.

Unfortunately it was not possible to study the formation of stage I, because the potential required was so high that side reactions took place, and as a result the surface of the HOPG crystal was irreversibly damaged. Etching of the steps and occasionally blister formation were observed (see below).

4.2.2.6 Blister formation

Blister formation was occasionally noticed on basal planes after the intercalation of perchlorate ions. We observed blisters becoming larger or smaller depending on the applied potential.

The three AFM images of Figure 4-24 show the dynamics of formation and partial disappearance of a group of blisters as a result of several cycles of potential between 0 V_{Pt} and 0.95 V_{Pt}. In the first image (Figure 4-24a), two groups of blisters are clearly visible at 0 V_{Pt}. When the potential is moved to +0.95 V_{Pt} (Figure 4-24b), the smaller group of blisters is no longer present and part of the larger blister has disappeared. When the potential was moved back to 0 V_{Pt} (Figure 4-24c), the blister group reappeared and some blisters merged.

This blister formation is similar to that observed by Murray and coworkers [91] on a HOPG surface in less concentrated electrolytes and probably is associated with the same mechanism of formation. Murray et al. proposed a model (see paragraph 4.2.1) in which blister formation reflects the intercalation of electrolyte and water into HOPG followed by subsurface gas evolution (electrolysis).

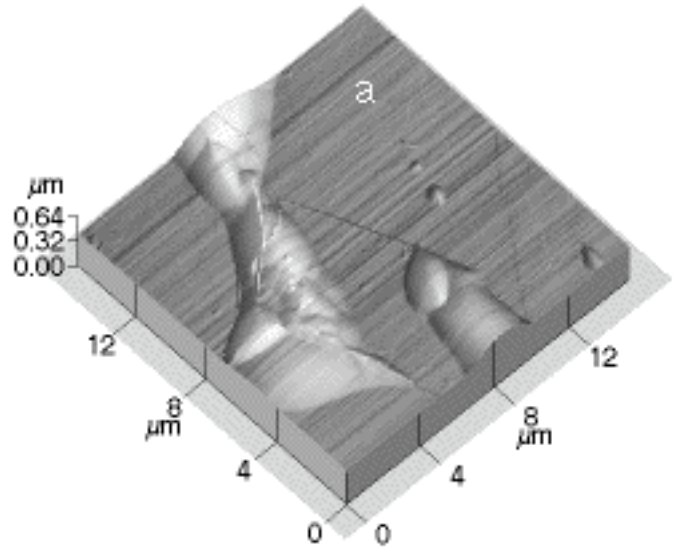
a
µm
0.64
0.32
0.00
12
8
µm
4
0
0
4
8
µm
12

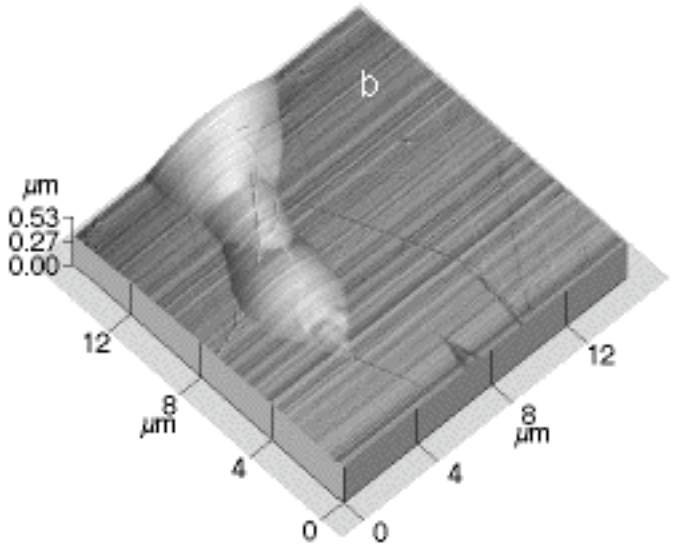
b
µm
0.53
0.27
0.00
12
8
µm
4
0
0
4
8
µm
12

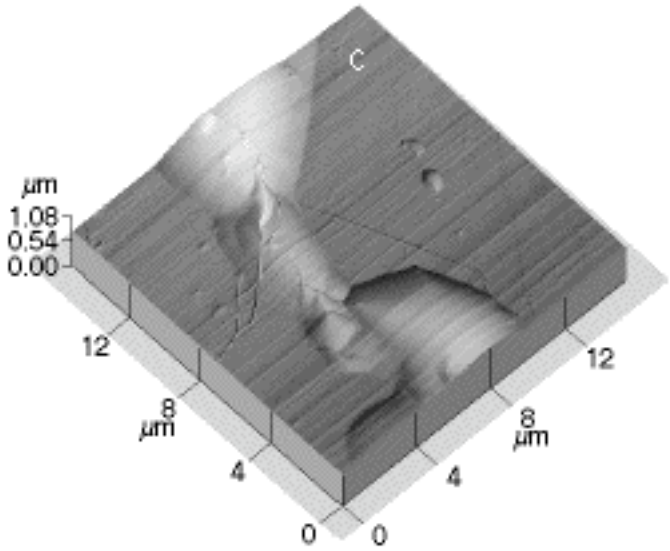
c
µm
1.08
0.54
0.00
12
8
µm
4
0
0
4
8
µm
12

Figure 4-24: Blister formation under potential control on a HOPG crystal in 2 M $HClO_4$. (a) 0 V; (b) 0.95 V; (c) 0 V. Potentials vs. PtQRef.

The main force driving the vertical and horizontal expansion of the blisters is mechanical stress caused by subsurface gas evolution. Initially, the gas evolves at anodic potential. The subsequent apparent growing of the blisters when the potentials is reversed to a cathodic value (see Figure 4-24b and c) is explained b y the expulsion of intercalated ions and corresponding change in thickness of the layered structure. At every scan cycle more gas is evolved at the anodic potential, therefore the blister is growing again. Our AFM results acquired under at controlled anodic and cathodic potentials seem to support the model discussed in paragraph 4.2.1.

4.2.2.7 Friction measurements

The understanding of tribological phenomena was one of the most extensively treated topics of the last few years [92]. Nevertheless, more has to be done, especially at microscopic scale. Lateral Force Microscopy (LFM) is able to measure normal and lateral forces at nanometer scale in various environmental conditions, included an electrolytic cell [93]. The goal of this study is to show a possible correlation between change in friction properties of HOPG and intercalation processes.

According to the LFM method described in paragraph 3.3.3, a step of four graphene layers was imaged under potential control in 2M $HClO_4$ (Figure 4-25). At -200 mV_{Pt}, no friction effect was probed at the step, as it is clear by comparing the forward and backward LFM images. When the sample was held at +700 mV_{Pt}, a strong friction signal appeared at the step, while almost nothing changed on the basal plane surface.

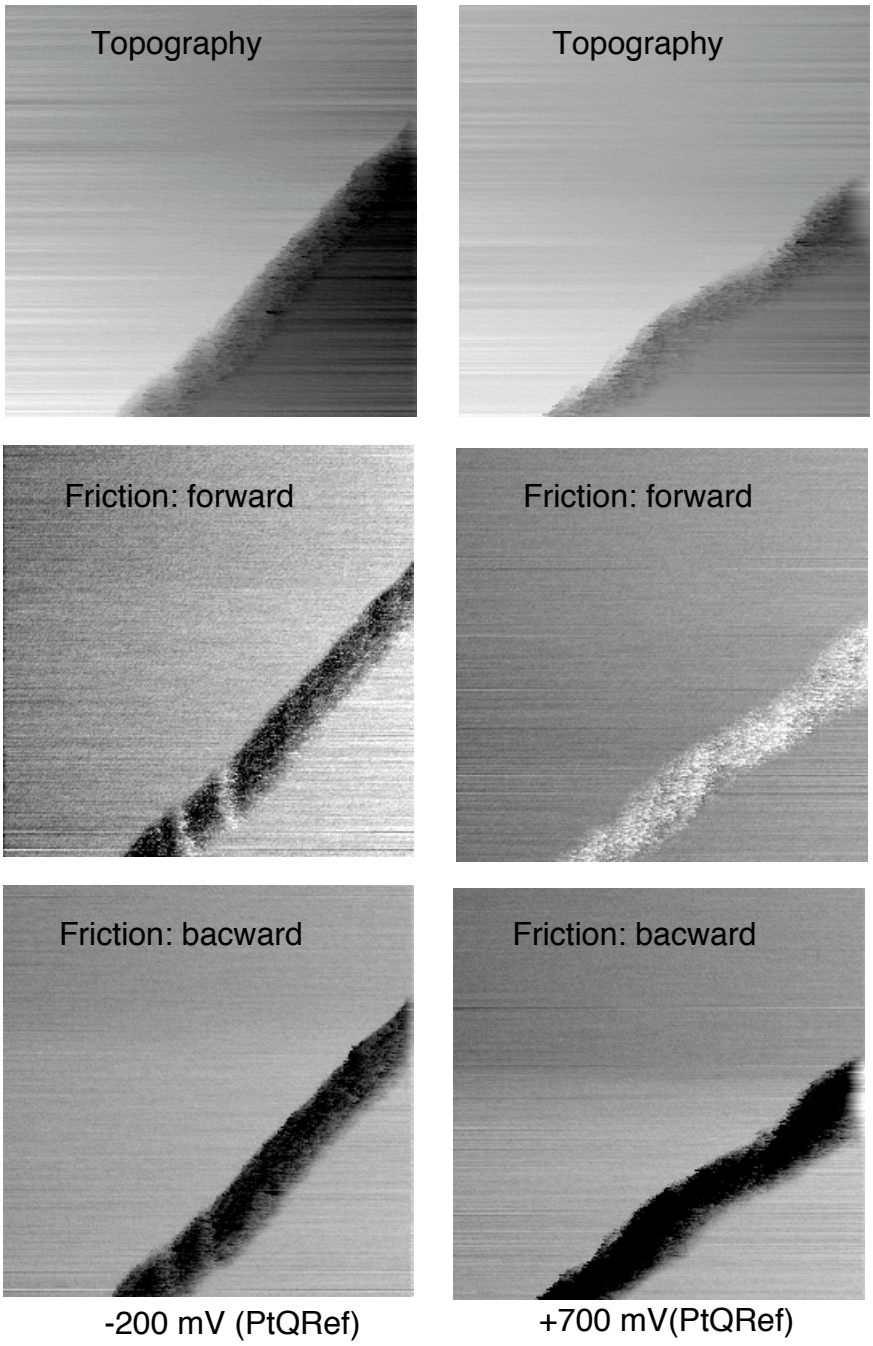

Figure 4-25: HOPG in 2 M $HClO_4$ at different potentials imaged by AFM/LFM. Size 1 x 1 μm^2. Reference electrode PtQRef.

The height of the step was not changing and the corresponding cyclic voltammogram (Figure 4-26) was not showing any intercalation process. Therefore the change in friction at the step can be assumed to be not a consequence of stage formation. However, the cyclic voltammogram shows an increase in the anodic current for potentials higher than 650 mV_{Pt}. This higher current might reflect a

stronger adsorption of perchlorate ions near the step that could affect the friction properties of steps in an HOPG crystal.

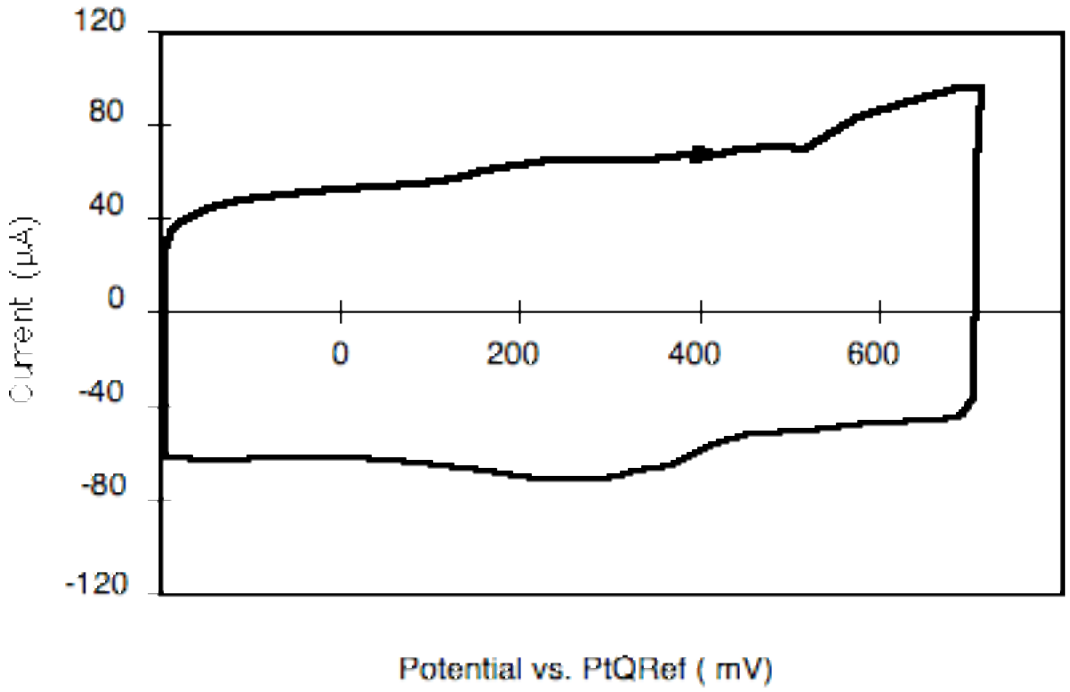

Figure 4-26: Cyclic voltammogram of an HOPG crystal in 2 M $HClO_4$; scan rate 100 mV/s.

The reproducibility of the friction effect at the step is well shown in Figure 4-27. By using the LFM in zxt-mode, the sample potential was cycled between -200 mV and +700 mV, while two steps (center and right) at a HOPG crystal were imaged in topography and friction.

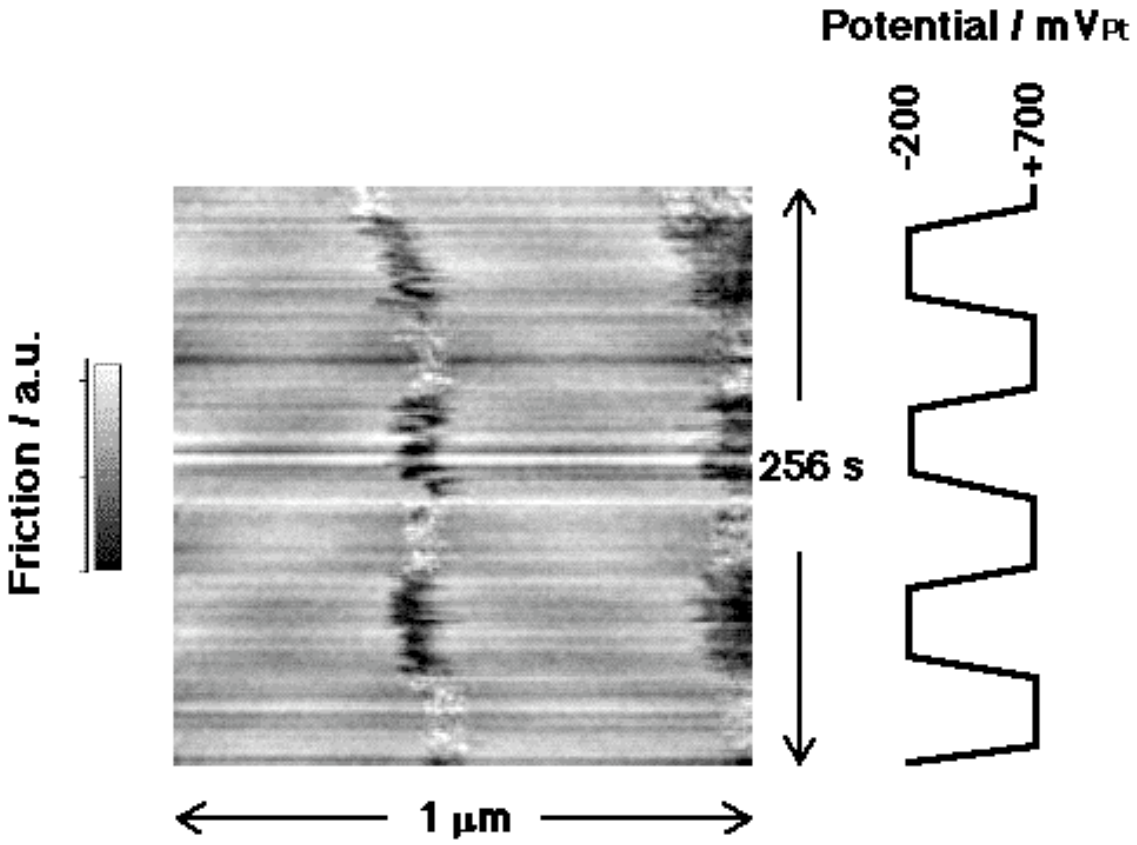

Figure 4-27: Friction vs. time image (left) and corresponding potential transients (right). Reference electrode PtQRef. Potential scan rate 100 mV/s. Imaging speed 1 Hz.

The changes in friction are clearly visible on the center and on the right, in correspondence with the change in potential. This phenomenon is clearly reversible.

To study possible effects of the stage formation on the friction signal, the potential was further increased till 925 mV, which is enough to form stage IV.

As shown in Figure 4-28, the formation of the stage IV changes the friction coefficient at a step, permanently. Here, LFM images were acquired at 925 mV, enabling the stage IV formation, and at 600 mV, which is negative enough to expel intercalated ions.

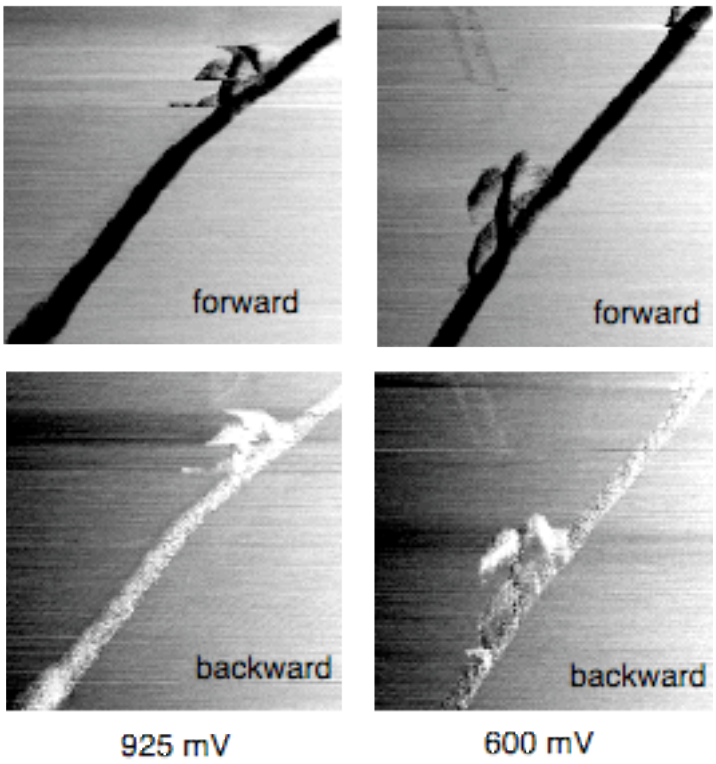

Figure 4-28: Friction signal by LFM at a step with HOPG basal planes in 2 M $HClO_4$. Potentials are expressed vs. PtQRef. Scan size 1 x 1 μm^2. Image speed 1 Hz.

We also tried to correlate the friction changes at the surface of an HOPG crystal with the formation and dissolution of Graphite-intercalation-compounds. The friction coefficient was measured as a function of the potential applied to the HOPG electrode from –0.2 V to 1.2 V vs. PtQRef. The corresponding plot is shown in Figure 4-29.

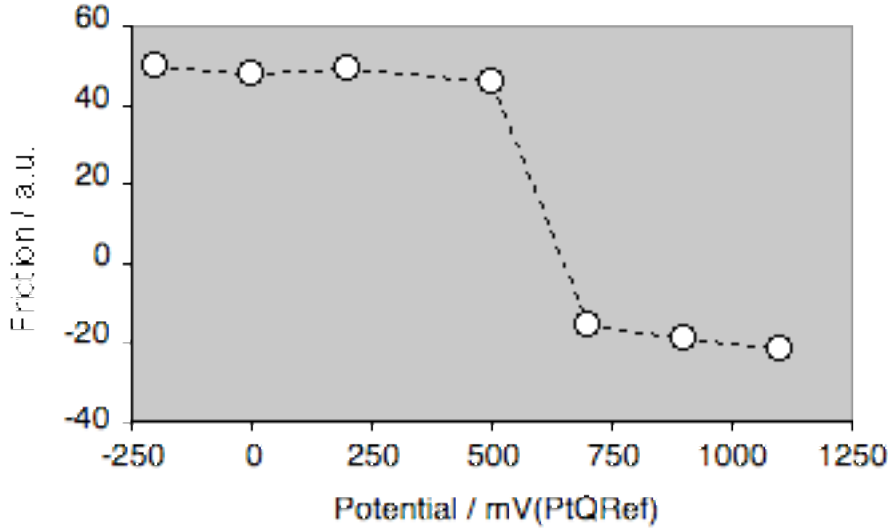

Figure 4-29: Dependence of the friction coefficient upon the potential applied. The friction was measured by in situ LFM on a 10 Å high step of HOPG in 2 M $HClO_4$. The friction coefficient is the average between the forward and the backward signal.

The change of the friction coefficient for an HOPG crystal was for the first time discovered by Marti and coworkers [94,95] in different electrolytes. Nevertheless, the origin of the friction behavior of graphite steps and a possible correlation with the oxidation / reduction of surface functional groups was not clarified. In agreement with Marti's studies, we observed a reversible change in the friction coefficient at HOPG steps in an electrolytic environment, and no evidence of similar phenomena on the basal plane surface. Furthermore, our results indicated that the friction coefficient at steps changes permanently, as soon as a stage IV is formed. Whether this behavior is due to chemical reactions at the graphite or to adsorbates at the steps could not be decided by only considering the LFM results. As illustrated in the next paragraph, an ex situ XPS investigation was performed to gain full understanding of the friction effects at HOPG steps.

4.2.2.8 XPS measurements

Ex-situ XPS studies can provide information about the electronic and chemical states of the electrode exposed to an electrolyte at a defined potential. Kolb at al. [96] and Kötz and coworkers [97] demonstrated the preservation of the double layer, built by counter ions, during the transfer to the UHV system.

XPS investigations were performed on HOPG charged in 2 M $HClO_4$. HOPG basal plane electrodes were charged at potentials between –0.2 V_{Pt} and 1.2 V_{Pt} and removed from the electrolyte under potential control. With XPS technique the adsorbed chlorine can be well distinguished from the intercalated one. In the potential region 0.2 - 1.2 V_{Pt} , which is more positive than the zero charge potential, the chlorine content increases with the increased amount of anions in the double layer. At potential higher than 0.95 V_{Pt} , i.e. where the stage IV starts to form, the increase of the chlorine species is even more pronounced. Chlorine can be due to either adsorbed or intercalated perchlorate ions. By XPS the adsorbed perchlorate can well be distinguished from the intercalated one (see Figure 4-30). In fact, the Cl 2p level of the intercalated species is shifted with respect to the adsorbed perchlorate by ~ 1.7 eV.

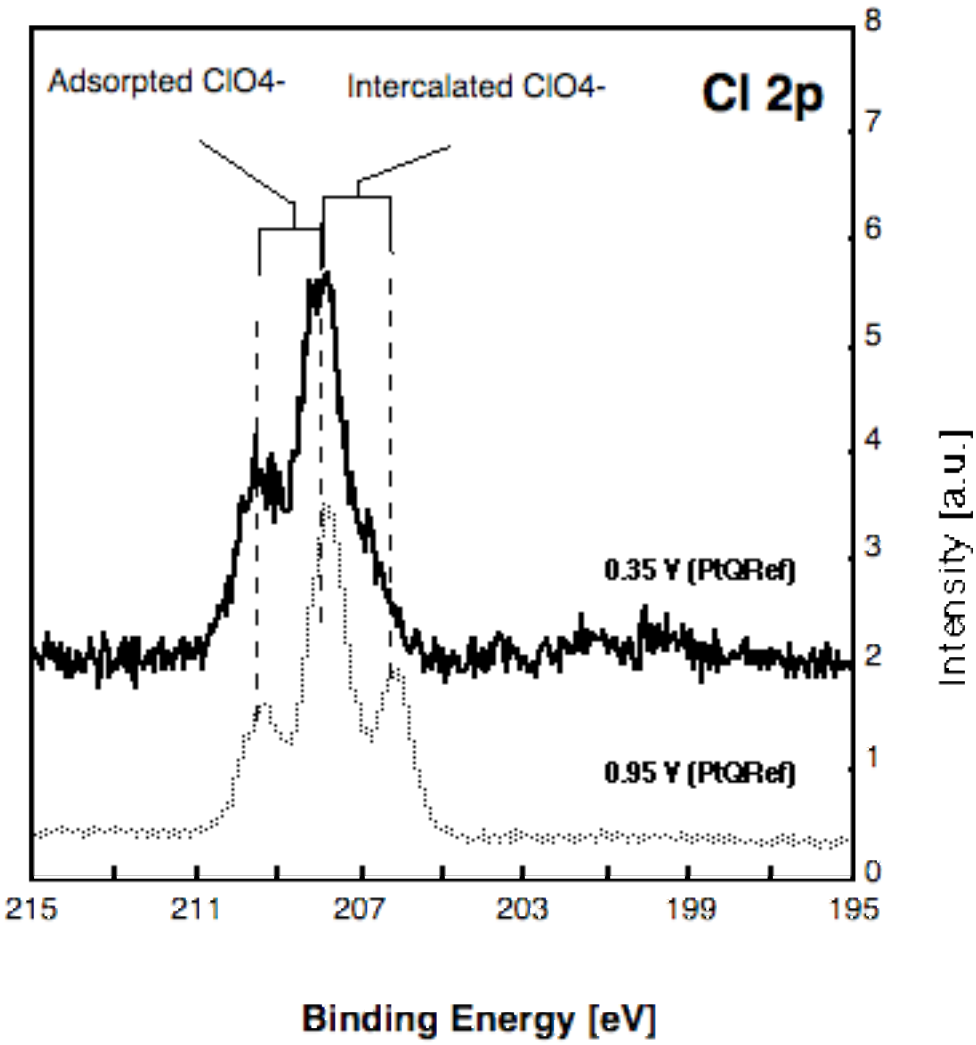

Figure 4-30: High resolution XPS spectra of the Cl 2p region for 0.35 V (dark line) and 0.95 V (gray line).

A smaller binding energy shift of ~ 0.7 eV could be also observed in the C 1s spectrum of intercalated samples (see Figure 4-31). Here, a graphitic carbon peak appeared at 284.3 eV with a long tail toward higher binding energy, which was attributed to interaction with the conduction band electrons [98]. The perchlorate however should not change the valence state and the C 1s peak should shift in the opposite direction in order to maintain the charge neutrality.

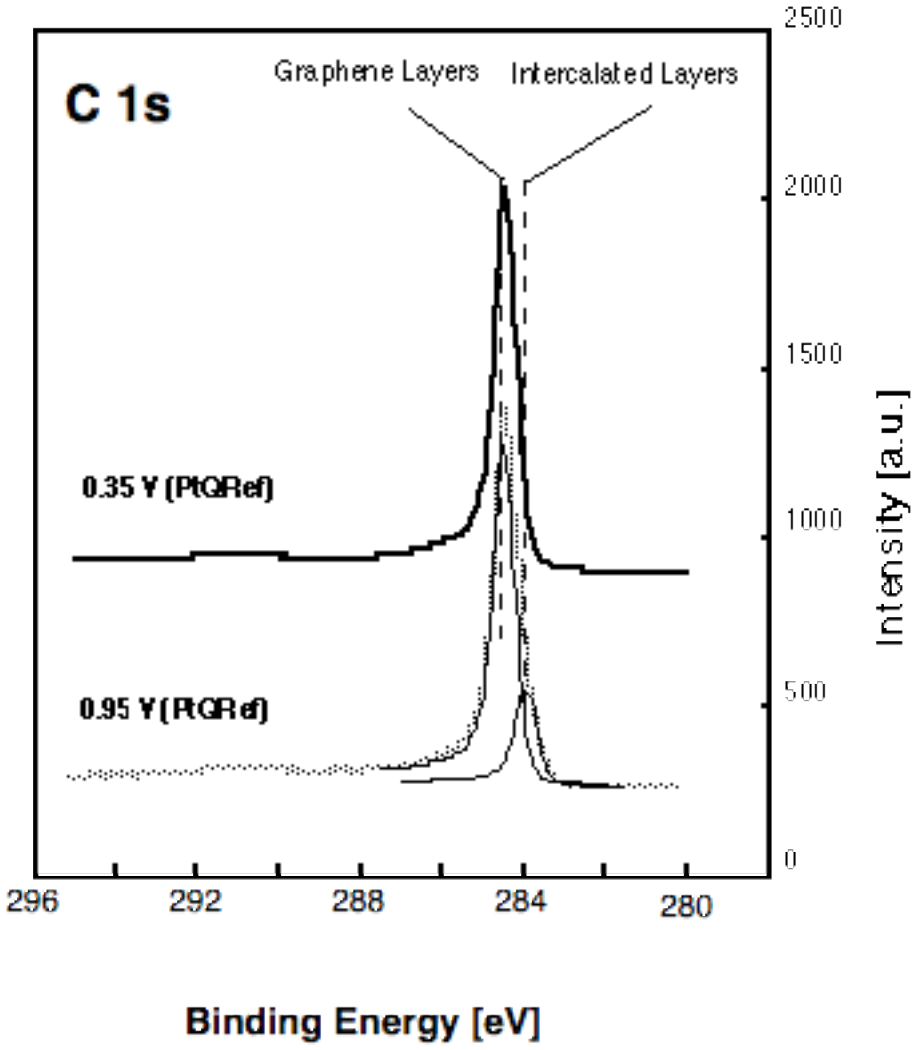

Figure 4-31: High resolution XPS spectra of the C 1s region for 0.35 V (dark line) and 0.95 V (gray line), corresponding to potential where adsorption or intercalation/adsorption occurred.

The observed shifts can be explained by a shift of the Fermi edge for the intercalated layers [98]. The resulting energy scheme is illustrated in Figure 4-32.

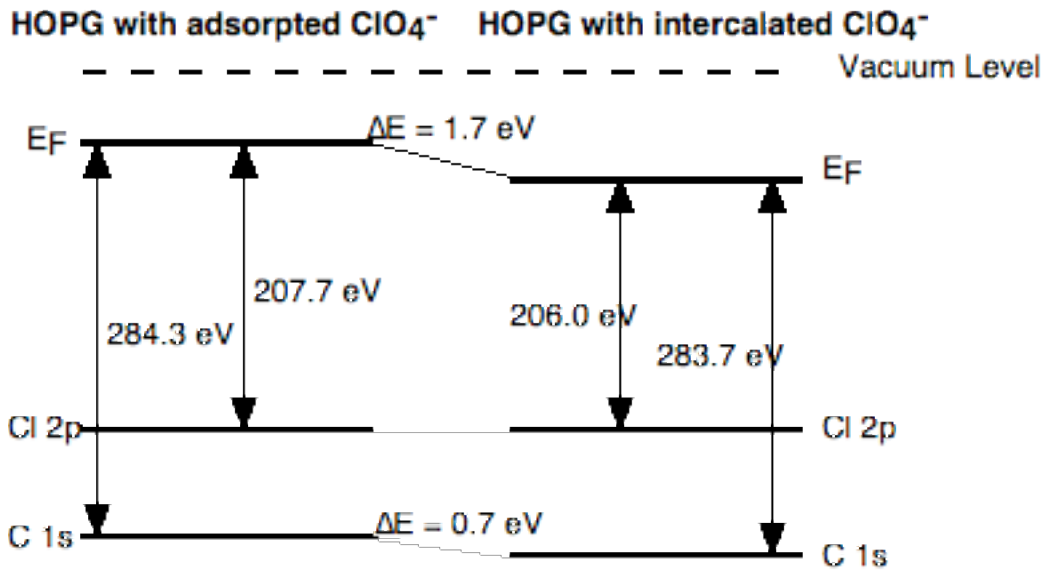

Figure 4-32: Energy scheme of HOPG with adsorbed and intercalated species of perchlorate ions.

XPS results showed clear evidence of intercalated species for potentials higher that 0.95 V_{Pt}. Unfortunately, we had no indication that the trend of adsorption of pechorate ions changes at the potential where the friction is also observed to change. Different reasons can explain the combined LFM and XPS results. For instance, the friction change could be due to an adsorption of ions at the steps, which starts at 0.7 V_{Pt}., which is the potential where the LFM signal changes. Nevertheless, the XPS technique is not able to discriminate between ions adsorbed on the basal planes and at the steps. Therefore, the XPS results are not in contradiction with the LFM observations.

Another possibility is that the ions are since always accumulated at the steps, but for geometrical reasons the LFM tip starts to be affected by their presence only when enough ions are adsorbed at the step to perturbate the interaction forces between the tip and the sample surface.

The second possibility here mentioned seems to be more reasonable. In fact, in case of a more general adsorption of ions on the basal planes, we should expect a change in the friction signal also there, and not only at the steps.

4.2.3 HOPG in Sulfuric Acid

In the effort to study a possible dependence of the stage formation process upon the electrolyte, a second system was investigated. HOPG basal plane electrodes were investigated in 1 M H_2SO_4. As already discussed in literature [99], only at

much higher acid concentration the efficiency of stage formation is comparable with the efficiency of perchloric acid. Nevertheless, in this case we were more interested to study the effect of the side reactions like CO and CO_2 production, which are more favorite at this low acid concentration. Furthermore, an experiment at 10 M acid concentration, for instance, was at the present state out of our possibility because of the expected strong corrosion.

4.2.3.1 Electrochemistry

The typical voltammogram for HOPG in 1 M H_2SO_4 is shown in Figure 4-33.

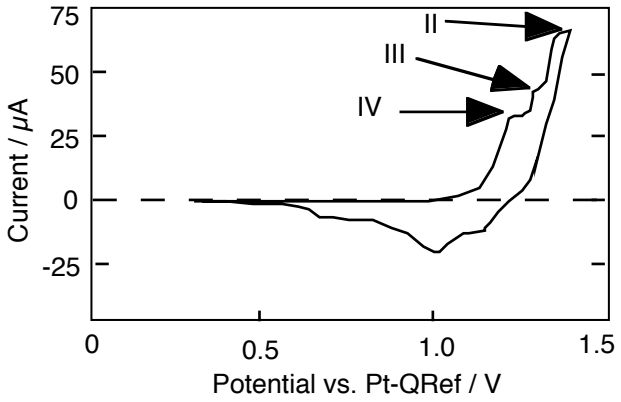

Figure 4-33: Cyclic voltammogram (2nd cycle) recorded at HOPG in 1 M H_2SO_4. Scan rate: 25 mV/s. According to the literature [21], peaks positions on the potential scale are typical for stages IV, III and II.

Again, the Equation 4-2 well describes the appearance of anodic peaks and cathodic counter peaks. However, in this case side reactions are much more important, which can be seen by comparing the oxidative (Q_A) and reductive (Q_C) charges associated with the voltammogram in Figure 4-33. In Table 4-7 charges are compared with the corresponding values determined for perchlorate ions, in order to estimate the degree of reversibility of the intercalation process.

CV	Ion	Q_A (mC/cm^2)	Q_C (mC/cm^2)	Q_C/Q_A
1a	perchlorate	7.15	5.51	0.8
1b	hydr.sulfate	43.7	13.39	0.3

Table 4-7: Anodic (Q_A) and cathodic (Q_C) charges for hydrogen sulfate are compared to the equivalent values typical for perchlorate ions. All values are normalized with respect to the HOPG area. Charges correspond in both cases to formation of stages IV, III and II.

The values of Q_A were calculated by integrating the CVs over the potential range between 0.85 V and the potential of anodic scan reversal. The values of Q_C represent the total cathodic charge above 0.3 V. While for intercalation of

perchlorate ions the charge efficiency is still relatively high even for stage II formation (Q_C/Q_A = 0.8), in the case of hydrogen sulfate ions the anodic charge is much higher than the cathodic one (Q_C/Q_A = 0.3) and, as a consequence, the efficiency of the intercalation process is reduced.

4.2.3.2 In situ electrochemical AFM of hydrogen sulfate intercalation

A freshly cleaved HOPG electrode was exposed to a 1M H_2SO_4 solution.

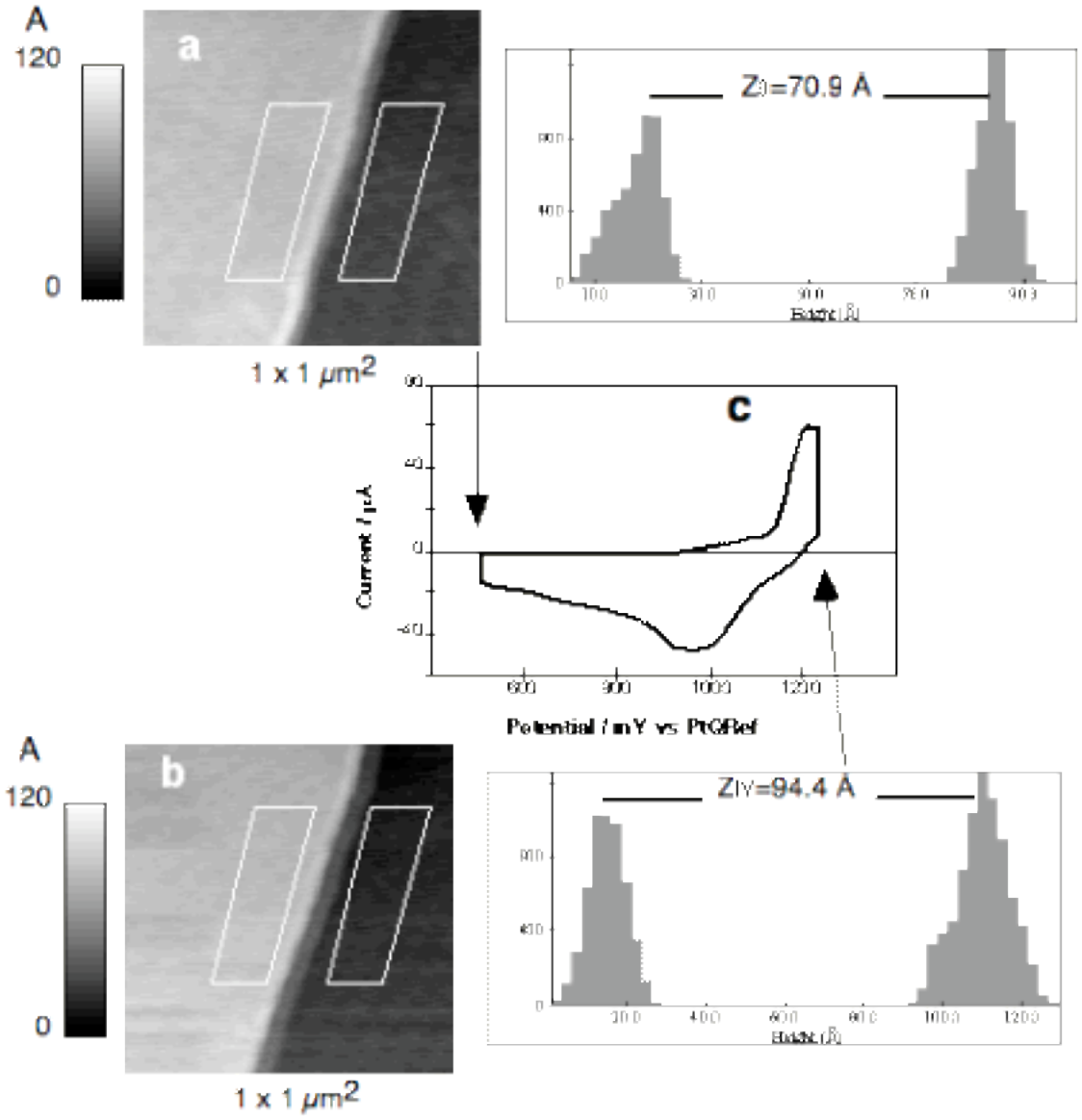

Figure 4-34: AFM images of a given HOPG multilayer in 1 M H_2SO_4, at different potentials. (a) HOPG before intercalation (+500 mV). Potentials are vs. PtQRef. (b) After waiting for 4 min to intercalate the anions (+1250 mV). (c) Corresponding cyclic voltammogram acquired at a scan rate of 25 mV/s. For each AFM image the acquisition time was about 4 min. The height distributions pertaining to the regions marked are shown on the right.

In Figure 4-34, a step of 21 layers is imaged before and after intercalation of hydrogen sulfate ions. The corresponding histograms show the increase in step height of 33.1% which is very close to the expected expansion of the interlayer spacing after formation of stage IV (see paragraph 4.2.1). However, after few (2 to 3) cycles the process cannot be reproduced anymore. For instance, Figure 4-35 shows how the surface of an HOPG crystal was damaged after two cycles in potential between 0 V and 1.25 V.

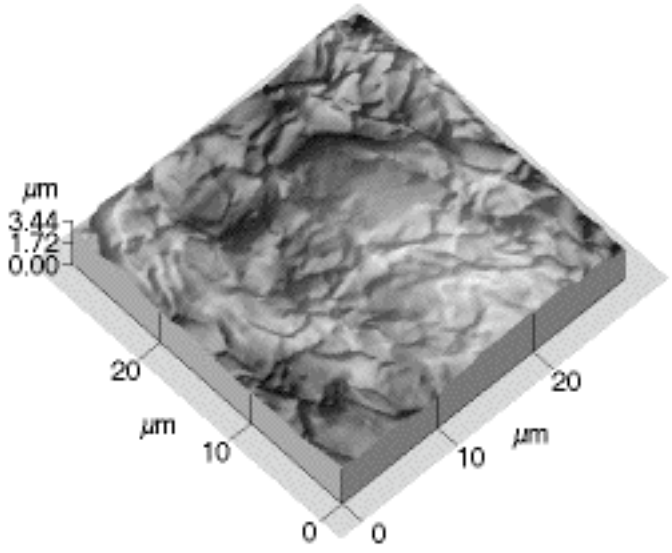

Figure 4-35: Effect of oxidation on the morphology of a fresh HOPG crystal in 1 M H_2SO_4 after two potential cycles between 0 V and 1.25 V vs. PtQRef.

Compared to the system of HOPG in perchloric acid, which was investigated earlier, HOPG in sulfuric acid is much more sensitive to irreversible modification of its surface because of the presence of side reactions (graphite oxide formation, carbon dioxide formation, water electrolysis), which are running in parallel with the intercalation (see Table 4-7 for the comparison of the charge efficiencies). This is mainly due to the fact that the potential we have to apply to induce hydrogen sulfate ion intercalation is higher than the potential required to intercalate perchlorate ions. As a result, the surface of HOPG is destroyed much more easily in sulfuric than in perchloric acid.

4.3 HOPG in non-aqueous electrolytes

After having studied the graphite intercalation compounds created in aqueous electrolytes, the investigation was extended to the formation of Lithium -graphite

compounds as anode materials for rechargeable lithium batteries. Our major effort was focused on the Solid Electrolyte Interphase (SEI) film formation process. This is motivated by the fact that proper filming is important for the protection of carbon materials, which are, otherwise, subjected to degradation.
Aim of the present set of experiments is to elucidate the mechanism of the film formation process at nanoscale level. STM and AFM/LFM, combined with Cyclic Voltammetry, were used as an in situ analytical tool during intercalation of lithium ions and co-intercalation of solvent molecules through the surface of graphite electrodes.

4.3.1 Electrochemistry

To evaluate the best experimental condition allowing intercalation and corresponding SEI film formation, cyclic voltammetry was applied to the system of powder graphite (SFG-6) in 1 M $LiPF_6$ dissolved in EC:DMC.
The SFG-6 electrode initially was discharged and charged at a scan rate of 400 μV/s in a hermetically sealed cell, as described in the experimental section. The resulting voltammogram is shown in Figure 4-36.

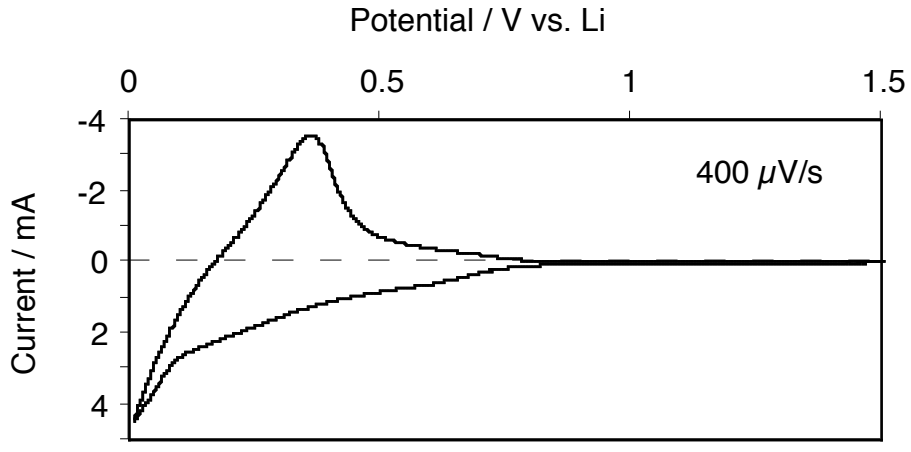

Figure 4-36: Cyclic voltammogram of SFG-6 in 1 M $LiPF_6$ (EC:DMC). Scan rate 400 μV/s. First cycle.

The cathodic current is observed to grow for potentials more negative than 0.7 V_{Li}. The current increases monotonically as indicated by the slope of the curve and was attributed by several authors [100, 101, 102, 103] to the reduction of the electrolyte, which leads to the formation of a SEI film. This reaction is normally finished within the first discharge of the graphite electrode and helps to avoid following cointercalation of solvent molecules, which would have tremendous effect on the graphite structure. At 0.2 V_{Li} the current increases faster. This is due to lithium

ions that start to intercalate through the graphene planes, which are deintercalated as soon as the potential is turned to a more positive value. The presence of an anodic counter peak at ca. 0.35 V_{Li} is a proof of the reversibility of the intercalation process. Because of the rather fast scan rate, we cannot yet resolved the formation of stages. This major characteristic of the intercalation reaction is well shown in Figure 4-37. Here, the SFG-6 electrode was scanned at a rate of 10 μV/s.

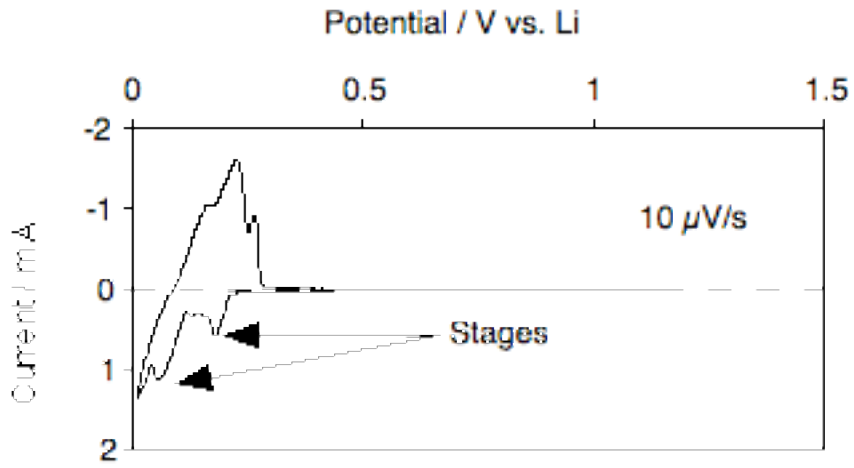

Figure 4-37: Second cyclic voltammogram for SFG-6 in 1 M $LiPF_6$ (EC:DMC) at a scan rate of 10 μV/s vs. Li/Li^+. Three stages are formed at ca. 0.2 V, 0.15 V and 0.1 V, as indicated by the three cathodic peaks and anodic counter peaks.

At least three stages are formed at ca. 0.2 V, 0.15 V and 0.1 V. Three counter peaks are also visible in the anodic sweep.

To compare the electrochemical behavior of a commercial and widely used graphite electrode, like SFG-6, and a more “ideal” electrode, the voltammetry were repeated with HOPG in the same experimental conditions as with SFG-6. The resulting first and second voltammograms are shown in Figure 4-38.

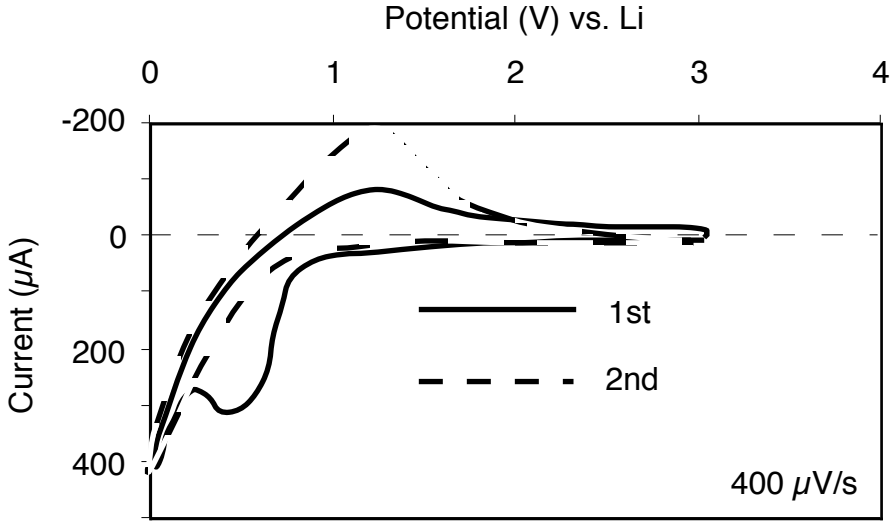

Figure 4-38: Voltammograms of basal planes of HOPG in 1 M $LiPF_6$ (EC:DMC) vs. Scan rate 400 μV/s. Potentials vs. Li/Li^+. The anodic peak centered at 0.5 V in the first cycle indicates the formation of a SEI film. The absence of the peak in the second cycle indicates that the film formation process is finished.

The cathodic peak centered at 0.5 V again indicates the formation of a SEI film. At potentials below 0.3 V, the current restarts to increase until reaching the cathodic limit.

It is immediately evident that here the current is an order of magnitude smaller and the SEI film formation is much more evident and clear than on SFG-6. This can be explained with the limited number of surface defects, mainly steps, through which the Li^+ can intercalate. Therefore the SEI film formation is more emphasized compare to the intercalation of lithium.

To know whether different stages of Li-GIC could also be discriminated, a new cycle at a scan rate of 10 μV/s was performed. The resulting voltammogram depicted in Figure 4-39 shows only a single large peak in the cathodic current, and a corresponding anodic counter peak, possibly due to the convolution of different stages.

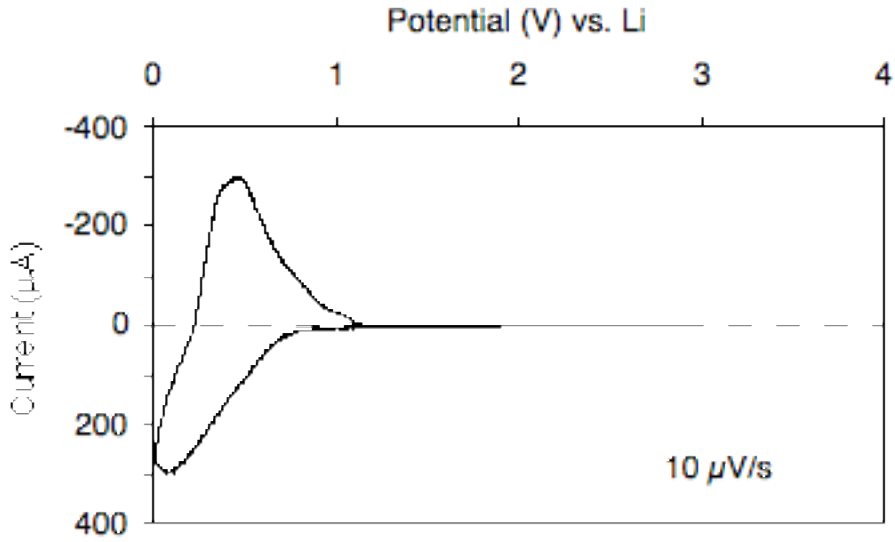

Figure 4-39: Basal planes of HOPG in 1 M $LiPF_6$ (EC:DMC) at a scan rate of 10 μV/s. Potentials vs. Li/Li^+. The presence of a single cathodic peak centered at 0.15 V indicates that the formation of different stages is not resolved.

These experiments indicate how favorite is the SEI film formation on HOPG compare to SFG-6 and, on the opposite, how more difficult is the intercalation of Li^+ through HOPG. The second important information is that only at very low scan rate (less than 10 μV/s) the stage formation of Li-GIC can be investigated.

One of the major problems, when $LiPF_6$ is used in an organic solvent is that it is very sensitive to the presence of water in the electrolyte, which cause the formation of HF. This compound is non tolerable to perform an in situ SPM experiment because it can corrode the glass window of the cell to be used. For this reason we extended the cyclic voltammetry characterization to HOPG in lithium perchlorate. Since results are very close to the previous one in lithium hexafluorate, it was decided to start the in situ experiments with lithium perchlorate in EC:DMC solvent.

4.3.2 In situ STM of SEI film formation

An in situ experiment was performed on HOPG in 1 M $LiClO_4$ dissolved in a mixture of EC and DMC. Figure 4-40 shows three STM images acquired during a voltammetry sweep between 3 V and 0.005 V at a scan rate of 5 mV/s.

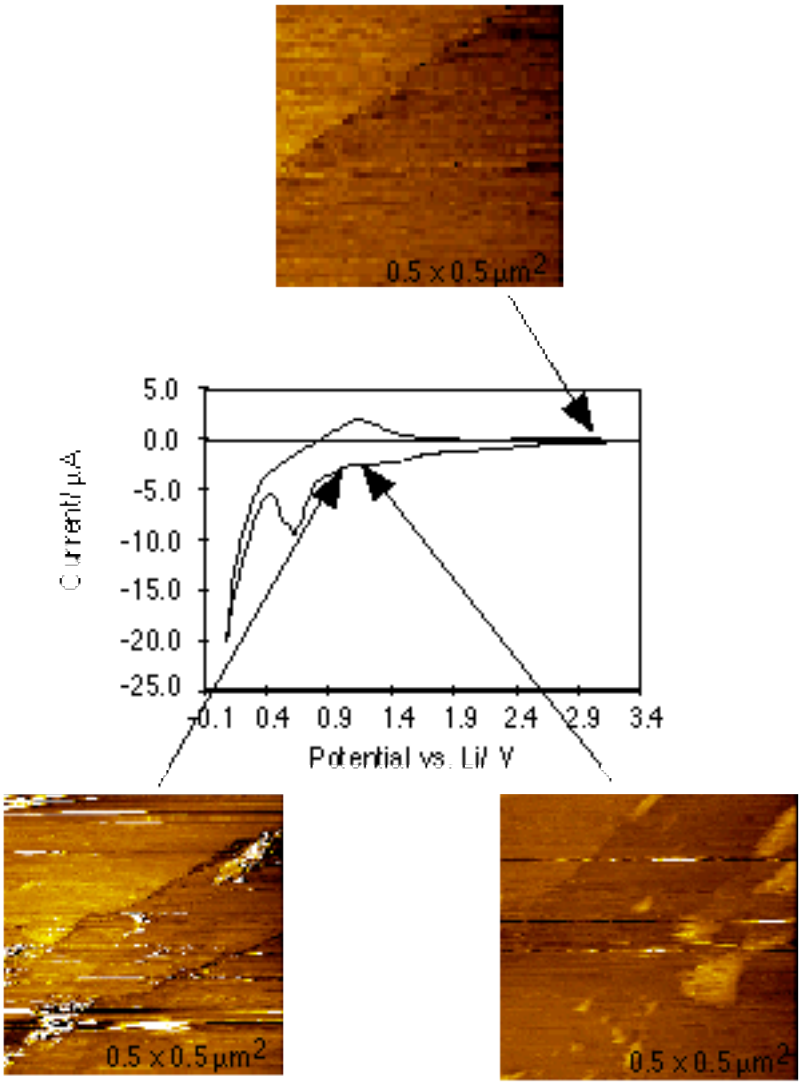

Figure 4-40: STM images and corresponding voltammogram (scan rate 5 mV/s) acquired during discharge and charge of a HOPG electrode in 1 M $LiClO_4$ (EC:DMC). Potentials vs. Li/Li^+.

For potential lower than 1.2 V, islands 15 Å high appear soon. Such islands are similar to the hill-like structures imaged for the first time by Inaba et al. [104]. These islands were attributed to the intercalation of solvent molecules, like ethylene carbonate and/or dimethyl carbonate.

Because the SEI film formed within the first cycle covers the surface of the electrode preventing further electronic conductivity, STM technique is strongly limited [104]. As a consequence, the same experiment was repeated by in situ AFM. Results are shown in the following paragraph.

4.3.3 In situ AFM of SEI film formation

Figure 4-41 shows the first two voltammetric cycles of HOPG recorded between 3 V and 0.01 V. The voltammograms were recorded in situ during electrochemical AFM experiments at a scan rate of 5 mV/s.

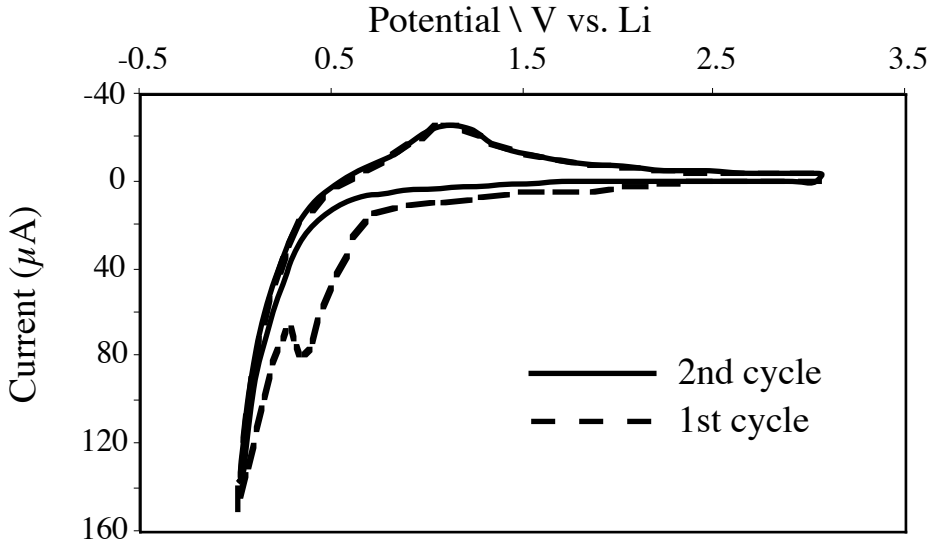

Figure 4-41: Cyclic voltammetry curves recorded with basal planes on HOPG in 1 M $LiClO_4$ in EC:DMC (1:1), at a scan rate of5 mV/s. Dashed line: 1st cycle; solid line: 2nd cycle.

In the first cathodic scan (dashed line in Figure 4-41) the reduction current increases rapidly at potentials more negative than 0.7 V and forms a characteristic cathodic peak centered at 0.4 V. This peak is only observed during the initial reduction (charging) sweep and was attributed to formation of a SEI film on the HOPG electrode surface[105]. Recent investigations revealed that the ethylene carbonate solvent[106] is decomposed in this potential window. As soon as the potential is

more negative than 0.3 V, the cathodic current increases again until the reversal point is reached.

During the discharge sweep only one anodic counter-peak appears. The large cathodic rise of the current below 0.3 V and the corresponding anodic counter-peak at about 1.1 V are the result of lithium intercalation into carbon facilitated by the many defects present on the basal HOPG surface. In the second cycle with the same electrode (solid line in Figure 4-41), the characteristic peak centered at 0.4 V is absent, which constitutes proof that SEI film formation was complete after the first cycle. It is of interest to know whether the SEI film starts to be formed preferentially near an edge plane. Therefore, the atomic force microscope was focused on an area of the HOPG crystal where a 32 nm high step was located. Several images were acquired at 3 V without noticing any change of the step with time. Then the potential was scanned from 2.6 V to 1.3 V, still without any noticeable change in morphology of the basal plane. The same step area was finally imaged between 1.3 V and 0.1 V. As shown in Figure 4-42a, between 1.3 V and 0.7 V still nothing observable happens.

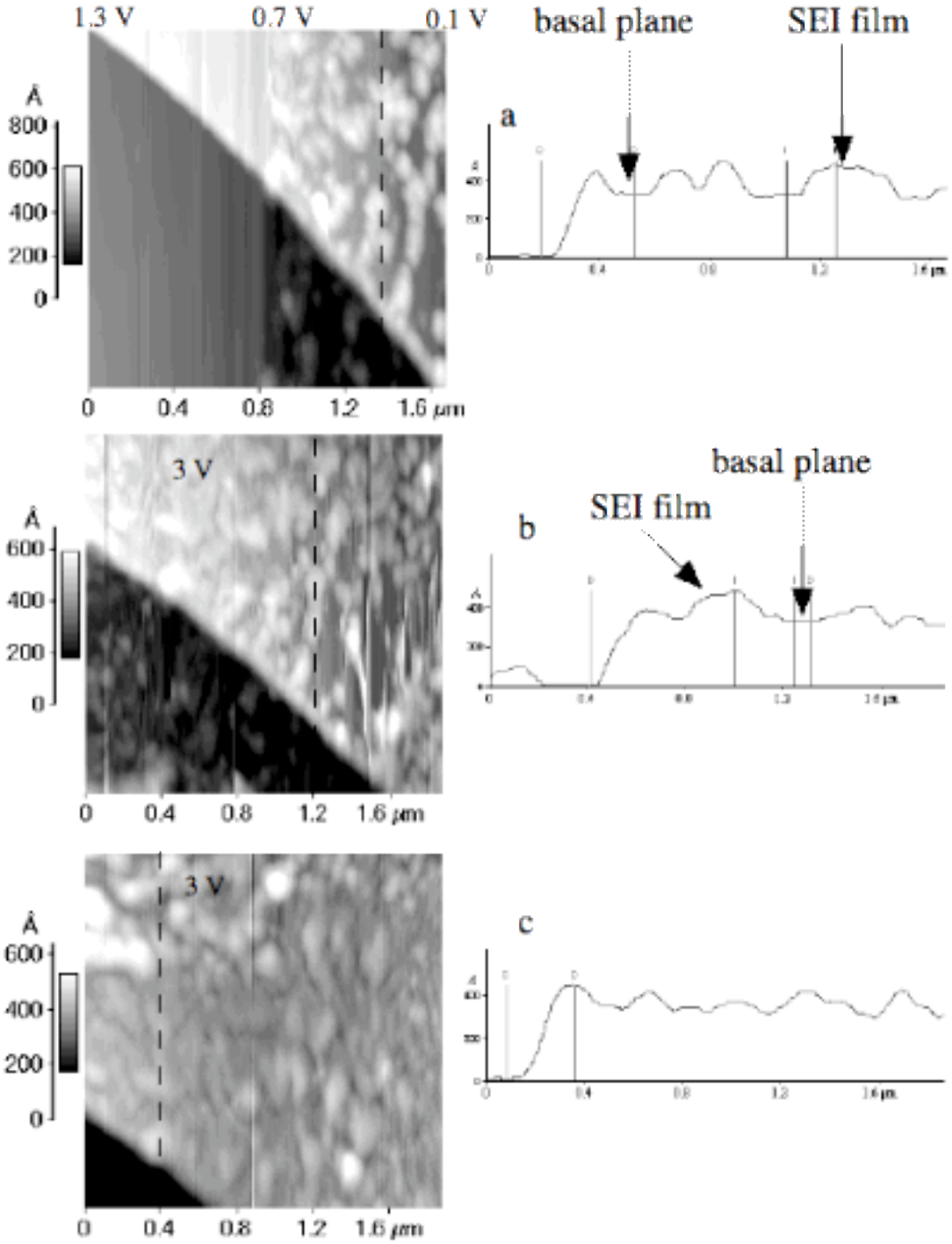

Figure 4-42: Three AFM images of the same HOPG step location in 1 M $LiClO_4$ (EC:DMC). The images were acquired by scanning from left to right with a continuously changing or constant potential. Potential scales: (a) from 1.3 V to 1.1 V; (b) 3V after the 1st cycle; (c) 3 V after the 2nd cycle. For each AFM image the acquisition time was 4 min 16 s. The vertical profiles related to the marked regions are shown on the right.

At 0.7 V_{Li} a film starts to cover the surface of the HOPG electrode. Apparently, this SEI film is formed by deposits, which appear exactly simultaneously at step-edge and basal plane surface, i.e. at exactly the same value of potential. However, the SEI film formed within the fast (5mV/s) first voltammetric half cycle covers the basal

plane only partially. In fact, as can be seen from the vertical profile recorded at about 0.5 V, some areas are completely flat, and the relative height is 32 nm, i.e. it corresponds to the initial thickness of the step. Therefore, a film has not yet formed on these areas. According to the same vertical profile, the thickness of the existing film is 15 nm.

The same area was then imaged at a constant potential of 3 V after one complete cycle. Figure 4-42b shows that now the SEI film is more dense but still does not fully cover the HOPG surface. The corresponding vertical profile still reveals film sections 15 nm high. Figure 4-42c shows the SEI film imaged at 3 V after two complete cycles. The surface of the HOPG electrode is now fully covered by a compact film with an average roughness of 4 nm. The vertical profile indicates that no discontinuities are present in the SEI film. Subsequent AFM images did not reveal other relevant changes in morphology of the electrode surface.

From the dense and compact SEI film present after the second cycle, a square portion was removed by increasing the pressure of the scanning AFM tip in order to measure the film thickness. An enlarged area, including the scraped square in the middle, was then imaged. To minimize further compression of the SEI film surrounding the scraped square, a lower loading force was applied. Vertical (topographic) deflection and lateral (friction) signals were recorded simultaneously. Figure 4-43 show topography and friction images of the same area.

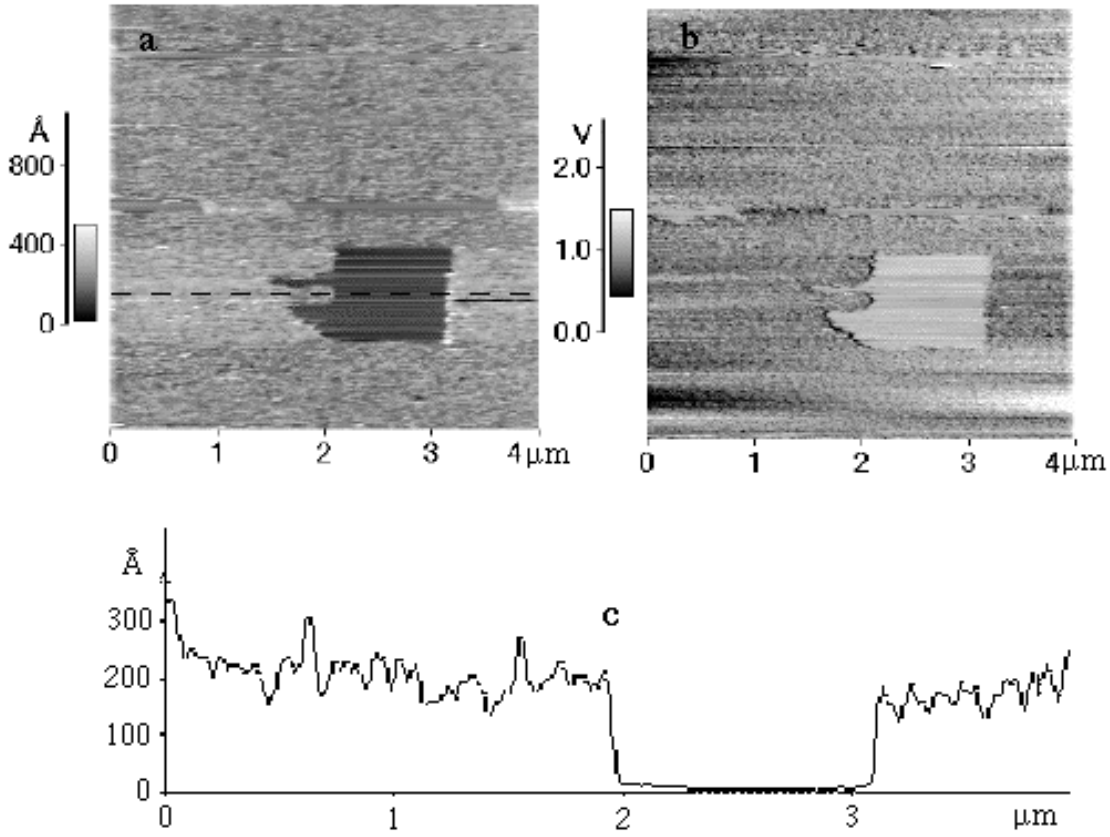

Figure 4-43: Simultaneous AFM (a) and LFM (b) images of the SEI film formed on the HOPG electrode after 2 cycles between 3 V and 0.01 V. A portion of the film was removed in advance from the HOPG surface by increasing the pressure of the scanning AFM tip. The vertical profile (c) shows that the SEI film thickness is 25 nm.

The exactly opposite changes in the friction coefficient found inside and outside the scraped square demonstrate that the SEI film was completely removed by the scraping. Hence the HOPG substrate was fully exposed. This also implies that with a vertical profile across the scraped area one can quantify the thickness of the top film. As shown in Figure 3c, the SEI film has a thickness of about 25 nm.

The AFM images and the cyclic voltammetry data are in excellent agreement with literature data on SEI. The CV indicates that a major reduction reaction occurs at potentials more negative than 0.7 V, while by AFM the start of formation of a surface film is observed at about the same potential. It is therefore reasonable to argue that the species imaged by AFM in our experiments are identical with the SEI film.

We found no evidence for the particles observed by Chu et al. [107] at potentials more negative than 1.6 V at edge locations of HOPG in the same electrolyte. We also did not see any feature similar to the hill-like structures reported by STM for HOPG in EC:DEC-based electrolyte [108] and in our previous STM experiment (see paragraph 4.3.2). However, our potential scan rate was quite fast as compared to that used in Chu's AFM study and Inaba's STM experiments. In our experiments, therefore, the time resolution probably was too poor for an observation of the intercalation of solvated molecules suggested by the solvent co-intercalation model proposed by Besenhard et al. [109].

The imaging conditions were quite critical, and had to be set correctly. When the loading force of the AFM tip was too high, the SEI film was destroyed. To the contrary, when the loading force was too low, the contact between tip and surface was immediately lost, preventing any further imaging. Since a small increase in tip pressure was enough to destroy the film, we may assume that the SEI film is extremely soft and, therefore, of a polymeric rather than inorganic nature.

4.3.3.1 Thickness of the SEI film vs. charge-discharge cycling

The SEI film formation process was also investigated as a function of the cycle number. The potential of the working electrode was cycled from 3 V_{Li} to 0 V_{Li} at a scan rate of 10 mV/s. The corresponding voltammograms are shown in Figure 4-44.

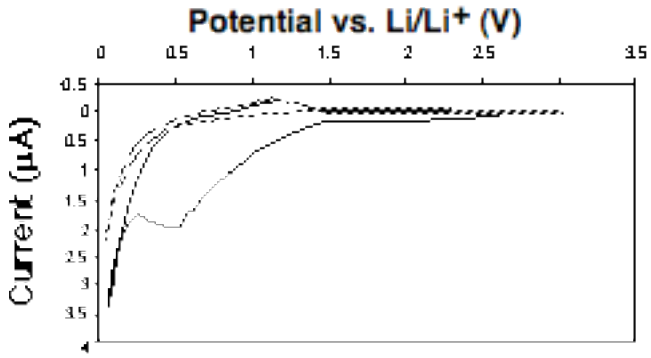

Figure 4-44: First and second cyclic voltammograms of HOPG in 1 M $LiClO_4$ (EC:DMC) at 10 mV/s. Solid line: 1st cycle; dashed line: 2nd cycle.

The SEI film thickness was studied as a function of the number of charge-discharge cycles by in situ AFM. To measure the film thickness, a 0.5 × 0.5 μm^2 square was scratched in the middle by increasing the loading force and imaging speed, and by switching the feedback off. Therefore the surface of the electrode was imaged at a lower force. The same procedure was extended up to 10 charge-discharge cycles. As an example, the hole obtained by this technique and the corresponding height's profile are shown in Figure 4-45. The measurement was performed after ten cycles and the final thickness of the SEI film is ca. 45 nm.

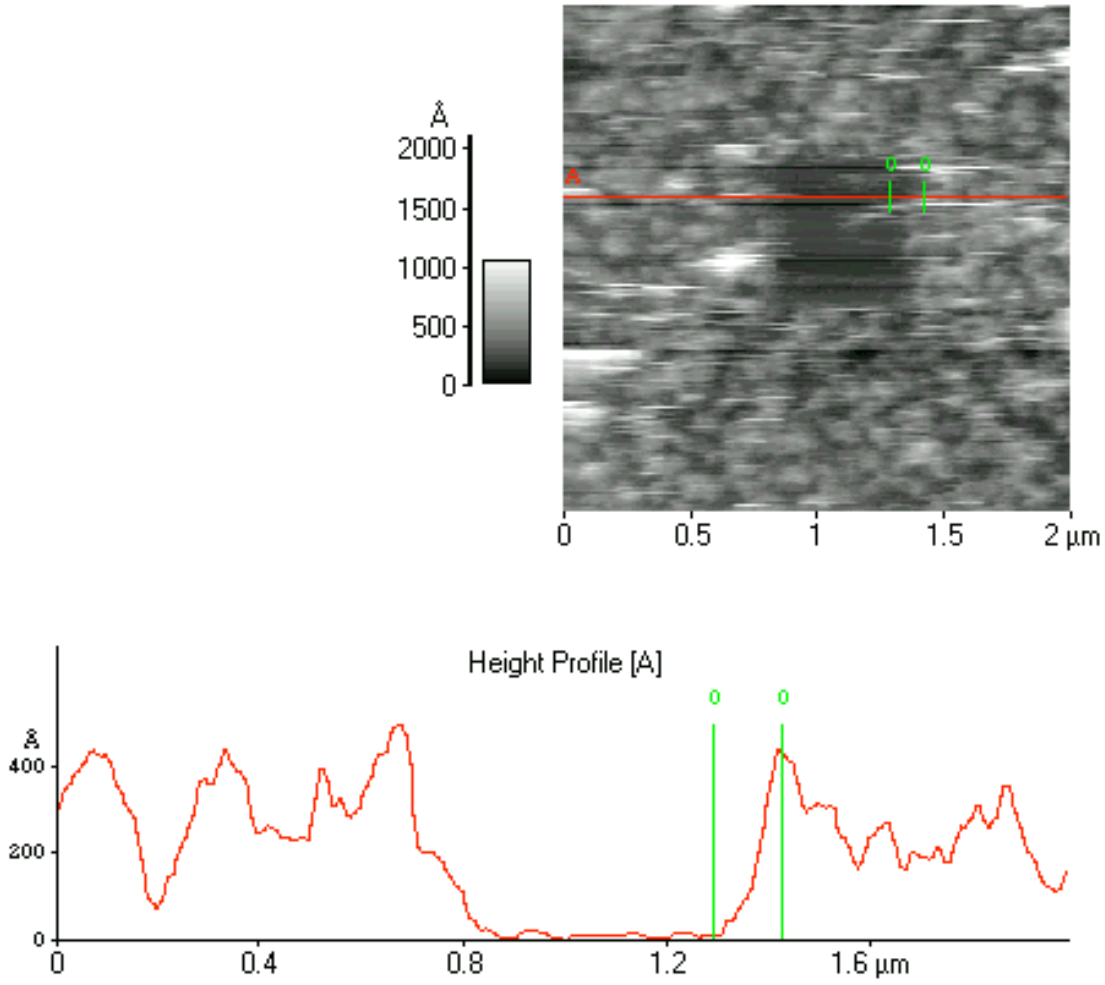

Figure 4-45: AFM picture of the SEI film on HOPG after 10 charge-discharge cycles in 1M $LiClO_4$ (EC:DMC). A square zone in the middle was previously scratched to remove the SEI film. Below the AFM picture, the corresponding height's profile is also shown. The difference in height between the two markers is 45 nm.

After 2-3 charge-discharge cycles the SEI film is still growing. Then, as depicted in Figure 4-46, its thickness is rather constant.

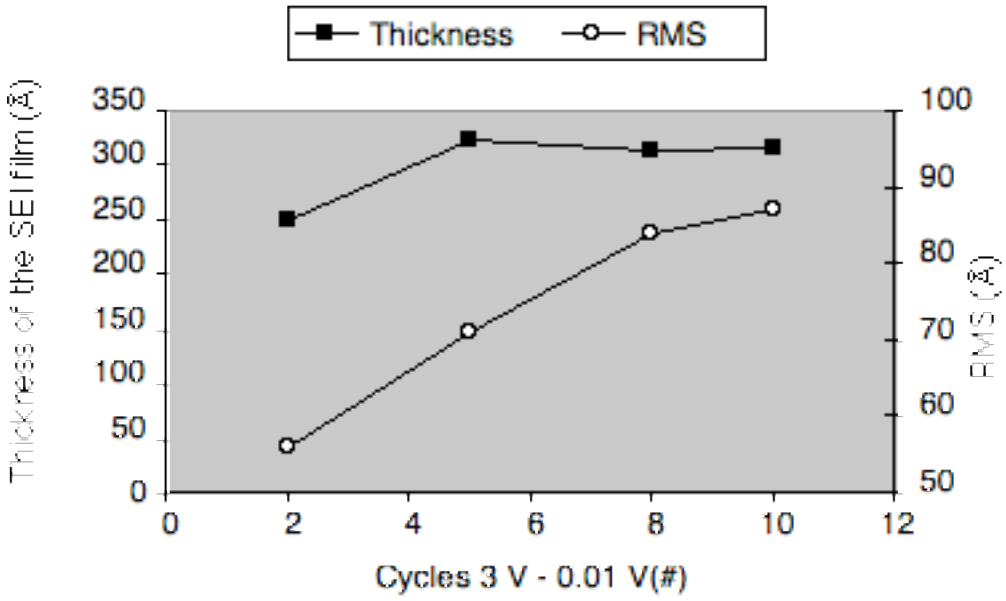

Figure 4-46: Thickness and roughness of the SEI film on HOPG as a function of the number of cycle. The SEI film is formed in 1 M LiClO4 by cyclic voltammetry at a scan rate of 10 mV/s.

The average roughness of the SEI film increases with the number of cycles from 56 Å to 87 Å within the first ten cycles. This is an indication that the charge-discharge procedure can still affect the surface morphology of the HOPG electrode even after several cycles. On the contrary, the thickness of the SEI film normally reaches a limit value within few cycles.

Our results indicate that the SEI film formation is not a process that can be concluded in one potential scan. Thickness measurements show evidence that the film grows during the first 2-4 cycles.

Nevertheless, It has to be considered that these experiments were performed at a scan rate of 10 mV/s, which is considerably high compare to the charge-discharge rate of a typical graphite electrode for battery systems. It cannot be excluded that at a considerably slower scan rate the film has more chance to be completed within the first cycle, as indicated by the cyclic voltammetry investigation at 400 μV/s (see paragraph 4.3.1).

4.3.3.2 Dependence of the SEI film upon the electrolyte water content

As recently observed by F. Joho et al. [110, 111], the presence of trace water in the electrolyte solutions can affect strongly the SEI film formation and causes an increasing irreversible charge loss in the first cycle of lithium intercalation into graphite electrodes. To investigate the influence of water, which is a common impurity in

electrolytes, on the morphology of the SEI film, HOPG electrodes were intercalated in solutions of 1 M $LiClO_4$ (EC:DMC) with different water content.
The first and the second CVs acquired in the electrolyte solution with a water content of ca. 20 ppm is shown in Figure 4-47.

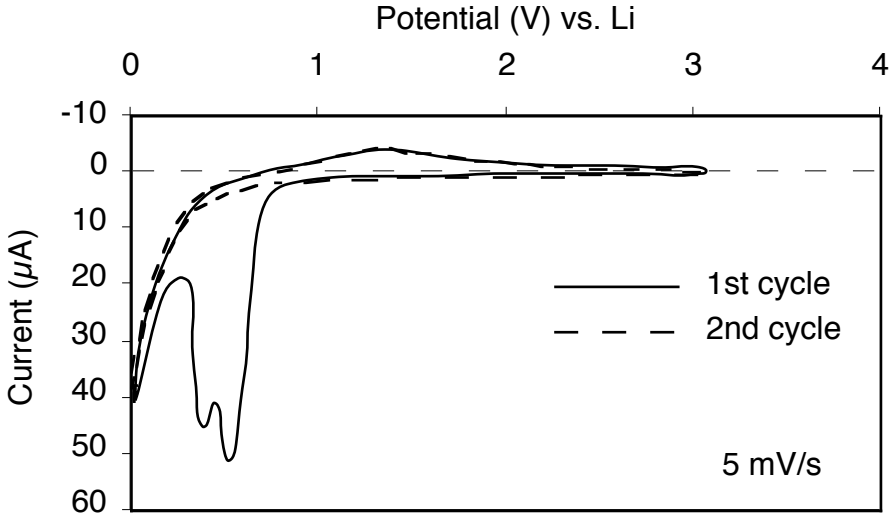

Figure 4-47: First (solid line) and second (dashed line) cyclic voltammogram of HOPG in 1 M $LiClO_4$ (EC:DMC) at a scan rate of 5 mV/s. The water content of the electrolyte is 20 ppm.

As indicated by the first and second voltammograms, the formation of the SEI film starts at 0.75 V_{Li} and is finished within the first cycle. The cathodic sweep does not show any other reactions until 0.75 V_{Li} is not overcame.
The corresponding topography after two cycles between 0 and 3 V vs. Li/Li^+ is shown in Figure 4-48. The film exhibits a compact globular structure and no relevant discontinuity.

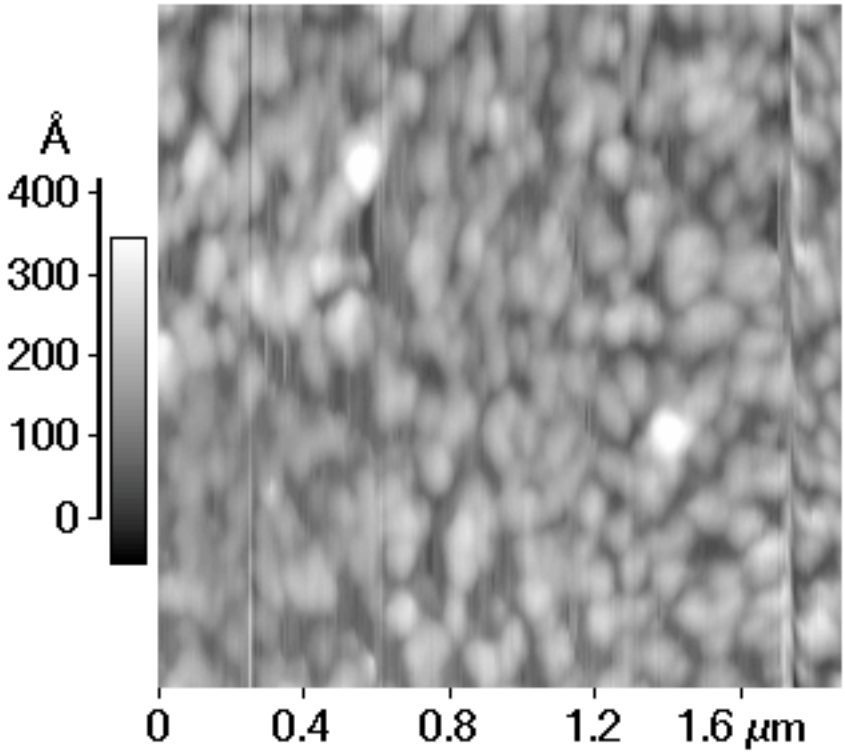

Figure 4-48: In situ AFM picture of a SEI film formed on HOPG in 1 M $LiClO_4$ (EC:DMC). Scan rate 5 mV/s. Water content 20 ppm. The SEI film was imaged at a speed of 1 Hz and a nominal loading force of 2 nN, in contact mode.

A second electrode was intercalated at the same scan rate in a solution contaminated with ca. 500 ppm of water. The corresponding first cyclic voltammogram is shown in Figure 4-49.

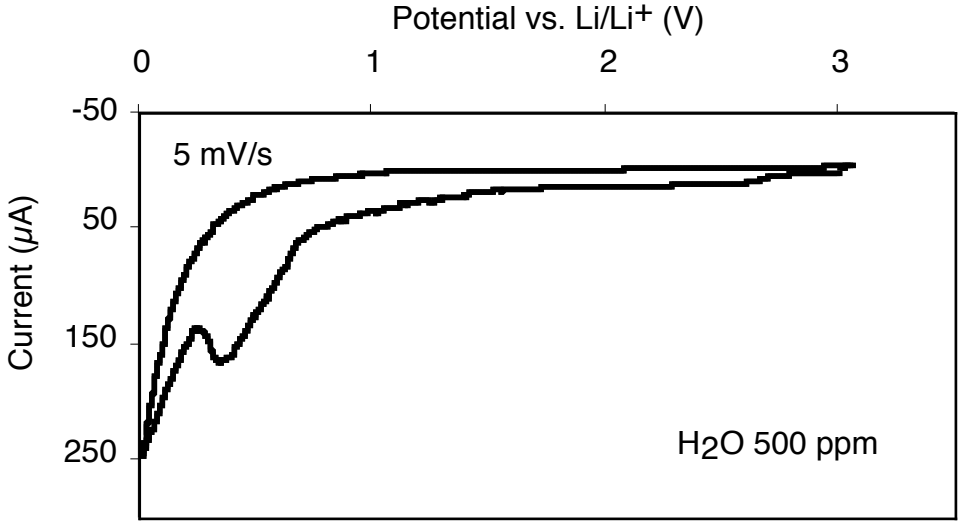

Figure 4-49: First voltammogram of HOPG in 1 M $LiClO_4$ (EC:DMC) at a scan rate of 5 mV/s. Water content ca. 500 ppm.

The voltammogram exhibits a first increase in the cathodic current for potential below 2.8 V_{Li} and a second higher increase at ca. 1.3 V_{Li}. The associated electrochemical reaction is probably due to the reduction of water, which is starting also at 1.3 V_{Li}. The absence of any anodic counter peak indicates the irreversibility of the reduction processes. The surface of the HOPG electrode was imaged by in situ AFM at 0.9 V vs. Li/Li^+ at zero current flowing. The corresponding picture is shown in Figure 4-50. At this potential the basal planes exhibit hill-like islands and several blisters, the origin of which is not clear, but possibly correlated to the water reduction and the following production of bubble of hydrogen under the graphene sheets.

The same area was then imaged at 3 V after the SEI film was formed (Figure 4-51). Despite the resolution of the image is not ideal, the SEI film seems to cover the most of the basal plane surface.

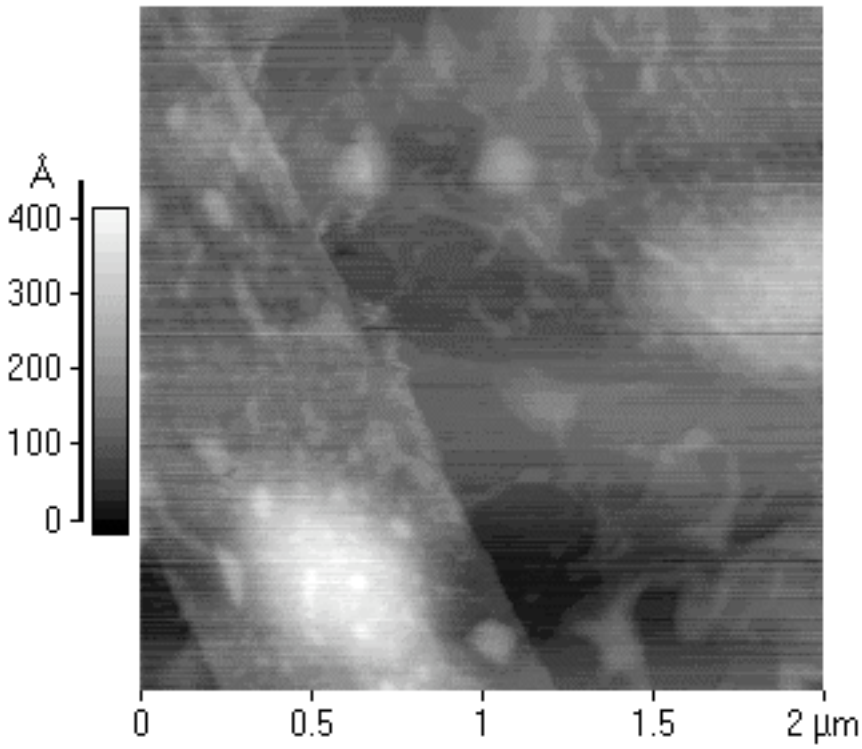

Figure 4-50: In situ AFM picture of the HOPG electrode in 1 M $LiClO_4$ (EC:DMC) solution with water content of ca. 500 ppm. Image acquired at a constant potential of 0.9 V vs. Li/Li^+ at zero current flowing. Scan speed 1 Hz. Nominal applied force 2 nN.

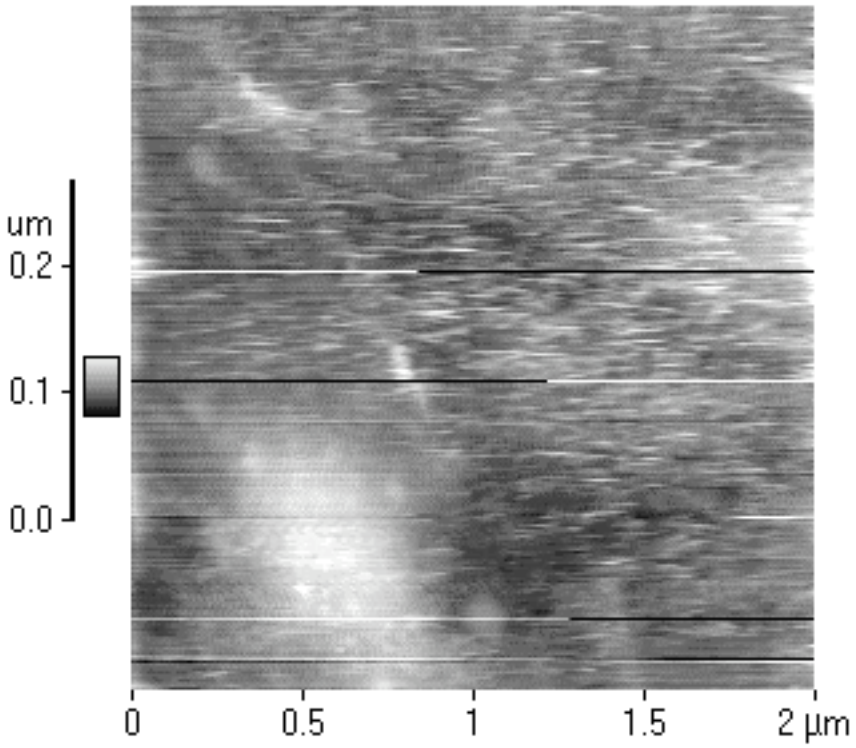

Figure 4-51: : In situ AFM picture of the SEI film formed in 1 M $LiClO_4$ (EC:DMC) solution with a water content of ca. 500 ppm. Image acquired at a constant potential of 0.9 V vs. Li/Li^+ at zero current flowing. Scan speed 1 Hz. Nominal applied force 2 nN.

A third HOPG electrode was charged in an electrolyte solution contaminated with ca. 5000 ppm of water.

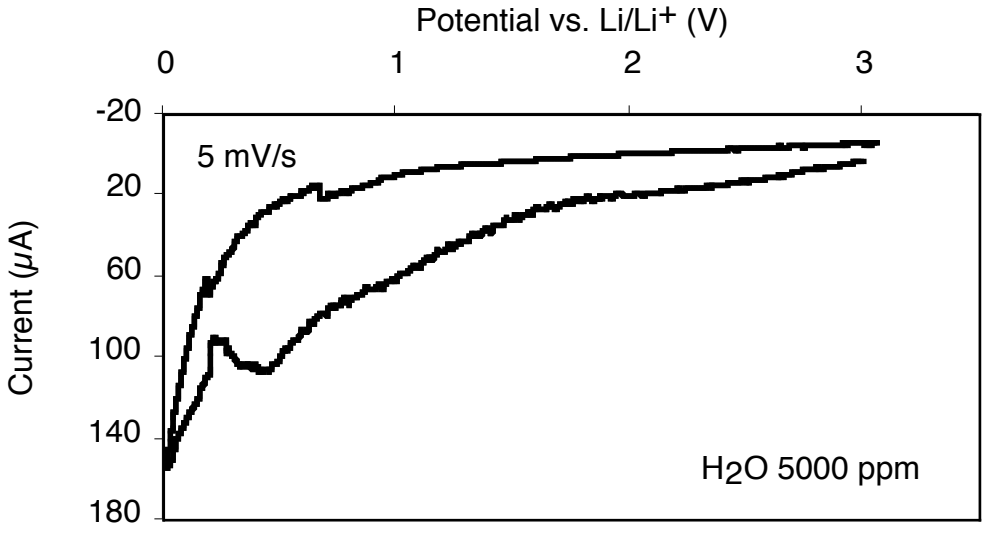

Figure 4-52: First voltammogram of HOPG in 1 M LiClO4 (EC:DMC) contaminated with ca. 5000 ppm of water. Scan rate 5 mV/s.

As indicated by the voltammogram shown in Figure 4-52, the cathodic current peak assigned to the intercalation of solvated Li ions and the formation of a SEI film is shifted to more negative potential with increasing water content. Furthermore, the anodic current tends to disappear indicating that irreversible electrochemical reactions are taking place at the electrode.

The morphology of the corresponding SEI film is shown in Figure 4-53. The film in this case does not cover completely the surface of the HOPG electrode. A huge amount of basal plane is still exposed to the electrolyte. Therefore further intercalation of the solvated molecules is still possible. This is probably the reason for a higher loss of charge in the first cycle of lithium intercalation.

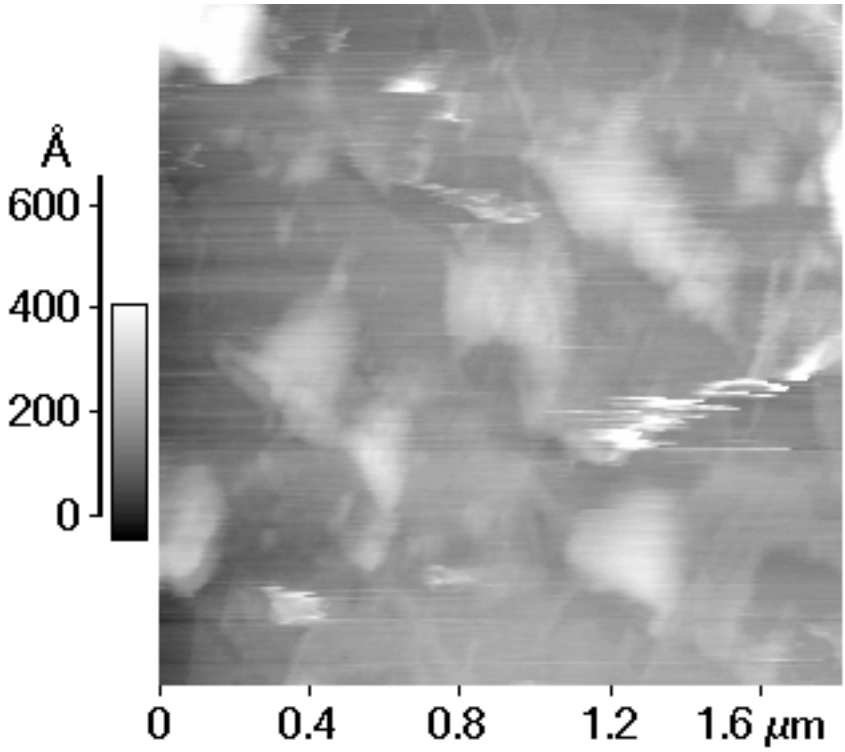

Figure 4-53: In situ AFM picture of the SEI film formed on HOPG in a solution contaminated with ca. 5000 ppm of water. Scan speed 1 Hz. Nominal loading force 2 nN.

From in situ measurements we know that the infrared spectra and, thus, the SEI layers are similar on different carbons [112]. For convenience, therefore, we chose the basal surface of HOPG for our SEI morphological study. In EC:DMC solvent the SEI starts to form at ca. 0.7 V vs. Li, which is after the start of ethylene evolution [38]. Our in situ AFM results show that the SEI is very rough at first, and does not cover the whole surface of the electrode, while later the SEI film covers the entire surface. Therefore, combining our results with literature data we can conclude that at first the carbonate solvents are reduced, forming ethylene gas, organic radicals and

polymers. Then a SEI film precipitates on the surface via a nucleation and growth mechanism.

4.4 Carbon films

The scaling down of electronics circuits and the introduction on the market of microelectromechanical (MEMS) devices motivated a strong increasing demand for miniaturized power sources. The conventional microbattery is typically formed by depositing thin layers of the positive electrode, negative electrode and solid electrolyte on a substrate material [113, 114]. Recently, another approach to fabricate microbatteries was proposed [115] and carbon films produced by pyrolysis of photoresist materials are now under investigation as a new type of anode material for developing micro-batteries [116].
Spin coating thin layers of photoresist on silicon wafers and subsequent photolithographic patterning are well-developed technologies in the semiconductor industry [117]. The microscopic structures that are routinely produced provided an opportunity to fabricate useful microstructures for microbatteries. In this direction interdigitated microelectrodes of carbon films have been already presented [118], but still many characteristics of these carbon materials are unknown.
With the intent of study the application of carbon films as negative electrode for microbatteries, Carbon films made from positive and negative photoresist materials were characterized in terms of morphology, electronics properties and electrochemical behavior in organic electrolytes by ex situ and in situ tool of analysis.

4.4.1 Resistance of Carbon films

4.4.1.1 Carbon films by positive Photoresist (OiR)

Carbon films produced by pyrolysis of the OiR photoresist at 600°C, 700°C, 800°C, 900°C and 1000°C (see paragraph 3.5.2 for more details on the pyrolysis procedure) were investigated by Current Sensitive Atomic Force Microscopy (CSAFM). This technique allows to map the surface conductivity of a material and can be used to investigate locally the characteristic current – potential dependence. More experimental details about CSAFM are illustrated in paragraph 3.3.4.

To be sure that the resistance measurement was not influenced by the roughness of the sample, the average morphology of the carbon films was characterized by contact-AFM. The roughness dependence upon the pyrolysis temperature is shown in Figure 4-54.

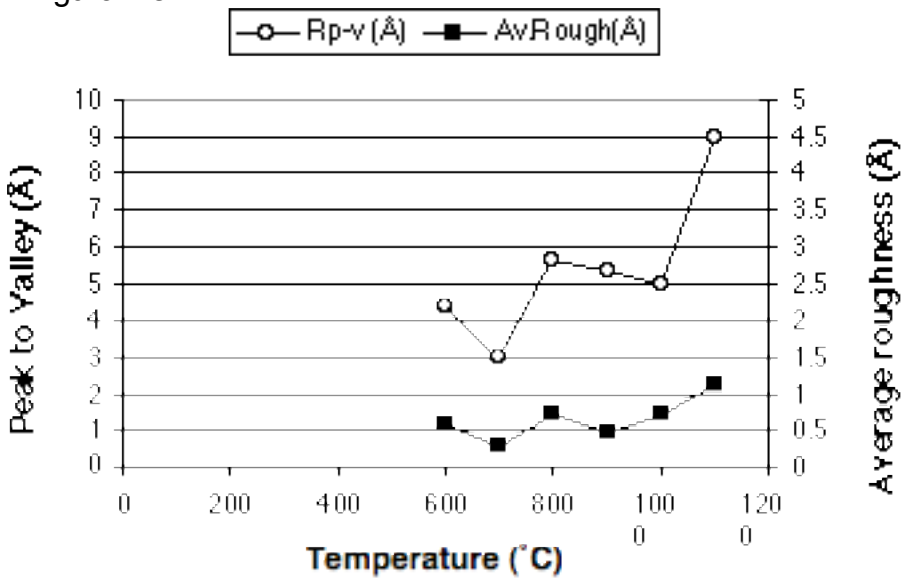

Figure 4-54: Peak to Valley distance and Roughness vs. pyrolysis temperature for OiR carbon films imaged by AFM in contact mode.

Both roughness and peak to valley distance are only slowly increasing with the temperature. Therefore, the pyrolysis process seems not to affect the roughness of the carbon films, strongly. We can conclude that the CSAFM method should not be influenced by the morphology of the carbon films, since all the films exhibit a very flat surface, independently by the pyrolysis temperature.

The sample pyrolyzed at 1000°C presents a homogenous surface conductivity. Even by applying a small bias of 50 mV, most of the time the current signal is completely saturated. In some occasion the current sensitive measurement reveals the presence of a surface layer which is less conductive than the rest of the carbon film. Figure 4-55 shows the typical surface conductivity picture and the corresponding topography.

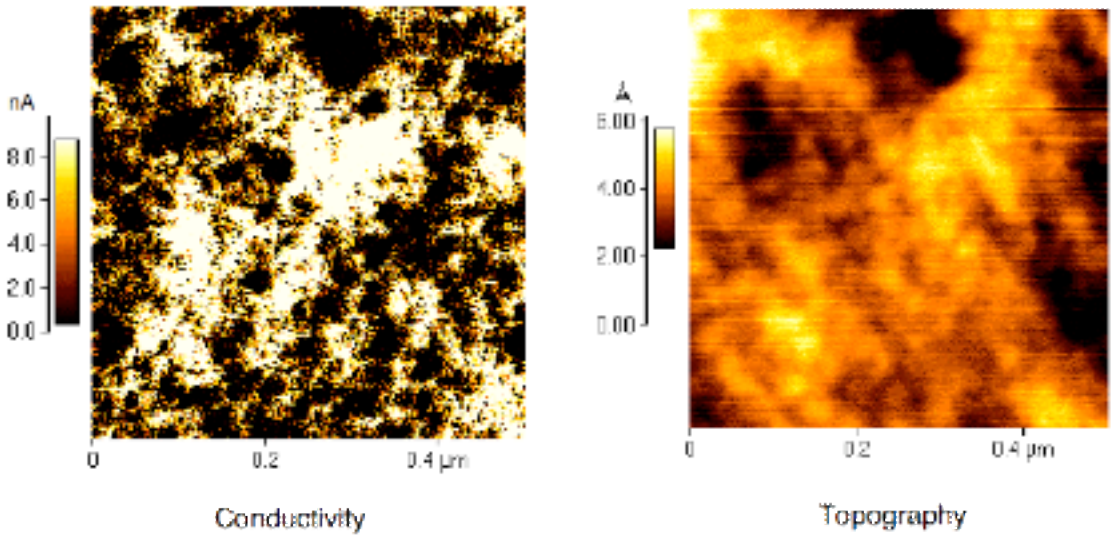

Figure 4-55: 1000°C carbon film imaged by CSAFM at a tip to sample bias of +0.05V. Bright and dark areas indicate low and high conductivity, respectively. The conductivity map is shown on the left, while the topography signal is shown on the right.

At a bias of +0.05 V (dark indicates high conductivity; white indicates low conductivity) there is a clear match between high areas in topography and areas low in conductivity. The electrical properties of the surface layer are better described by the current-potential dependence of the carbon film. I-V curves were acquired in different points of the surface. As shown in Figure 4-56, in a high conductivity region the current is linearly proportional to the bias voltage, which is typical for an ohmic-like conductive material.

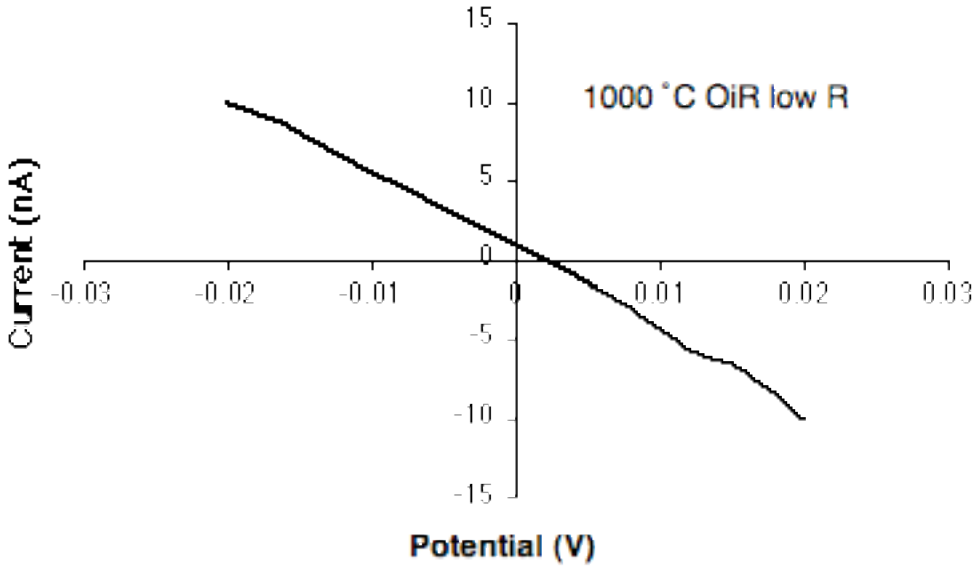

Figure 4-56: I-V dependence on a high conductivity region of an OiR carbon film pyrolyzed at 1000°C.

For bias voltage higher than ± 20 mV, the current signal is saturated because the maximum current detectable is limited to ± 10 nA by the preamplifier.
The I-V curves acquired in the low conductivity regions show a non-ohmic behavior (Figure 4-57). Curves are normally asymmetric and only by applying higher bias voltages (± 2 V) the current signal saturates the preamplifier.

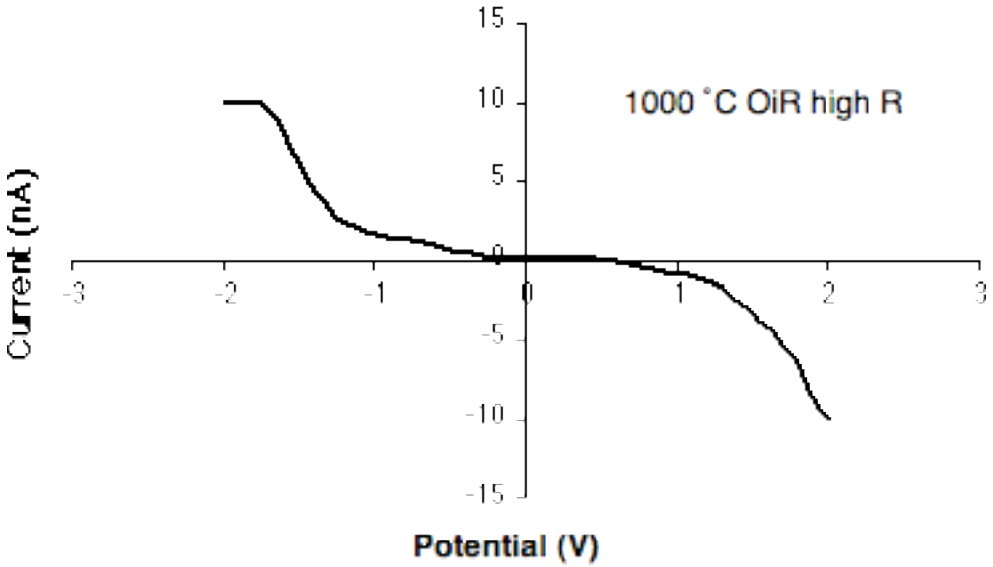

Figure 4-57: I-V dependence on a low conductivity region of an OiR carbon film pyrolyzed at 1000°C.

Similar results were obtained from the samples pyrolyzed at 800°C and 900°C.
The samples pyrolyzed at 600°C presents a very low conductivity. The typical I-V dependence is shown in Figure 4-58. The curvature shown here indicates the non-ohmic resistance behavior of the material. Similar results were obtained in each point investigated.

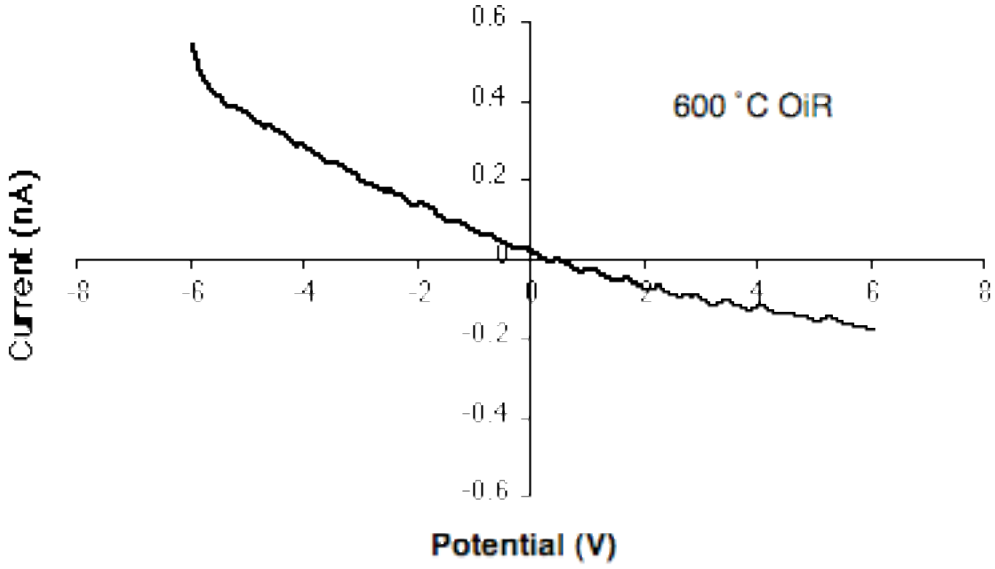

Figure 4-58: I-V dependence for an OiR carbon film pyrolyzed at 600°C.

The resistance of the carbon films pyrolised at different temperatures was determined from the slope of the corresponding I-V characteristic dependence. In Figure 4-59 the resistance is plotted vs. the pyrolysis temperature.

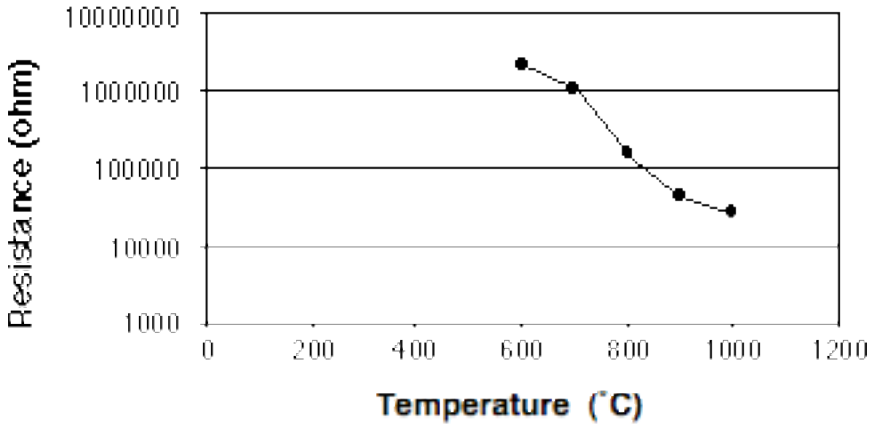

Figure 4-59: Local resistance of OiR carbon films measured by CSAFM method.

To see whether the local resistance determined by CSAFM is a real indication of the average surface resistance, the four-point probe technique was performed on the same set of samples to measure the sheet resistance of the carbon films. For comparison with the CSAFM result, the equivalent resistance plot obtained by four-point probe technique is shown in Figure 4-60.

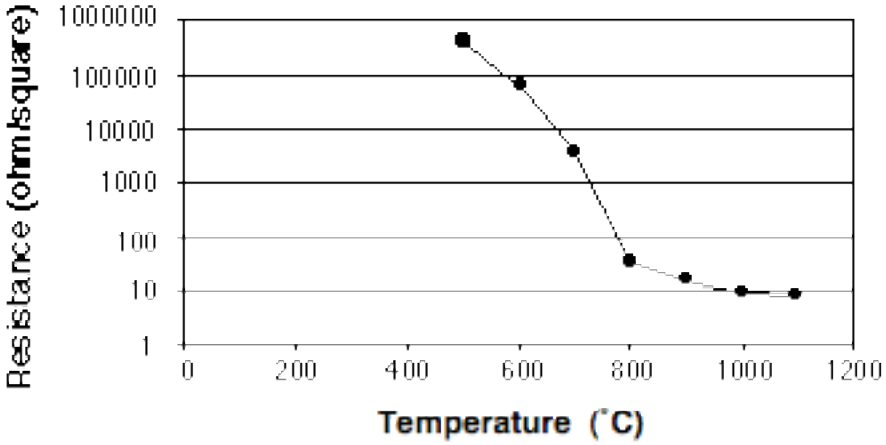

Figure 4-60: Sheet resistance of OiR carbon films measured by four-point probe method.

The local resistance determined by CSAFM is in excellent agreement with the electrical sheet resistance measured by the four-point probe method. In both cases, the resistance of the carbon films produced at 600°C and 700°C is high,

but decreases for films produced at temperatures above 700°C. Very similar results were obtained for carbon films from other photoresists [119].
The major difference between the two methods concerns the absolute scale of the measured resistance. Unluckily, the CSAFM is affected by the tip-sample contact area, which is normally very difficult to be determined. As a consequence, only relative measurements can be performed by CSAFM, while the true resistivity of the material cannot be estimated. Anyway, the advantage of the CSAFM method with respect to the four-point probe technique is that the local conductivity of the material can be correlated with the surface morphology down to the nanometer scale. Furthermore, the current-potential dependence can be also investigated.

4.4.1.2 Carbon films by negative photoresist (XPSU)

To see any effect of the photoresist material used, we studied also carbon films made from a negative photoresist.
Three samples pyrolyzed at different temperatures were imaged by CSAFM. Figure 4-61 shows the typical conductive map for a film carbonized at 1000°C.

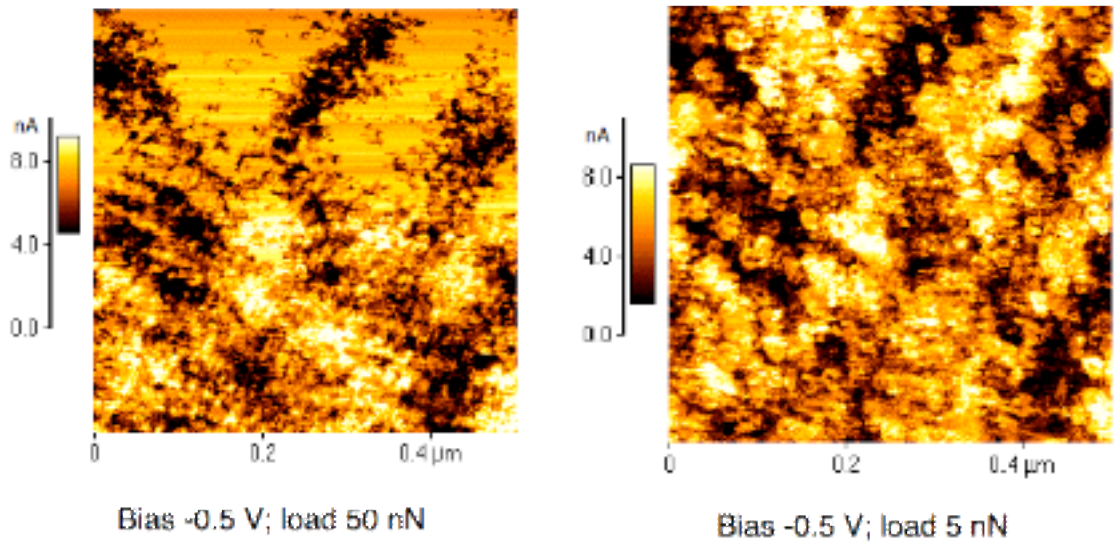

Figure 4-61: Carbon film pyrolyzed at 1000°C imaged by CSAFM in Nitrogen. Bias –0.5 V; load 50 nN (left), 5 nN (right). Bright and dark indicate high and low conductivity, respectively.

The carbon film exhibits regions with very high conductivity and areas with lower conductivity. By decreasing the loading force of the cantilever, i.e. the contact area, more details are visible. The left image of Figure 4-61 shows ring-like fine structures which are not visible in the right image acquired on the same area at a loading force an order of magnitude higher.
The carbon film pyrolyzed at 800°C presents a similar behavior. The resistance of the carbon film pyrolyzed at 600°C was so high that any conductive measurement was prevented.

Generally, OiR carbon films show conductivity higher than XPSU carbon films pyrolyzed at the same temperature. A typical example is shown in Figure 4-62 where two films carbonized at the same temperature (800°C), but from different photoresists, are compared. The mapping of the surface conductivity shows large bright areas for the positive carbon film, which is depicted, on the left in Figure 4-62. This result proves that the most of the positive carbon film is conductive, while a lower percentage of the negative carbon film is conductive.

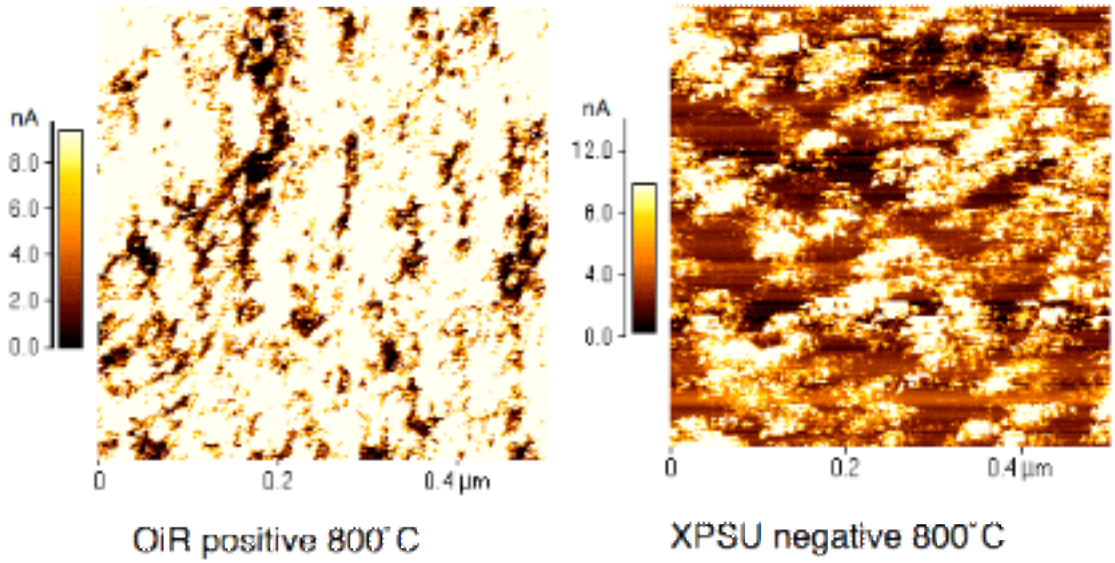

Figure 4-62: Conductivity map of OiR positive carbon film (left) and XPSU negative carbon film (right) imaged by CSAFM in Nitrogen. Bias –0.5 V; load 50 nN. Bright and dark indicate high and low conductivity, respectively.

Nevertheless, it has to be considered that the carbon films from negative photoresist where prepared ca. 10 months before the CSAFM characterization, while the positive photoresist carbon films were studied only a few days after being produced. Therefore, we cannot exclude that the older carbon films were oxidized more than the younger ones, as they were stored in air. At the moment it is not clear whether the conductivity is influenced by the oxidation effect or by the physico-chemical properties of the starting photoresist materal. We suspect that the higher resistance of the negative carbon film is only an age effect. In fact, the resistance-pyrolysis temperature trend is similar for the two types of carbon films. Furthermore, previous investigation of carbon films from different photoresists by four-point probe method did not show any difference in resistance behavior [116].

4.4.1.3 Raman of Carbon films

Raman spectroscopy is a powerful and sensitive technique to study the microstructure of carbonaceous materials [120, 121, 122, 123]. The development

of the characteristic sp^2 carbon bands at ~1360 (D) and ~1600 cm^{-1} (G) can be easily followed by this method.

For this reason Raman spectroscopy was applied to characterize the carbon films made from OiR positive photoresist.

Raman spectra of fresh carbon thin films produced by pyrolysis at 700°C and 900°C are shown in Figure 4-63. The two carbon bands at ~1360 (D) and ~1600 cm^{-1} (G) are clearly visible in both samples. The G band is related to the symmetry of the E_{2g} vibrational mode of graphite, which is due to the motion of the carbon atoms in the hexagonal graphite lattice. Therefore, the wave number and the bandwich of the G band are correlated to the structural order within the carbon sheet. The D band is usually attributed to vibrational modes, which originate from the disruption of the delocatized electronic structure of the graphite layer. This two bands were studied extensively in literature and their peak area ratio (D/G ratio) were correlated with disorder of the sp^2 carbon matrix [124, 125, 126]. A larger D/G ratio indicates greater disorder. Here, higher pyrolysis temperatures cause narrowing of the D band which indicates that the disorder is decreasing with the increasing temperature.

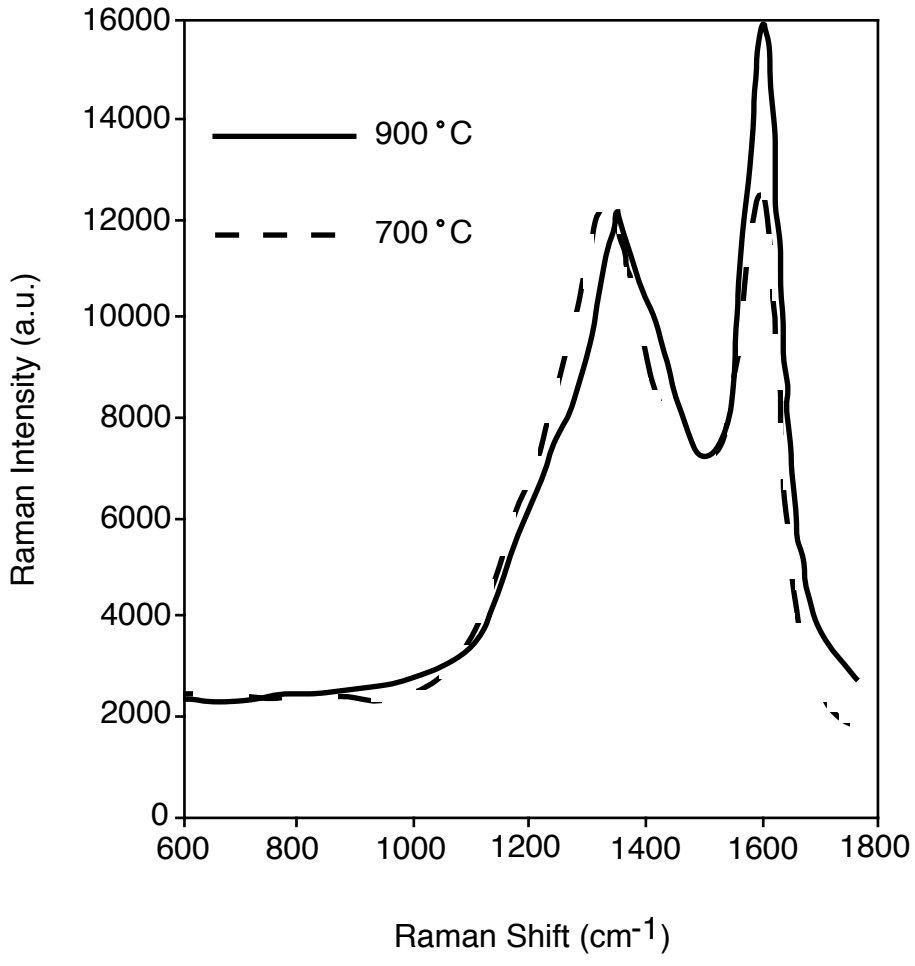

Figure 4-63: Raman spectra of Carbon films pyrolyzed at different temperatures. The narrowing of the D band indicates that the disorder is decreasing with the increasing temperature.

These results are in agreement with recent investigations on different photoresists pyrolyzed in the same range of temperatures [119].

4.4.1.4 XPS of carbon films

As complementary to the Raman study of vibrational modes, the electronic properties of the carbon films were investigated by XPS. In particular, the XPS study was performed to determine the oxygen coverage of the films, based on O1s and C1s peak area ratios.

Figure 4-64 shows the survey spectrum of a carbon film pyrolyzed at 900°C from the positive photoresist. Oxygen, Carbon and traces of Silicon, because of the substrate, were revealed.

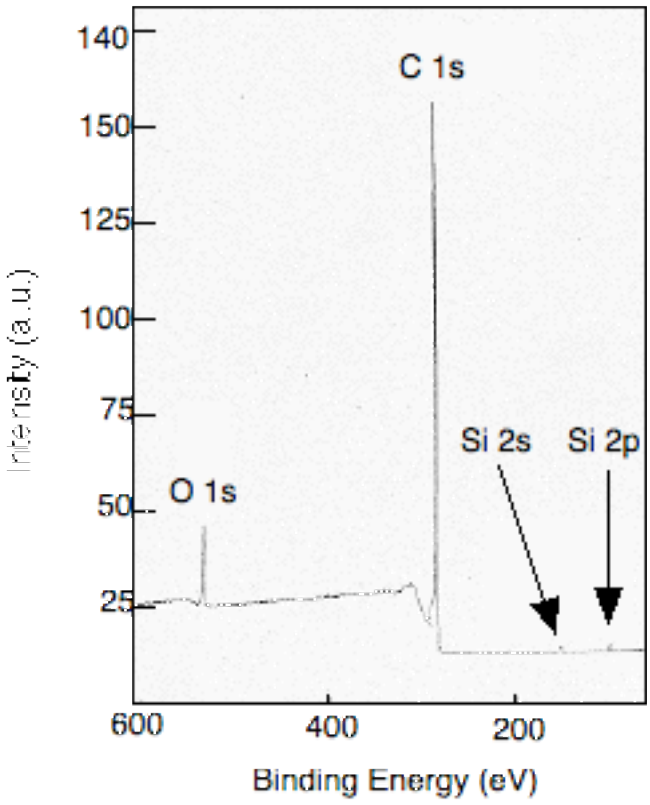

Figure 4-64: Low resolution XPS spectrum of an OiR carbon film pyrolyzed at 900°C.

High resolution spectra of the O1s and C1s regions for the same sample are shown in Figure 4-65 and Figure 4-66, respectively.

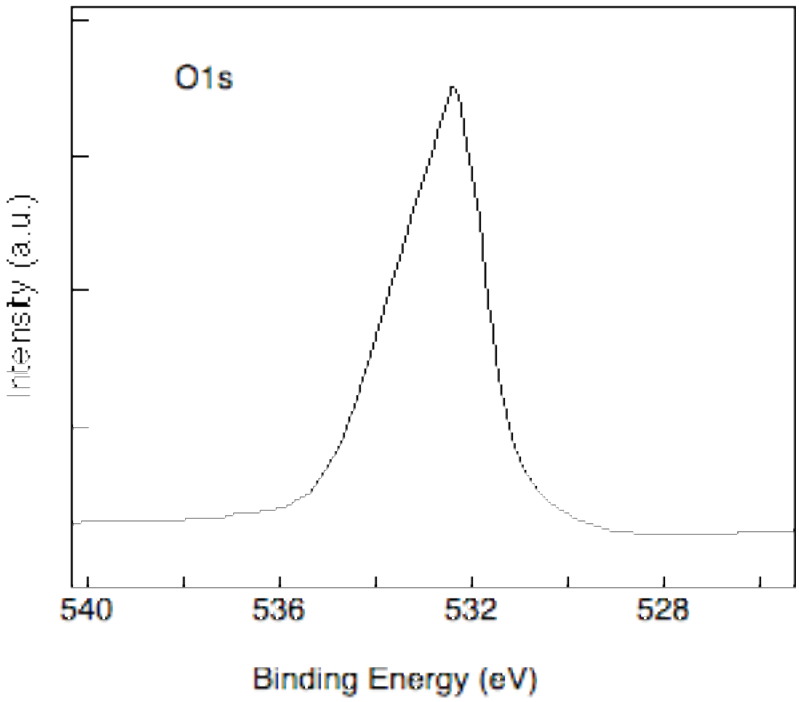

Figure 4-65: High resolution XPS spectrum of the O1s region for an OiR carbon film pyrolyzed at 900°C.

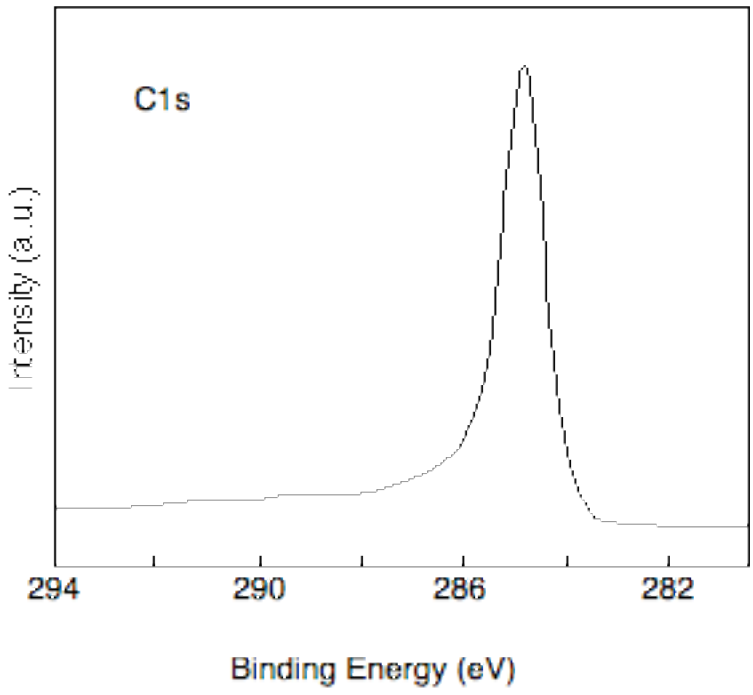

Figure 4-66: High resolution XPS spectrum of the C1s region for an OiR carbon film pyrolyzed at 900°C.

Similar spectra were measured for the OiR carbon films pyrolyzed at different temperatures (500°C to 1100°C). The atomic O/C ratio as a function of the pyrolysis temperatures is shown in Figure 4-67.

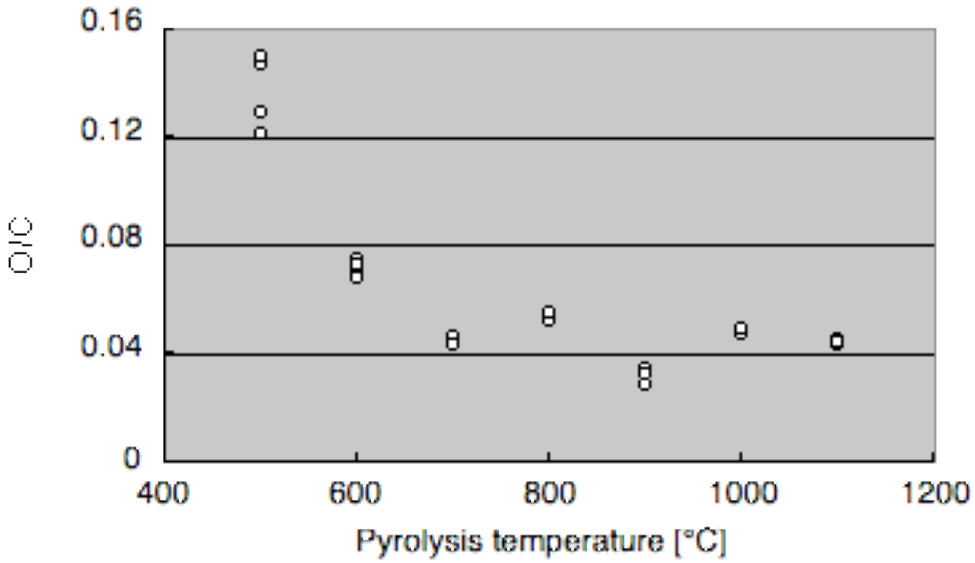

Figure 4-67: O/C atomic ratio vs. pyrolysis temperature for OiR carbon films.

The main result is that the O/C ratio clearly decreases with the increasing temperature.

The full width at half maximum (FWHM) for the C1s peaks is shown in Figure 4-68 as a function of the temperature.

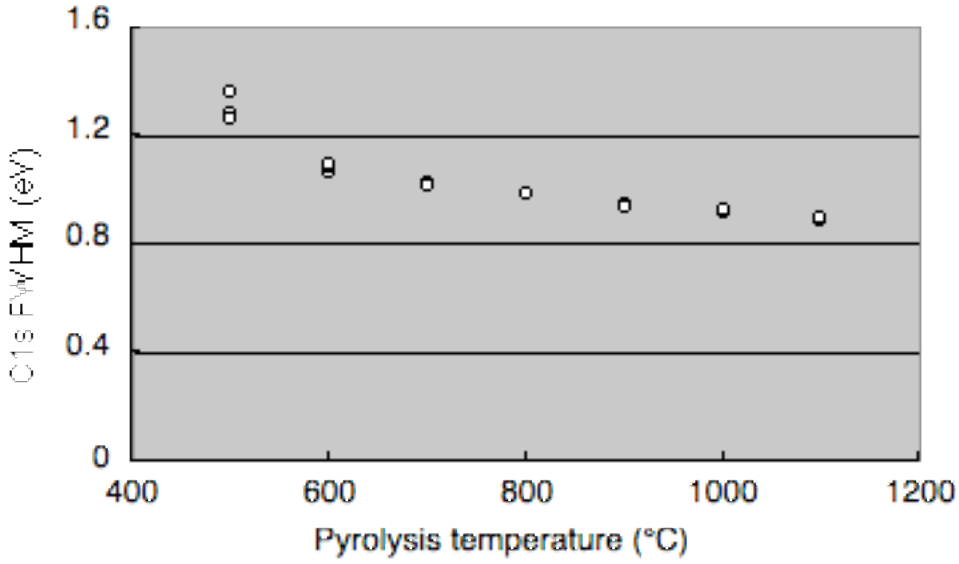

Figure 4-68: FWHM of the C1s peaks for OiR carbon films pyrolyzed at different temperatures.

The FWHM of the C1s level decreases with pyrolysis temperature (500°C to 1100°C), indicating that the level of graphitization of the carbon films increases with the temperature in agreement with the previous Raman result.

The same XPS study was repeated on carbon films made from the negative photoresist. The results shows that the O/C ratio decreases with the increasing

temperature of pyrolysis, but the absolute amount of oxygen detected on the negative carbon films is higher than on the positive carbon films.

As shown by the CSAFM and four point probe results the resistance of both carbon films decreases sharply for pyrolysis temperature higher than 700°C. A similar behavior was reported by Schueller et al. [127] in their studies of glassy carbon obtained by pyrolysis of polymeric precursors. This change in the resistance is believed to be due to changes in the physico-chemical composition of the film (for example, H/C ratio) as the pyrolysis temperature increases [128, 129]. Our XPS results indicate a possible correlation with the O/C ratio, too. The general higher oxygen content observed on the carbon films analyzed after ten months suggests that the lower resistance measured on these films is only due to an age oxidation effect.

The results here described indicate that the electrical properties of carbon films can be controlled over a wide range by varying the pyrolysis temperature. This variation in resistance and film composition affects the electrochemical behavior and is discussed in the next paragraph.

4.4.2 In situ electrochemical AFM of SEI film formation

The electrochemical behavior of the same set of carbon films obtained by pyrolysis of OiR photoresist and previously characterized by CSAFM, Raman and XPS was investigated in non-aqueous electrolyte. OiR photoresist carbonized at 900°C for 1 hour was studied by in situ AFM in 1 M $LiClO_4$ (EC:DMC), during charge-discharge cycles from 3 to 0 V vs. Li, at 5 mV/s. Charging the carbon film at potentials close to 0 V_{Li} is expected to induce the formation of a SEI film at about 0.7 V_{Li} and, possibly, intercalation of Li ions for potentials below 0.4 V_{Li}.

The first four cyclic voltammograms are depicted in Figure 4-69. The first cycle shows an increasing cathodic current for potentials below 1.2 V, with a peak at 0.4 V.

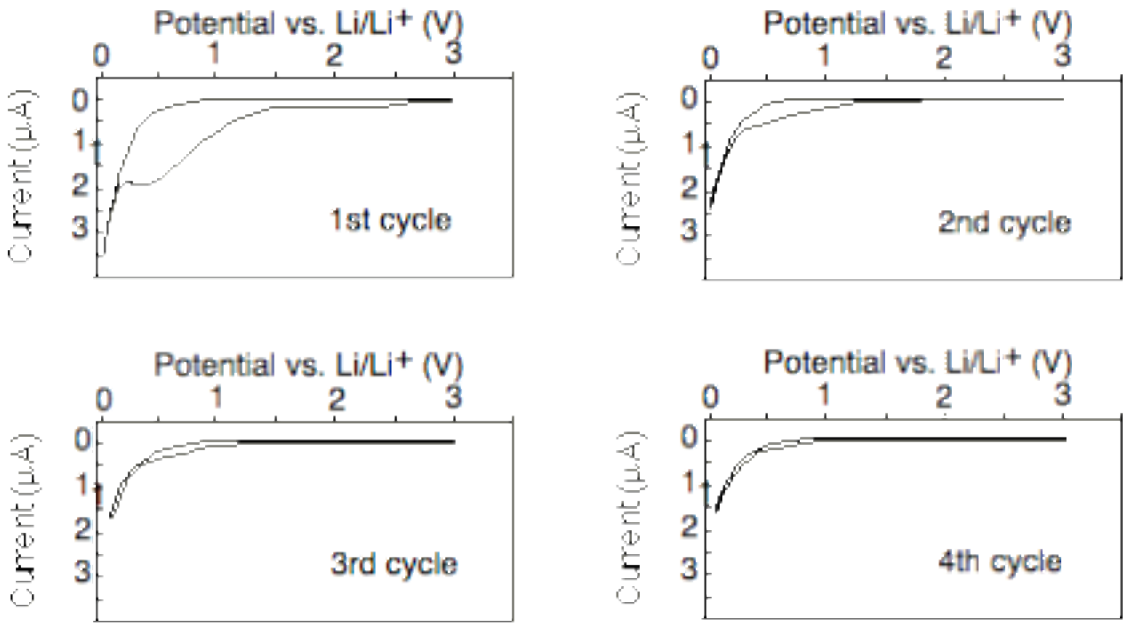

Figure 4-69: First four cyclic voltammograms of 900°C OiR Carbon film in 1 M $LiClO_4$ (EC:DMC) at 5 mV/s.

The absence of other peaks between 3 V and 1.5 V proves that side reactions like decomposition of water were minimized. As a consequence the cathodic peak located at 0.4 V can be mainly addressed to SEI film formation processes, i.e. to the electrochemical reduction of the electrolyte. The presence of this peak, even though smaller, in the following two cyclic voltammograms indicates that the SEI film formation process apparently is not completed within the first charge-discharge cycle, but still in progress during the following 2-3 cycles, at least at this particular scan rate. A further increase in cathodic current close to 0 V is correlated to Li insertion. The absence of anodic current counter-peaks should indicate that Li insertion is negligible in the carbon film.

The thickness of the SEI film formed on the carbon electrode was also studied as a function of the number of charge-discharge cycles by in situ AFM. As for thickness measurements of SEI films on HOPG, a square portion was removed from the dense and compact SEI film, by increasing the pressure of the scanning AFM tip. An enlarged area, including the scraped square in the middle, was then imaged. To minimize further compression of the SEI film surrounding the scraped square, a lower loading force was applied.

After two cycles between 3 V and 0 V, the SEI film was about 140 Å thick as shown by the height's profile in Figure 4-70 acquired at 3 V.

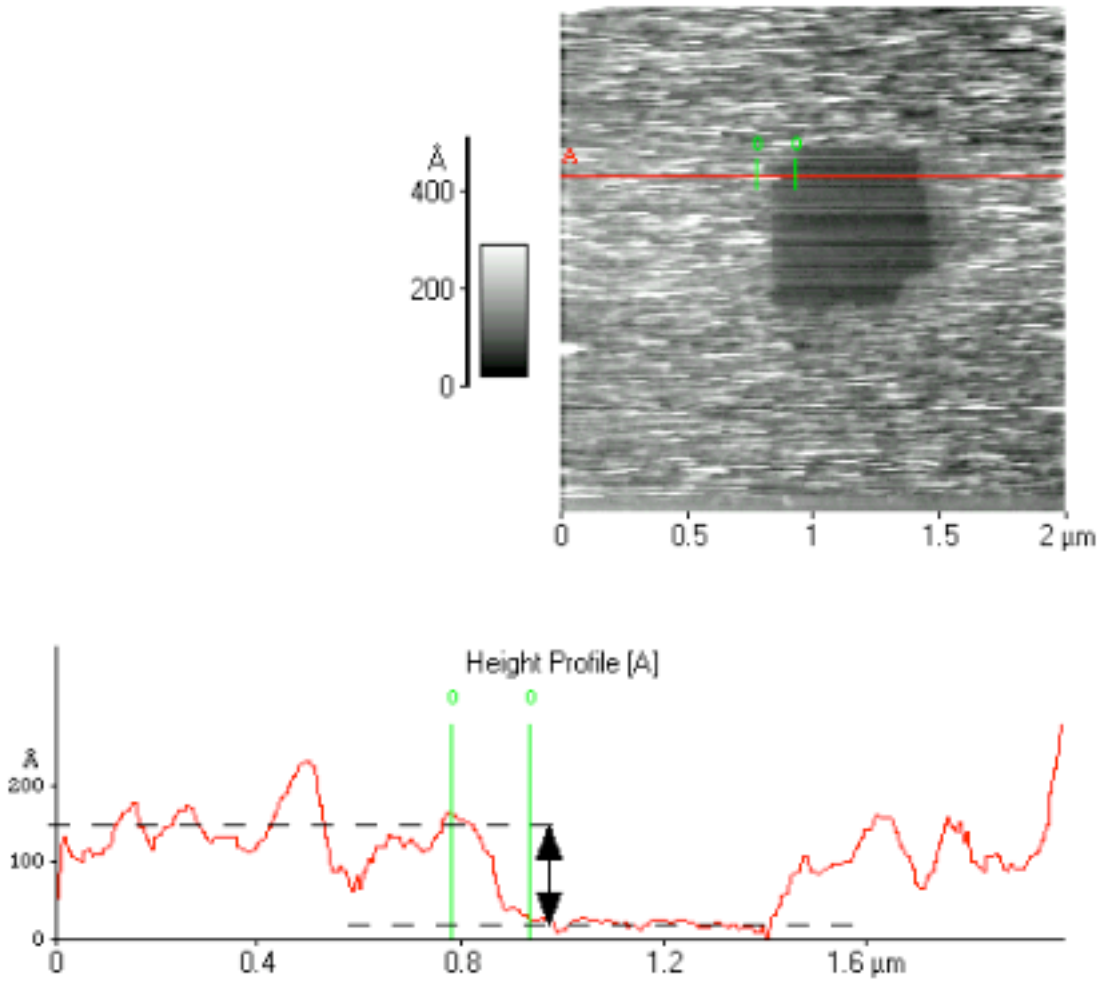

Figure 4-70: AFM image of the SEI film formed on a 900°C Carbon electrode in 1M $LiClO_4$ (EC:DMC). The SEI thickness is about 140 Å. Image acquired at 3 V after two cycles.

Since the surface of the SEI film formed was rough, the thickness of the film was determined by considering the average height of the SEI film and of the carbon substrate.

Therefore, with the same procedure the thickness of the SEI film was measured up to six cycles. The corresponding thickness and RMS values are plotted in Figure 4-71.

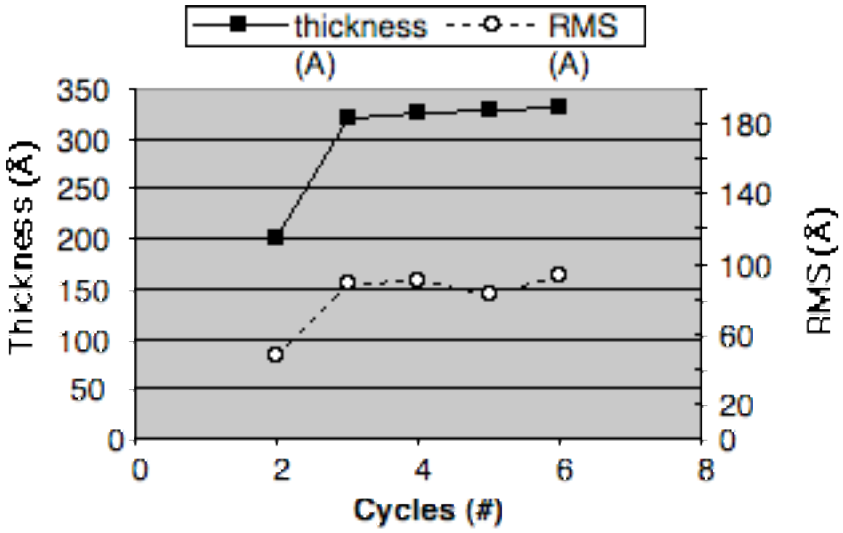

Figure 4-71: Thickness and RMS of the SEI film formed on the 900°C Carbon electrode as function of the cycle life. Electrode imaged by in situ AFM during cyclic voltammetry between 3 V and 0 V vs. Li in 1 M $LiClO_4$ (EC:DMC).

Both quantities reach a constant value within three cycles. The thickness grows to about 325 Å while the RMS changes from 47 Å to 93 Å.

The same study was extended to an OiR film carbonized at 700°C. The voltammograms show a cathodic current density lower than the electrode pyrolyzed at 900°C. Apparently the formation of the SEI film is finished within three cycles as indicated in Figure 4-72.

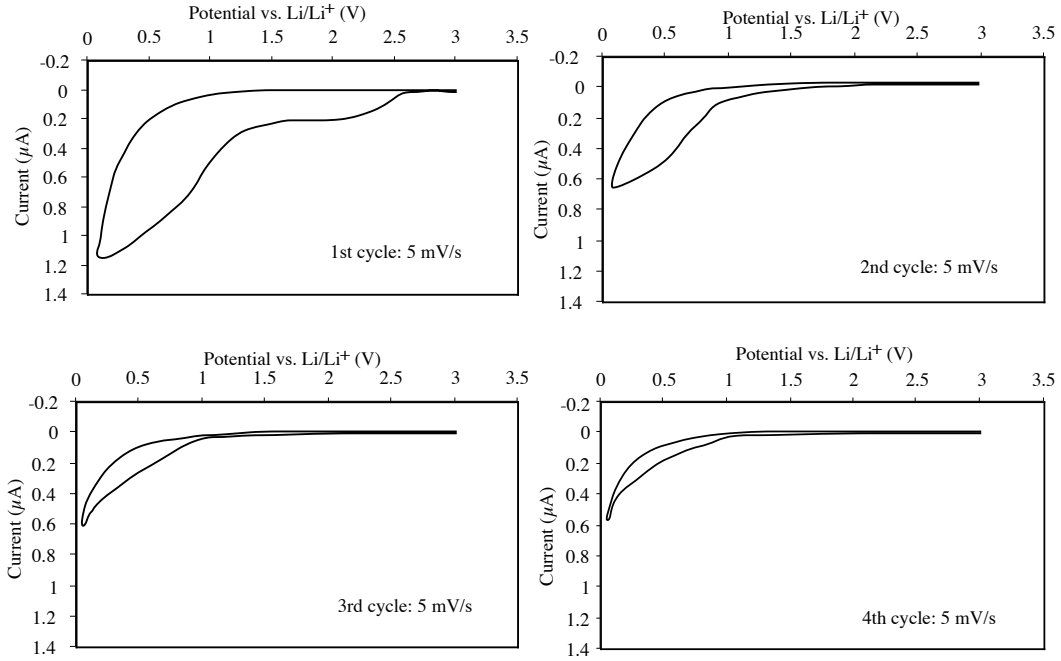

Figure 4-72: First four voltammograms of a 700°C Carbon electrode in 1M $LiClO_4$ (EC:DMC) recorded at a speed of 5 mV/s.

After the first cycle the SEI film was 150 Å thick, while it was 200 Å after the second and 230 Å after the third cycle. The RMS value was always close to 40 Å, independent of cycle number. The complete sequence of measurements is shown in Figure 4-73.

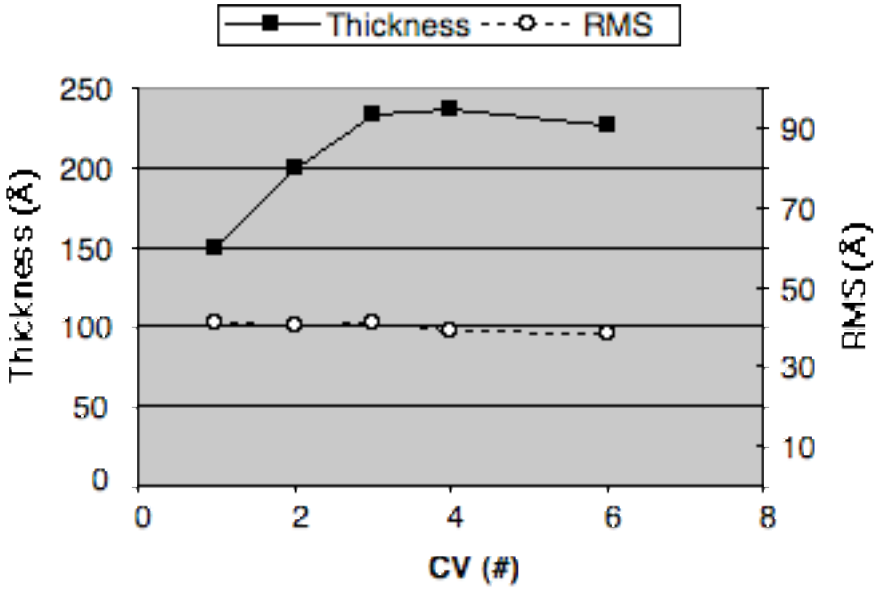

Figure 4-73: Thickness and RMS of the SEI film on the electrode pyrolyzed at 700°C.

The in situ electrochemical AFM study confirms that the electrochemical activity of the carbon films in organic electrolyte depends on the pyrolysis temperature. For example, carbon films obtained at 900°C show a cathodic current much higher than carbon films produced at 700°C (Figure 4-74).

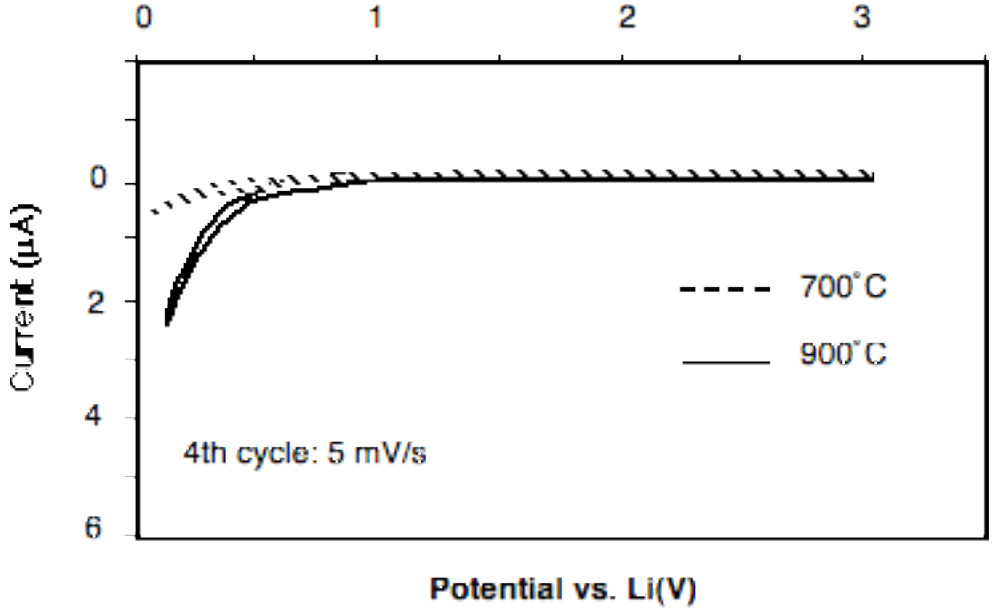

Figure 4-74: Cyclic voltammograms of carbon films pyrolyzed at 900°C (solid line) and 700°C (dashed line) acquired in 1 M $LiClO_4$ (EC:DMC) . Scan rate 5 mV/s.

Furthermore, the SEI film formed in the non-aqueous electrolyte is thicker on the carbon films obtained at 900°C, as indicated by the in situ AFM measurements (Figure 4-75).

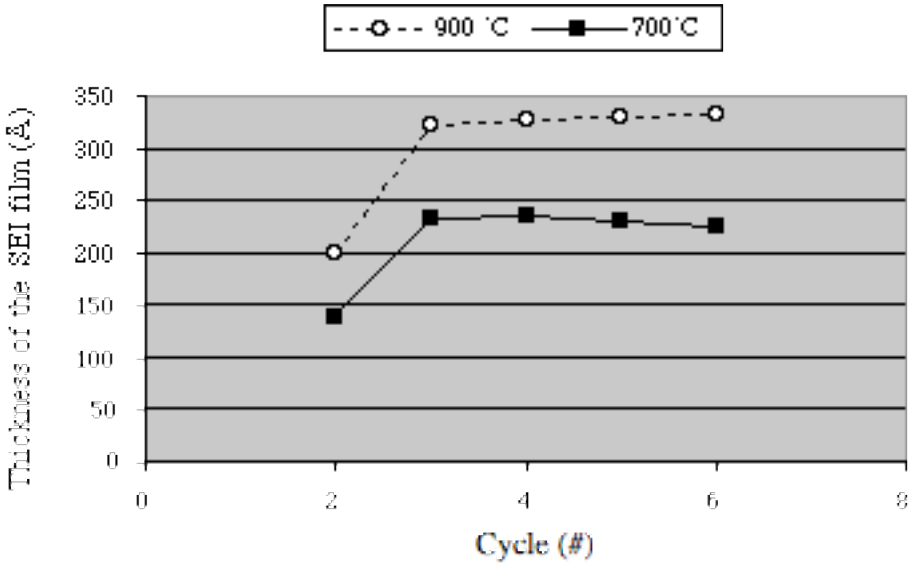

Figure 4-75: Thickness of the SEI films formed in 1 M $LiClO_4$ (EC:DMC). 900°C vs. 700°C carbon film.

As supposed before the beginning of this study, the electrochemical behavior of the carbon films is affected by the variation in resistance and film composition. Our electrochemical results confirm the recently published kinetics data [119]. In this work Ranganathan and coworkers demonstrated that the electron-transfer rate for $Fe(CN)_6^{4-}$ / $Fe(CN)_6^{3-}$ redox couple is strongly dependent on the pyrolysis temperature, but that can approach the electron-transfer rate of glassy carbon for pyrolysis temperature higher that 1000°C. The results presented here and in literature indicate that carbon film electrodes made by pyrolysis of photoresist have glassy carbon-like electrochemical behavior with good electrochemical reversibility. Therefore by selecting an appropriate pyrolysis temperature, carbon films can be produced electrochemically active or inert according to the purpose. In addition, the ability to use photolithography to make electrode patterns makes carbon films very attractive to develop micro-power supplies for MEMS applications.

4.5 Resistance behavior of the SEI film formed on HOPG and carbon electrodes

The electrical conductivity of electrode materials is one of the most significant issues for the design of high performance batteries. In addition to such practical importance, local conductivity measurements would be an effective approach to

study the influence of the SEI film formation on the electronic properties of the substrate electrode, especially at low dimensional scale.

It is well known that the SEI film formed during the first cycles in organic electrolyte is not electronically conductive [13]. To study the resistance of the electrode with and without SEI film, HOPG and OiR carbon electrodes were imaged by CSAFM before and after having been cycled in 1 M $LiClO_4$ (EC:DMC). In Figure 4-76 the topography and the conductivity of a fresh cleaved HOPG surface are shown.

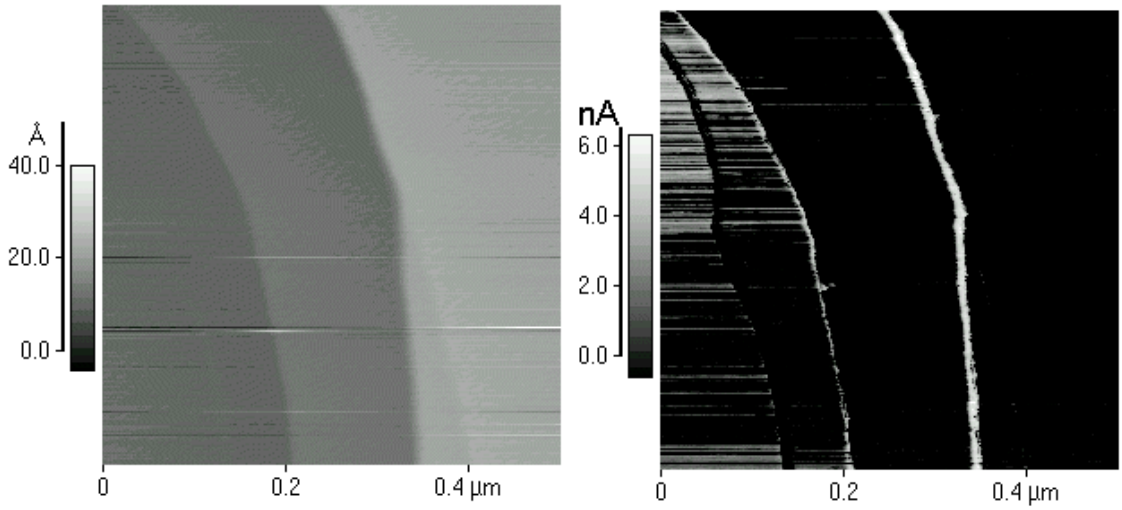

Figure 4-76: HOPG surface imaged by CSAFM: topography (left); Current (right). Bias –0.1 V. Bright and dark indicate high and low conductivity, respectively.

Because of the negative bias applied, dark indicates low conductivity while bright means high conductivity. The conductivity map of the HOPG surface shows a much higher current signal near the step locations than on the basal plane. In fact it is well known that the electronic conductivity is greater than $3 \cdot 10^4\ \Omega^{-1}\ cm^{-1}$ at room temperature in the a-axis, i.e. in the basal plane, while it is only ca. $1\ \Omega^{-1}\ cm^{-1}$ in the c-axis (perpendicular direction).

After 5 charge-discharge cycles between 3 V and 0 V at 5 mV/s, a compact SEI film was formed on the HOPG surface. Consequently, as shown in Figure 4-77, the conductivity signal was decreased consistently.

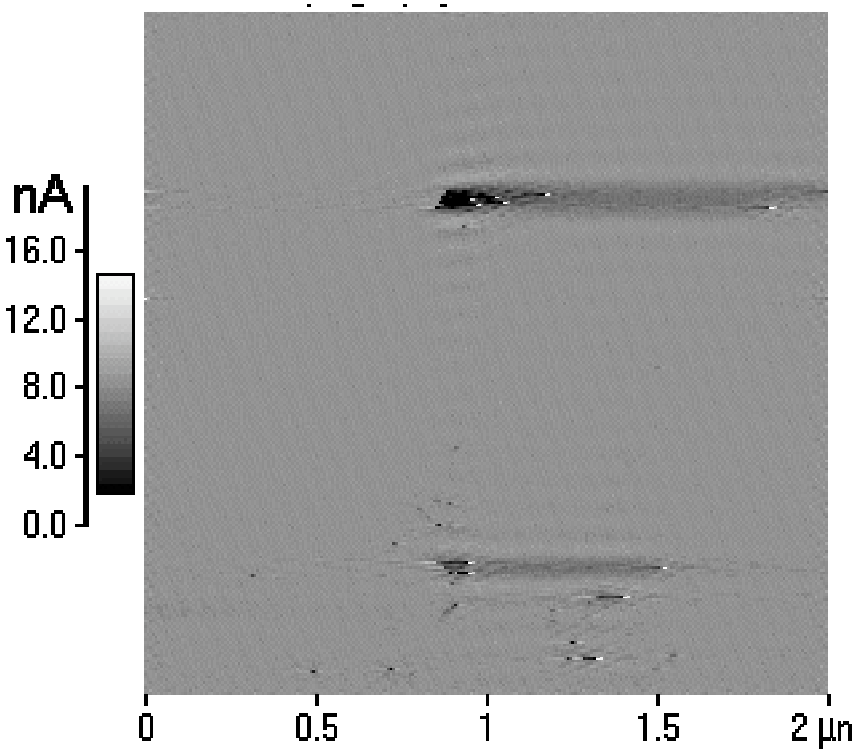

Figure 4-77: Current signal by CSAFM of the SEI film formed on HOPG in 1 M $LiClO_4$ (EC:DMC), scan rate 5 mV/s. Bias +0.1 V. Bright and dark indicate low and high conductivity, respectively.

The three dark spots which indicate a local increase in conductivity were caused by local scan in potential between +20 V and -20 V. Applying strong electric field seems to destroy the SEI film. The grow in current signal is due to the fact that now the HOPG surface is also contributing to increase the conductivity because the SEI film was destroyed.

The same technique was applied to investigate the electrical properties of the SEI film formed on a carbon film pyrolyzed at 900°C. The sample was discharge and charge ten times from 3 V to 0 V in 1 M $LiClO_4$ (EC:DMC). Therefore, it was dried overnight in He atmosphere and imaged by CSAFM in a glove box saturated with He. The SEI film formed on the carbon electrode was never exposed to the air.

The topography of the SEI film on the OiR carbon electrode is shown in Figure 4-78. The surface appears rather flat and does not show evidence of the globular structures imaged previously during in situ experiments. We suppose that the drying process affects the morphology of the SEI film. The mechanical properties also changes as it could be possible to image the SEI film also at much higher loading forces than in the electrolyte.

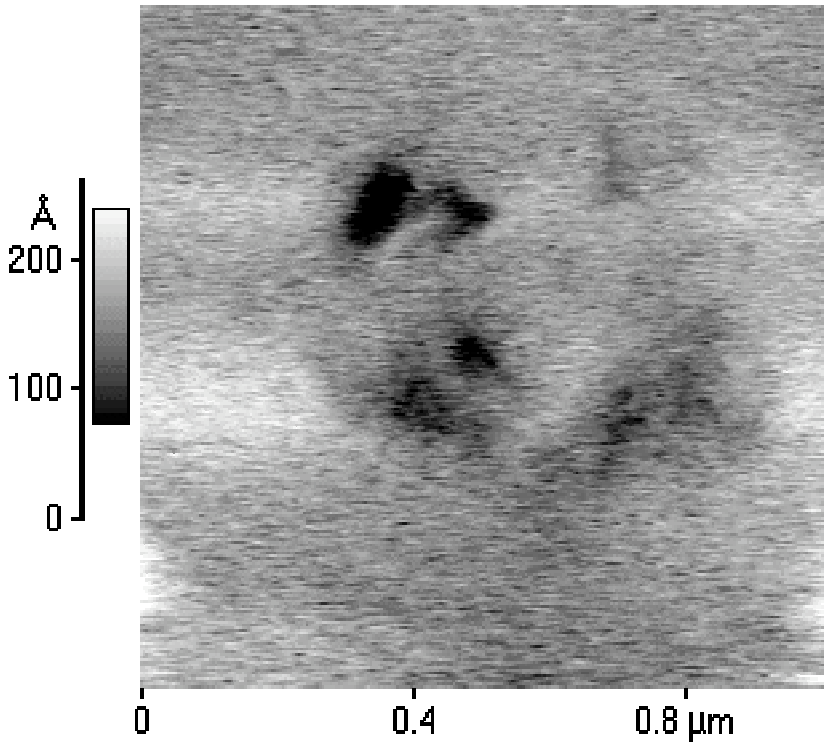

Figure 4-78: Topography image of the SEI film on 900°C Carbon electrode after local modification of the electric field.

The conductivity map corresponding to the above topography is shown in Figure 4-79. In correspondence of the holes also visible in topography, a very high current flow was observed. On the rest of the surface, the current signal was rather homogenous and presenting no discontinuity. We believe that he holes imaged in both signals were produced by high potentials, which had been applied locally to study the current-potential dependence. We think that the strong electric field locally applied could destroy the SEI film. Therefore the high current signal shown in correspondence of the holes is due to the conductive carbon substrate.

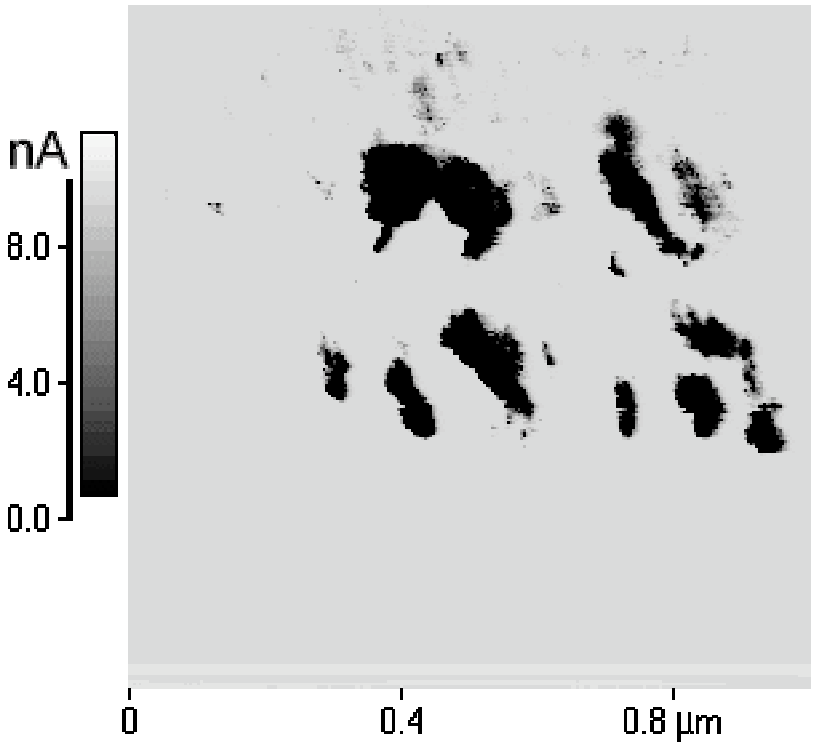

Figure 4-79: Current signal acquired simultaneously with the image shown above.

To demonstrate that the SEI film is no more present in the holes, the current-potential dependence was investigated inside and outside the holes.

In Figure 4-80 the characteristic I-V curve acquired in bright and dark regions of the previous image are shown.

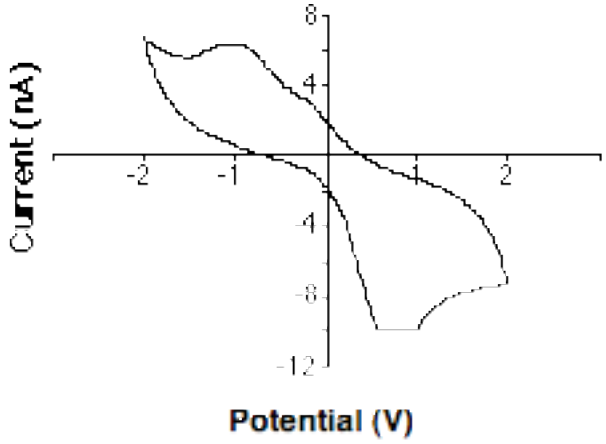

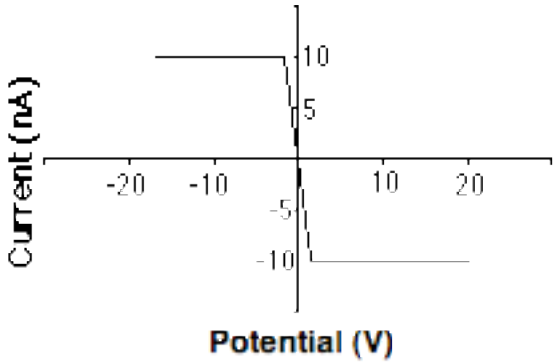

Figure 4-80: I-V curves on SEI film: bright zone (up); dark zone (down).

The upper curve was acquired in a point of the surface not damaged by the electric field. The dependence of the current from the applied bias voltage indicates an electrical behavior quite complex, which is typical of a polymer-like material. The bottom curve was acquired in a hole. The current – voltage linear behavior was attributed to the contribution of the carbon substrate, which is no more isolated by the SEI film.

Ex situ CSAFM technique is an interesting technique suitable for investigating the electric resistance behavior of electrode with and without SEI film. Our results show a very complex current-potential dependence for the SEI film that, possibly, indicates the polymer nature of the SEI material. Normally, the SEI film is fully isolating the substrate and prevents any electron conductivity. Nevertheless local electric field can destroy the SEI film and consequently the original electron conductivity of the substrate material is again predominant.

5. Conclusions and Outlook

5.1 Conclusions

This study has demonstrated that Scanning Probe Microscopy is a powerful in situ tool for investigating intercalation reactions in aqueous and non aqueous electrolytes under potential control. The main results obtained are resumed as follow.

5.1.1 HOPG in perchloric and sulfuric acids

For the first time a reproducible, quantitative estimate of the interlayer spacing of graphene layers could be obtained by in situ AFM measurements for the $HClO_4$ - GIC (stage IV, III and II) and H_2SO_4 - GIC (stage IV) formation in HOPG. In perchloric acid the experimental values are in agreement with the theoretical expectation, only for small stacks of graphene layers. For a larger number of layers the percentage of interlayer distance change decreases. The AFM results clearly demonstrate the local aspect of the intercalation process into HOPG by revealing coexisting regions with different kinetics for the intercalation and deintercalation process. The intercalation process appears to be faster than the reverse deintercalation.
Furthermore, blister formation in perchloric acid was observed as a function of the potential applied. Finally, as a consequence of the much lower charge efficiency only the stage IV formation could be evaluated in H_2SO_4. The corresponding experimental values for the change of interlayer spacing are again in agreement with the theoretical expectation. Compare to the results for the stage IV formation in perchloric acid, dramatic change of the surface morphology are observed already after 2-3 intercalation cycles in sulfuric acid. The effect of the intercalation process on the friction property of the graphite surface can be summarized as follows:

- The HOPG basal plane did not show any friction dependence upon the potential applied;
- The friction coefficient at HOPG steps was observed to reversibly change in the potential region between –0.2 V and +0.7 V vs. PtQRef electrode;

- after stage formation and dissolution, at some HOPG steps the friction properties change irreversibly, i.e. a permanent friction signal appear. Therefore we don't have anymore a change in friction while the potential is cycled between -200 mV_{Pt} and +700 mV_{Pt} after intercalation processes.

5.1.2 HOPG in Lithium perchlorate

Conditions for a direct observation of the SEI film formation process by in situ electrochemical AFM were found. The investigations revealed that the SEI film is formed at potentials more negative than 0.7 V vs. Li/Li^+.
After the first voltammetric cycle between 3 V and 0.01 V, the SEI film is about 15 nm thick and dense, but does not yet completely cover the HOPG surface. After two cycles the SEI film completely covers the surface of the HOPG electrode and has an average roughness of 4 nm and a thickness of about 25 nm.
These preliminary results suggest a more complex growth dynamics of the SEI film than hitherto expected and support a nucleation-and-growth mechanism.

5.1.3 Carbon electrodes by pyrolysis of photoresist

Both photoresists generated high conductive carbon films when they are pyrolyzed at temperatures higher than 700°C. The conductivity measured by CSAFM drops down dramatically for temperatures less than 600°C, in agreement with the sheet resistance determined by the four-point probe method.
Samples pyrolyzed at 600°C show a non-linear resistance behavior. All the other samples show an ohmic-like resistance.
Surface current mapping reveals the presence of outlet regions characterized by a semiconductor resistance behavior.
Carbon films from OiR positive photoresists are more conductive than samples from XPSU negative photoresists.
XPS and Raman results confirm the trend of the resistance measurements and are in good agreement with the general behavior of "ordinary" glassy carbon.
This variation in sheet resistance affects the thickness of the SEI film formed and more generally the electrochemical activity.
CSAFM ex situ studies revealed that, as expected, the SEI film shows a very low conductivity and a non linear resistance behavior. Furthermore, the SEI film morphology can be modified locally when strong electric fields are applied.

5.2 Outlook

The results of the thesis have shown that in situ SPM methods can be applied in a variety of electrolytic media to investigate anode materials.
However, there are several topics, especially correlated to the SEI film formation process that can furthermore be explored. The temperature of formation of the SEI film, the content of water in the electrolyte and the nature of the electrolyte are expected to affect substantially the SEI film formation process and, more generally, the electrochemical behavior of the electrode materials utilized.
Because of the "soft" nature of the SEI films, the use of non contact or semicontact AFM techniques should also improve the topographic resolution of the method and open the possibility to investigate other properties of the electrode surfaces, like visco-elasticity and adhesion. Mechanical properties could furthermore investigated by local force spectroscopy to determine, for instance, the Young modulus of the SEI film.
Similar investigation has also to be extended to Metal Oxide, the positive electrode of a Li-ion battery system.
The CSAFM method, here applied ex situ, could be upgraded for in situ experiments. To do this, unwanted electrochemical reactions as well as capacitive currents have to be minimized by coating only the foremost part of the tip and insulating the remaining part. According to Hartmannn et al. [130], the force – distance interaction can be influenced by the surface charge of the tip and the sample. Therefore, provided a bi-potentiostatic control of the tip and of the sample, the force – distance properties can be adjusted to minimize the interaction of the tip and improving the imaging quality, as suggested in a different context by Nyffenegger [131].
Finally, the production of carbon films by pyrolysis of photoresists materials can be joined with the AFM technique as nano-machining tool to challenge the development of battery systems at the nano scale level.

5.3 Publications and presentations

5.3.1 Reviewed papers

-"Electrochemical/Interfacial studies of carbon films in non-aqueous electrolytes" D. Alliata, R. Kostecki, X. Song, K. Kinoshita, R. Kötz, Proceedings of IMLB-10

Conference, May 28-Jun2 2, 2000, to be published as special issue of the J. of. Power Sources.

-"The complex electrrochemistry of graphite electrodes in Lithium-ion batteries" P. Novák, F. Joho, M. Lanz, B. Rykart, J-C. Panitz, D. Alliata, R. Kötz, Proceedings of IMLB-10 Conference, May 28-Jun2 2, 2000, to be published as special issue of the J. of. Power Sources.

-"Electrochemical SPM investigation of the solid electrolyte interphase film formed on HOPG electrodes" D. Alliata, R. Kötz, P. Novák, H. Siegenthaler, Electrochemistry Communications, submitted.

-"In situ AFM study of interlayer spacing during anion intercalation into HOPG in aqueous electrolyte" D. Alliata, R. Kötz, O. Haas, H. Siegenthaler, Langmuir 15:24 (1999) 8483.

-"Anion intercalation into highly oriented pyrolytic graphite studied by electrochemical atomic force microscopy" D. Alliata, P. Häring, O. Haas, R. Kötz, H. Siegenthaler, Electrochemistry Communications 1 (1999) 5-9.

-"In situ Atomic Force Microscopy of Electrochemical Activated Glassy Carbon" D. Alliata, P. Häring, O. Haas, R. Kötz, H. Siegenthaler, Electrochemical and Solid State Letters 2 (1999) 33-35.

5.3.2 Posters

-"Electrochemical/Interfacial Studies of Carbon Films in Non-aqueous Electrolytes" D. Alliata, R. Kostecki, X. Song, K. Kinoshita, R. Kötz, Abstract , IMLB10th Conference, Como (I), May 28 - June, 2000

-"Intercalation process of perchlorate ions in HOPG: an SPM and XPS study" B. Schnyder, D. Alliata, R. Kötz, H. Siegenthaler, Abstract # CMD-18, Montreux, CH, March 13-17, 2000.

-"Graphite electrodes in aqueous and non-aqueous media studied by electrochemical scanning probe microscopy" D. Alliata, R. Kötz, O. Haas, H. Siegenthaler, Abstract #430 Sym 4, 50th ISE Meeting, Pavia, Sept. 5-10, 1999

-"In situ electrochemical STM/AFM investigation of graphite/non aqueous electrolyte interface" D. Alliata, R. Kötz, O. Haas, H. Siegenthaler, Abstract # 2, Nanoforum CH-US, September 20-22, 1999 ETH Zurich, Switzerland

-"Electrochemical Scanning Probe Microscopy of graphite electrodes during anion intercalation processes" D. Alliata, R. Kötz, O. Haas, H. Siegenthaler, Abstract # 4, Hasliberg 3 - 3rd Hasliberg Worshop on Nanoscience, October 12-16, 1998.

-“Electrochemical Scanning Probe Microscopy of graphite electrodes during anion intercalation processes” D. Alliata, P. Häring, R. Kötz, O. Haas, H. Siegenthaler, Abstract # NS.PTu.54, 5th International Conference on Nanometer-scale Science and Technology (NANO 5), Birmingham, UK, August 31-September 4, 1998

5.3.3 Oral presentations

-Swiss Physical Society Meeting, February 26-27, 1998 Bern, Switzerland.
- “Electrochemical STM study of anion intercalation in HOPG” D. Alliata, O. Haas, P. Häring, R. Kötz, H. Siegenthaler, 5th European Users Meeting '95 - Park Scientific Instruments, September 10-14, 1997 Padova, Italy.

6. Acknowledgments

7. Index

7.1 Abbreviations

AFM, Atomic Force Microscopy
CSAFM, Current sebsitive atomic force microscopy
CDL, Double layer capacity
CV, Cyclic voltammogram
DEMS, Differential Electrolytic Mass Spectroscopy
FTIR, Fourier Transformed Infrared Spectroscopy
GC, Glassy Carbon
HOPG, Highly Oriented Pyrolytic Graphite
LFM, Lateral Force Microscopy
NHE, Normal hidrogen electrode
PAR, Princeton Applied Research
PBD, Probe Beam Deflection
PSD, position sensitive Photodetektor
Pt-QRef, Platin-quasi reference electrode
SEM, Scanning electrone microscopy
SFM, Scanning force microscopy
SME, Saturated mercury electrode
SPM, Scanning probe microscopy
STM, Scanning tunneling microscopy
UHV, Ultra high vacuum

7.2 Addresses of manufacturers

Manufacturer	**Adress**
Agar Scietific Ltd.	Stansted, Essex, U.K.
Balzers AG	9496 Balzers, FL
Buehler AG	40599 Düsseldorf, D
Carba Gas AG	4056 Basel
Cell Pack AG	5610 Wohlen

Cendres & Métaux SA	2504 Biel
Ciba-Geigy AG	4002 Basel
Debrunner AG	4402 Frenkendorf
Demetron	6450 Hanau, D
EG&G	Princeton, NJ, USA
Elga Ltd.	High Wycombe, Bucks, U.K.
Emetron	6450 Hanau, D
Fluka Chemie AG	9471 Buchs
Goodfellow Ltd.	Cambridge, U.K.
Leica Gmbh	8152 Glattbrugg
Media Cybernetics Ltd.	Silver Spring, Maryland, USA
Merz+Benteli AG	3172 Niederwangen
Metrohm AG	9100 Herisau
Newport Ltd.	8952 Schlieren
Nikon Ltd.	4054 Basel
Olin Corp.	CT06856-4500 Norwalk, USA
Panacol AG	8105 Regensdorf
Polyscience AG	6330 Cham
Sauerstoffwerk Lenzburg	5600 Lenzburg
Schait Elektronik AG	8603 Schwerzenbach
Shipley Company	MS 01752, MARLBOROUGH, USA
ThermoMicroscope SA	1227 Carouge
Topcon G.m.b.H	47877 Willich, D
Union Carbide Ltd.	1217 Meyrin

7.3 Materials

Material / Substance	**Quality**	**Manufacturer**
Argon	4.11	Carba Gas
Diamant suspension	0.25 - 9 μm	Bühler
Dimethyl carbonate	per analysis	Merck
Ethylene carbonate	per analysis	Merck
Epo-tek epoxy resin		Polyscience AG
Glassy carbon	standard	Hoch-Temperatur Werkstoffe GmbH
Gold	>99.9%	Goodfellow, Cendres & Métaux SA
HOPG	ZYH	Union Carbide

Kel-F		Cell Pack AG
KOH	per analysis	Fluka
Lithium perchlorate	per analysis	Merck
Microlever MSCT-AUMT		Thermomicroscope
NaOH	per analysis	Fluka
Nickel plates	>99.9 %	Goodfellow, Cendres & Métaux SA
Nitrogen	4.2	Carba Gas
OiR 897-101photoresist	industrial	Olin Corp.
Perchloric acid (68%)	per analysis	Fluka
Platinum wire	>99.9 %	Goodfellow, Cendres & Métaux SA
Pointprobe cantilever		Nanosensors GmbH
Polypropylene	standard	Cell Pack
Pt/Ir-wire	Alloy 80/20	Goodfellow, Cendres & Métaux SA
Silver paint	>99.9 %	Demetron GmbH
Sulfuric acid (97%)	per analysis	Fluka
Ultralever ULCT-AUMT		Thermomicroscope SA
XPSU photoresist	industrial	Shipley Co.
ZnO_2 Diaphragma		Metrohm

8. References

[1] E. Peled, in Lithium Batteries, J.P. Gabano, Editor, Academic Press,New York, 1983.

[2] C. Vincent, B. Scrosati, Modern batteries: an introduction to electrochemical power sources , 2nd Ed., Arnold, London, 1997.

[3] L. Pietronero, E. Tesatti, Physics of Intercalation Compounds, Spinger, Berlin, D, 1981.

[4] M.S. Whittingham, J. Electrochem. Soc. 124 (1977) 1387.

[5] R. Schöllhorn, Physica B, C99 (1980) 89.

[6] M.C. Miras, C. Barbero, R. Kötz, O. Haas, V.M. Schmidt, J. Electroanal. Chem., 338 (1992) 279.

[7] P. Zhou, J.E. Fischer, Phys. Rev. B53 (1996) 12643.

[8] K.E. Carr, Carbon, 8 (1970) 155.

[9] W. Biberacher, A. Lerf, J.O. Besenhard, H. Mohwald, T. Butz, Mater. Res. Bull. 17 (1982) 1385.

[10] G. Binning, F.C. Quate, C. Gerber, Phy. Rev. Lett. 56 (1986) 930.

[11] H. Siegenthaler, in Scanning Tunneling Microscopy II , R. Wiesendanger, H.J. Guentherodt, Editors, Springer Verlag, Berlin, 1993.

[12] A.A. Gewirth, H. Siegenthaler, Nanoscale probe of the Solid/Liquid Inferface Nato ASI Series E: Applied Science vol.288, Kluwer Academic Publishers, Dordrecht, 1995.

[13] M. Inaba, Y. Kawatate, A. Funabiki, S-K. Jeong, T. Abe, Z. Ogumi, Electrochim. Acta 45 (1999) 99.

[14] K.A. Kirasawa, T. Sato, H. Asahina, S. Yamaguchi, S. Mori, J. Electrochem. Soc. 144 (1997) L81.

[15] G.M. Jenkins, K. Kawamura, Polymeric Carbons, Carbon fibre, Glass and Char, Cambridge University Press, Cambrigde, UK, 1976.

[16] L.B. Ebert, Ann. Rev. Mater. Sci. 6 (1976) 181.

[17] J.O. Besenhard, H. P. Fritz, Angew. Chem. Int. Ed. Engl. 22 (1983) 950.

[18] W. Rüdorff in Advances in Inorganic Chemistry and Radiochemistry, (Ed. H.J. Emeleus and A.G. Sharpe), Academic Press, New York, 1959.

[19] W.R. McKinnon, R.R. Häring in "Modern aspects of electrochemistry" (Ed.: R.E.White, J. Bockris, A. Conway), PLENUM, London (UK) 1983, p. 248.

[20] K. Kinoshita, Carbon: electrochemical and physicochemical properties John Wiley & Sons: New York, 1988.

[21] F. Beck, H. Junge, H. Krohn, Electrochim. Acta, 26 (1981) 799.

[22] F. Kang, T-Y. Zhang, Y. Leng, J. Phys. Chem. Solids 57 (1996) 883.

[23] D.C. Alsmeyer, R.L. McCreery, Anal. Chem. 64 (1992) 1528.

[24] C.A. Goss, J.C. Brumfield, E.A. Irene, R.W. Murray, Anal. Chem. 65 (1993) 1378.

[25] B.L. Zhang, Q. Chi, S. Dong, E. Wang, Electrochim. Acta 40 (1995) 733.

[26] J. Zhang, E. Wang, J. Electroanal. Chem. 399 (1995) 83.

[27] D. Aurbach, B. Markovsky, A. Shechter, Y. Ein-Eli, H. Cohen, J. Electrochem. Soc., 143 (1996) 3809.

[28] O. Haas, E.J. Cairns, Annu. Rep. Prog. Chem., Sect. C, 95 (1999) 163.

[29] R. Fong, U. von Sacken, J. R. Dahn, J. Electrochem. Soc., 137 (1990) 2009.

[30] M.Winter, J.O.Besenhard, M.E.Spahr, P.Novak, Adv. Mater., 10 (1998) 725.

[31] M. Winter, P. Novak, A. Monnier, J. Electrochem. Soc., 145 (1998) 428.

[32] G.H. Wrodnigg, J.O. Besenhard, M. Winter, J. Electrochem. Soc., 146 (1999) 470.

[33] Z. Ogumi, M. Inaba, Bull. Chem. Soc. Jpn., 71 (1998) 521.

[34] D. Aurbach, Y. Ein-Eli, J. Electrochem. Soc. 142 (1995) 1746.

[35] W. Huang, R. Frech, J. Electrochem. Soc., 145 (1998) 765.

[36] E. Endo, M. Ata, K. Tanaka, K. Sekai, J. Electrochem. Soc., 145 (1998) 3757.

[37] M. Winter, P. Novak, J. Electrochem. Soc., 145 (1998) L27.

[38] R. Imhof, P. Novak, J. Electrochem. Soc., 145 (1998) 1081.

[39] F. Kong, J. Kim, X. Song, M. Inaba, K. Kinoshita, F. McLarnon, Electrochem. Sol. State Lett., 1 (1998) 39.

[40] J.O. Besenhard, M. Winter, J. Yang, Proceeding of the Int. workshop on Advanced Batteries, Osaka, (1995) 129.

[41] G. Binnig, H. Rohrer, Angew. Cgem. Int. Ed. Engl. 26 (1987) 606.

[42] G. Binnig, H. Rohrer, Surf. Sci. 126 (1983) 236.

[43] G. Binnig, C. Quate, C. Gerber, Phys. Rev. Lett., 56 (1986) 930.

[44] U.D. Schwarz in “Handbook of Microscopy: methods II” (Ed.: S. Amelinckx, D. van Dyck, J. van Landuyt, G. van Tendenloo), VCH, Weinheim (D) 1997, p. 839.

[45] D. Anselmetti, R. Lüthi, E. Meyer, T. Richmond, M. Dreier, J.E. Frommer, H-J. Güntherodt, Nanotechnology 5 (1994) 87.

[46] Y. Martin, C. Williams, H. Wickramasinghe, J. Appl. Phys. 61 (1987) 4729.

[47] R. Christoph, H. Siegenthaler, H. Rohrer, H. Wiese, Electrochim. Acta 34 (1989) 1011.

[48] L.A. Bottomley, J.E. Coury, P.N. First, Anal. Chem. 68 (1996) 185R.

[49] J. Frommer, Angew. Chem. Int. Ed. Engl. 31 (1992) 1298.

[50] R. Sonnenfeld, P.K. Hansma, Science 232 (1986) 211.

[51] O. Lev, Fu-Ren Fan, A.J. Bard, J. Electrochem. Soc. 135 (1988) 783.

[52] P. Lustenberger, H. Rohrer, R. Christoph, H. Siegenthaler, J. Electroanal. Chem. 243 (1988) 225.

[53] P. Drake, C.B. Prater, A.L. Weisenhorn, S.A.C. Gould, T.R. Albrecht, C.F. Quate, D.S. Cannell, H.G. Hansma, P.K. Hansma, Science 243 (1989) 1586.

[54] P. Novák, Personal communication, 1998.

[55] K. Itaya, E. Tomita, Surf. Sci. 201 (1988) L507.

[56] C. M. Brett, A. M. O. Brett, Electrochemistry Principles, methods and applications, Oxford University Press, Oxford, 1993, p. 138.

[57] M. Sullivan, R. Kötz, O. Haas, J. Electrochem. Soc. (2000) 308.

[58] M. Pourbaix (ed.), Atlas d'équilibres electrochemiques á 25ºC, Gauthier-Villars, Paris (1963)359.

[59] R. C. Weast (ed.), CRC Handbook of Chemistry and Physics, 69th Edition (1989) D-151.

[60] E. Gileadi, E. Kirowa-Eisner, J. Penciner, Interfacial Electrochemistry: an experimental approach, p. 222, Addison-Wesley, London, UK, 1975

[61] R. Nyffenegger, E. Amman, H. Siegenthaler, R. Kötz, O. Haas, Electrochim. Acta 40 (1995) 1411.

[62] P. Häring, R. Kötz, J. Electroanal. Chem. 385 (1995) 273.

[63] P. Häring, PhD Thesis, University of Bern, Bern, 1998.

[64] L.E.C. van de Leemput, P.H.H. Rongen, B.H. Timmerman, H. Kempen, Rev. Sci. Instrum. 62 (1991) 986.

[65] M.Locatelli, G.Lamboley, J.P. Michenaud, V. Bayot, Rev. Sci. Instrum. 59 (1991) 661.

[66] C.Z. Cai, X.Y. Chen, Q.Q. Shu, X.L. Zhen, Rev. Sci. Instrum. 63 (1992) 5649.

[67] R. Staub, D. Alliata, C. Nicolini, Rev. Sci. Intrum. 66 (1995) 2513.

[68] User's guide to Autoprobe CP, May 22, 1998 (Thermomicroscope)

[69] N. M. Forsyth, P. Coxon, Surf. Interface Anal. 21 (1994) 430.

[70] J. H. Scofield, J. Electron Spectrosc. Relat. Phenom. 8 (1976) 129.

[71] Th. Kunz, Thesis, ETH Zürich, 1997.

[72] M. Madou, A. Lal, G. Schmidt, X. Song, K. Kinoshita, M. Fendorf, A. Zettl, R. White, in Chemical and biological sensors and analytical electrochemical

methods, A. Ricco, M. Butler, P. Vanysek, G. Horvai, A. Silva, Editors, PV 97-19, The Electrochemical Society Proceedings Series, Pennington New Jersey (1997).

[73] P.W. Atkins, Physical Chemistry 4th edition, Oxford University Press, Oxford, United Kingdom, 1992, p. 621.

[74] R. M. Penner, Scanning Microscopy, 7 (1993) 805.

[75] R. M. Penner, M. J. Heben, N. S. Lewis, C. F. Quate, Appl. Phys. Lett., 58 (1991) 1389.

[76] R. E. Russo, Appl. Spectroscopy, 49 (1995) 14.

[77] Z. Klusek, Appl. Surf. Sci., 125 (1998) 339.

[78] Z. Klosek, P. Kobierski, W. Olejniczak, Appl. Phys. A 66 (1998) S129.

[79] S.M. Lee, Y.H. Lee, Y.G. Hwang, J.R. Hahn, H. Kang, Phy. Rev. Lett., 82 (19990 217.

[80] Y. Maeda, Y. Okemoto, M. Inagaki, J. Electrochem. Soc. 132 (1985) 2369.

[81] S. Aronson, S. Lemont, J. Weiner, Inorg. Chem. 10 (1971) 1296.

[82] V.Z. Mordkovich, Synthetic Metals 63 (1994) 1.

[83] F. Beck, H. Junge, H. Krohn, in Power Sources 8, J. Thompson Editor, Academic Press, London, United Kingdom, 1989.

[84] F. Beck, H. Krohn, Synthetic Metals, 7 (1983) 193.

[85] M. Winter, P. Novak, A. Monnier, J. Electrochem. Soc. 145 (1998) 428.

[86] J.G. Hooley, Mater. Sci. Eng. 31 (1977) 17.

[87] H. Shi, J. Barker, M.Y. Saïdi, R. Koksbang, J. Electrochem. Soc. 143 (1996) 3466.

[88] R. Moret, Intercalation of Layered Materials, NATO ASI Series (Ed.: M.S. Dresselhaus), Plenum Press, New York 1986, B148, p. 185.

[89] J.O. Besenhard, E. Wudy, H. Mohwald, J.J. Nickl, W. Biberacher, W. Foag, Synthetic Metals 7 (1983) 185.

[90] R. Rhodes, Proceeding of Fifth International Power Symposium, Brighton, 1966, in Power Sources 1966 , D.A. Collins, editor, Pergamon Press: London, 1966.

[91] K.W. Hathcock, J.C. Brumfield, C.A. Goss, E.A. Irene, R.W. Murray, Anal. Chem. 67 (1995) 2201.

[92] K. Johnson, Contact Mechanics, Cambridge University Press, Cambridge, 1985.

[93] M. Binggeli, R. Christoph, H.E. Hintermann, O. Marti, Surf. Coat. Technol. 62 (1993) 523.

[94] M. Binggeli, R. Christoph, H-E Hintermann, J. Colchero, O. Marti Nanotechnology 4 (1993) 59.

[95] E. Weilandt, A. Menck, O. Marti Surface and Interface Analysis 23 (1995) 428.[

[96] D. M. Kolb, D.L. Rath, R. Wille, W.N. Hansen, Ber. Bunsenges. Phys. Chem. 87 (1983) 1108.

[97] R. Kötz in Advances in Electrochemical Science and Engineering Voi. 1, H. Gerischer and C.W. Tobias, Editors, VCH, Berlin (1990).

[98] G.K. Wertheim, P.M.Th.M. Van Attekum, S. Basu, Solid State Commun. 33 (1980) 1127.

[99] M. Inagaki, O. Tanaike, N. Iwashita, Synthetic Metals 73 (1995) 83.

[100] E. Peled, J. Electrochem. Soc. 126 (1979) 2047.

[101] E. Peled, in Lithium Batteries, J.P. Gabano, Editor, Academic Press, New York (1983).

[102] J.R. Dahn, A.K. Sleigh, H. Shi, J.N. Reimers, Q. Zhong, B.M. Way, Electrochim. Acta 38 (1993) 1179.

[103] T.D. Tran, J.H. Feikert, X. Song, K. Kinoshita, J. Electrochem. Soc. 142 (1995) 3297.

[104] M. Inaba, Z. Siroma, Y. Kawatate, A. Funabiki, Z. Ogumi, J. Power Sources, 68 (1997) 221.

[105] Z.X. Shu, R.S. McMillan, J.J. Murray, J. Electrochem. Soc., 140 (1993) 922.

[106] P. Novak, F. Joho, R. Imhof, J-C. Panitz, O. Haas, J. Power Sources, 81 (1999) 212.

[107] A.C. Chu, J.Y. Josefowicz, G.C. Farrington, J. Electrochem. Soc., 144 (1997) 4161.

[108] M. Inaba, Z. Siroma, A. Funabiki, Z. Ogumi, Langmuir, 12 (1996) 1535.

[109] J.O. Besenhard, M. Winter, J. Yang, W. Biberacher, J. Power Sources, 54 (1995) 228.

[110] F. Joho, B. Rykart, P. Novák, M.E. Spahr, A. Monnier, PSI Scientific Report 1998, V (1998) 40.

[111] F. Joho, B. Rykart, R. Imhof, P. Novák, M.E. Spahr, Chimia 52 (1998) 193.

[112] M. Winter, R. Imhof, F. Joho, P. Novák, J. Power Sources 81 (1999) 818.

[113] Y. Aihara, M. Kodama, K. Nakahara, H. Okise, K. Murata, J. Power Sources 65 (1997) 143.

[114] D. Ingersoll, S. H. Kravitz, R.J. Shul, E.J. Heller, 196th Meeting of the Electrochem. Soc., Honolulu, Hawaii, Oct. 17-22, 1999, abstract # 323.

[115] K. Kinoshita, X. Song, J. Kim, M. Inaba, J. Power Sources 81 (1999) 170.

[116] J. Kim, X. Song, K. Kinoshita, M. Madou, R. White, J. Electrochem. Soc. 145:7 (1998) 2314.

[117] S.M. Sze, Semiconductor devices: physics and technology, John Wiley & Sons, 1985.

[118] R. Kostecki, X. Song, K. Kinoshita, Electrochem. Solid State Lett. 2 (1999) 465.

[119] S. Ranganathan, R. McCreery, S.Mouli Majji, M. Madou, J. Electrochem. Soc. 147 (2000) 277.

[120] M. Nakamizo, K. Tamai, Carbon 22 (1984) 197.

[121] F. Tuinstra, J. Koenig, J. Chem. Phys. 53 (1970) 1126.

[122] R. Nemanich, S. Solin, Phys. Rev. B 20 (1979) 392.

[123] T. Mernagh, R. Cooney, R. Johnson, Carbon 22 (1984) 39.

[124] Y. Wang, D. Alsmeyer, R.L. McCreery, Chem. Mater. 2 (1990) 557.

[125] M.S. Dresselhaus, G. Dresselhaus, K. Sugihara, I.L. Spain, M.A. Goldberg, Graphite Fibers and Filaments, 98, Springer-Verlag, New York, 1988.

[126] R. Kostecki, T. Tran, X. Song, K. Kinoshita, F. McLarnon, J. Electrochem. Soc. 144 (1997) 3111.

[127] O.J.A. Schuller, S.T. Brittain, G.M. Whitesides, Adv. Mater. 9 (1997) 477.

[128] H. Q. Xiang, S. B. Fang, Y.Y. Jiang, J. Electrochem. Soc. 144 (1997) L187.

[129] T. Zheng, Q. Zhong, J. Dahn, J. Electrochem. Soc. 142 (1995) L211.

[130] U. Hartmann, Advances in electronics and electron physics 87 (1994) 49.

[131] R. Nyffenegger, Thesis, University of Bern, 1994.